POLITECNICO DI TORINO

Corso di Laurea Magistrale in Ingegneria chimica e dei processi sostenibili

Tesi di Laurea Magistrale

Digital simulation of diffusion in a $\gamma-Al_2O_3$ porous network and characterization by PFG-NMR

Relatori
Prof. Stefania Specchia
PhD Gabriel A. Ledezma Lopez
PhD Carmen W. Moncada Quintero

Candidato
Francesco Milazzo

Sessione Marzo 2022

For my family who has
wondered what I was
doing in the last year
at home

Abstract

γ-Alumina is the most important phase of alumina. It presents the higher surface area, porosity and it has been studied and exploited for the acidity of its surface that promotes catalytic performances. The industrial significance of this phase is evident as it is used as a catalyst support in numerous fields where heterogenous catalysis is involved: from automotive to petroleum refining or fuel cells applications.Because of its role, since 1935 alumina has been deeply studied in order to better understand its properties.

γ-Alumina is a disordered solid. The pore network topology and architecture of this material is not fully characterized. These often not considered textural properties are relevant to better understand the transport phenomena and the selectivity in complex chemical reactions. With this in mind, a digital twin was developed. This model can statistically reproduce the topology of the real solid (Ledezma, 2021).

PFG-NMR is a non destructive technique that allows to study diffusion phenomena in porous media. To digitally characterize the tortuosity of the digital twin a Pulsed Field Gradient-Nuclear Magnetic Resonance (PFG-NMR) simulation was developed. The simulation of a real characterization techniques allows to directly validate the calculated tortuosity.

The novel methodology developed in this thesis is based on Fickian diffusion simulations in order to save time and resources. The simulation was validated by comparison with the results obtained for a real γ-Alumina sample. The predicted value differs by less than 25% from the tortuosity factor measured by PFG-NMR.

Indice

Capitolo 1

Riassunto

1.1 Scopo

La modellazione e la previsione della cinetica delle reazioni all'interno di solidi porosi sono settori di crescente rilevanza nella progettazione di apparati ingegneristici. Una corretta caratterizzazione dei fenomeni coinvolti consente di migliorare la modellizzazione e perfezionare i processi.

L'ottimizzazione di materiali catalitici coadiuvata da calcolatori è stata studiata a fondo negli ultimi anni ma non ha raggiunto una maturità. Sebbene siano stati segnalati nuovi progressi in molti campi, la previsione necessita ancora di essere perfezionata.

Una adeguata descrizione della topologia della rete porosa è fondamentale per capire come progettare accuratamente il catalizzatore, prevedendo anche l'andamento delle reazioni e migliorando le prestazioni.

Questo lavoro si pone come obiettivo la previsione del coefficiente di tortuosità di un campione di γ-Allumina attraverso la caratterizzazione numerica di un gemello digitale (digital twin). La caratterizzazione numerica è stata sviluppata tramite una simulazione di Pulsed Field Gradient-Nuclear Magnetic Resonance, PFG-NMR. Il gemello digitale è stato costruito attraverso una ricostruzione stocastica e la topologia della struttura è stata ottenuta e validata mediante simulazioni digitali di porosimetria ad azoto.

I risultati delle simulazioni digitali sono stati successivamente correlati agli esiti di esperienze empiriche presenti sia in letteratura che nei risultati di dottorati svolti presso l'istituto di ricerca IFPEN, con sede a Lione, che ha anche supervisionato questo progetto.

La metodologia sviluppata permette un'innovativa tecnica di analisi dei materiali porosi ed è supportata da dati sperimentali. Per comprendere i risultati ottenuti è necessario prima affrontare molti ambiti:

- Materiali porosi, in particolare allumina
- PFG-NMR, spiegazione teorica
- Creazione del modello fisico dell'allumina
- Modellizzazione dell'analisi PFG-NMR

Solo allora sarà possibile analizzare i risultati e confrontarli con valori simili presenti in letteratura.
Questo lavoro contribuisce alla caratterizzazione dell'effetto della topologia di un catalizzatore poroso sulla diffusione in condizioni non reattive.

1.2 Allumina

I materiali porosi sono stati ampiamente studiati per via del loro ruolo di primo piano nel mondo dell'ingegneria e delle applicazioni scientifiche (O'Sullivan, 2001). Uno dei materiali porosi più importanti è l'allumina. Allumina è il nome comune dell'ossido di alluminio, Al_2O_3, è un materiale ceramico, conosciuto e utilizzato, da almeno sette millenni. Tuttavia, solo negli ultimi due secoli e soprattutto dopo l'invenzione dei processi Bayer e Hall-Heroult(Wefers et al., 1987), l'allumina è stata comunemente usata in applicazioni commerciali (Brindenbaugh et al., 2018). L'allumina si trova in natura in forma minerale con il nome di corindone. Gli ossidi di alluminio, esistono come materiale polimorfo. Ciò significa che presentano varie fasi termodinamicamente stabili (o metastabili) e ciascuna di esse è caratterizzata da differenti proprietà fisiche e chimiche. Al_2O_3 sfruttabile nelle industrie, è comunemente ottenuto mediante un trattamento termico da un minerale precursore chiamato gibbsite.
Tra tutte le possibili configurazioni, la γ-Al_2O_3 è considerata la fase di transizione più importante dell'allumina. Essa presenta infatti la maggiore area superficiale, porosità e viene studiata e sfruttata per l'acidità della sua superficie che favorisce le prestazioni catalitiche.
L'interesse industriale di questa fase aumenta costantemente, infatti viene utilizzata come supporto catalizzatore in numerosi campi in cui è coinvolta la catalisi eterogenea come l'automotive (dove copre circa il 70% delle 850000 tonnellate di materiali ceramici coinvolti nella mercato, Rosenberger), cracking e raffinazione del petrolio (Tung et al.,1964), applicazioni di celle a combustibile come supporto sol-gel per il reforming catalitico del vapore del metanolo o l'ossidazione della benzina con water gas shift (Manasilp et al., 2002).
Per comprendere appieno come sfruttare la γ-Al_2O_3 e come riprodurlo con una simulazione numerica, è fondamentale definirne la struttura e la topologia. La

prima descrizione atomica è datata 1935 e ritrae l'allumina come uno spinello cubico $MgAl_2O_4$ (Verwey, 1935), questa struttura è stata poi confermata nel tempo. A livello mesoscopico, la struttura dell'allumina presenta un'organizzazione gerarchica ed è una potenziale spiegazione dell'elevata porosità della γ-Al_2O_3 che è in conflitto con l'elevata tortuosità del solido. Ciò implica che è presente una forte influenza dell'organizzazione della rete porosa sulla tortuosità (Kolitcheff, 2017).

1.3 Introduzione al NMR

La risonanza magnetica nucleare è un fenomeno scoperto dai gruppi di ricerca di Felix Bloch ed Edward Purcell alla fine della seconda guerra mondiale ed è valso loro il premio Nobel. La risonanza magnetica dal secolo scorso ha avuto un ruolo di primaria importanza nei campi della medicina e dell'ingegneria.
Uno dei campi di studio più rilevanti è l'argomento di questa tesi: il trasporto di massa all'interno di una rete porosa.

La risonanza magnetica dà la possibilità di ottenere informazioni sull'organizzazione della rete porosa e del coefficiente di diffussione effettivo all'interno del solido. Dal 1950 la NMR è stata adottata per studiare la diffusione molecolare all'interno di sistemi liquidi. Successivamente, attraverso l'applicazione di gradienti di maggiore intensità, l'uso della risonanza magnetica nucleare ha permesso anche l'analisi della diffusione all'interno di materiali porosi.

1.4 Teoria del NMR

I nuclei atomici, posti in un campo magnetico costante e perturbati da un campo oscillante, reagiscono producendo un segnale elettromagnetico con una frequenza caratteristica dipendente dalle caratteristiche del nucleo. Quando la frequenza di oscillazione della radiazione è uguale alla frequenza dei nuclei, si verifica il processo di risonanza magnetica nucleare.
Per capire come avviene il fenomeno è necessario esplorare cosa sia lo spin dei nuclei atomici. Lo spin nucleare è una proprietà intrinseca del nucleo e seguendo la statistica di Fermi-Durac possiede un valore semi-intero (Pauli, 1940). Lo spin può avere un valore positivo o negativo ($+\frac{1}{2}$, -$\frac{1}{2}$). Tuttavia, non è possibile identificare con certezza lo spin di una singola particella, quindi è necessario sfruttare un'analisi d'insieme seguendo la distribuzione di Boltzmann e cercando la probabilità di un certo stato, modificando l'orientamento dell'insieme applicando un campo magnetico esterno e unificando così l'orientamento totale. Questa proprietà si può

sfruttare per ottenere uno stato iniziale comune in una direzione. Lo spin, tuttavia, è ancora presente e produce una precessione (ovvero il cambiamento dell'asse di rotazione nel corpo rotante) con una frequenza ben definita chiamata frequenza di Larmor.

Una caratteristica del nucleo è la costante giromagnetica γ che rappresenta il rapporto tra momento magnetico e angolare della particella. Il vettore del momento angolare precede sull'asse del campo magnetico esterno B_0 con la frequenza di Larmor.

$$\omega = -\gamma B_0 \tag{1.1}$$

Il campo magnetico B_0 allinea gli spin e crea immediatamente uno stato comune. Per ottenere gli spostamenti è necessario utilizzare un campo magnetico alternato B_1 con la stessa frequenza di Larmor degli spin e pulsato con una sequenza scelta. Nel caso in cui l'energia dell'impulso è uguale al livello energetico dell'insieme di nuclei, la componente verticale del momento magnetico viene neutralizzata e rimane solo la direzione orizzontale con una componente che viene misurata. Il momento magnetico netto ottenuto è chiamato magnetizzazione trasversale e induce un segnale che viene poi amplificato. Il ritorno della componente longitudinale del vettore di magnetizzazione allo stato originale è chiamato rilassamento spin-lattice e la perdita di coerenza (caratteristica degli spin ad avere vettori di polarizzazione trasversali, Levitt, 2008) è chiamato rilassamento spin-spin (Rinck, 2016).

Il segnale NMR osservabile è generato dalla magnetizzazione dello spin nucleare che precede in direzione del campo magnetico ed è chiamato decadimento a induzione libera, free induction decay (FID).

Per ottenere un segnale scevro da errori nella misurazione, vengono solitamente sfruttate diverse sequenze di impulsi denominate Inversion-Recovery e Spin-Echo. Inversion-Recovery consiste in un impulso di 180°, il momento di magnetizzazione viene invertito rispetto a B_0 e diventa antiparallelo rispetto al campo magnetico. Quindi, viene inviato un successivo impulso di 90° in modo che il vettore di magnetizzazione effettivo sia rilevabile nel piano trasversale.

La sequenza Spin-Echo inizia eccitando il sistema con un impulso di 90°, gli spin sfasano sul piano trasversale, quindi un impulso di 180° permette una rifocalizzazione. Gli spin più veloci, sfruttando l'impulso a 180° recuperano lo spazio che si era creato dopo il primo impulso creando un'eco nel segnale. Dall'inviluppo di picchi di più echi si ricava il tempo di rilassamento.

1.5 PFG-NMR

Il metodo PFG-NMR, consente di misurare gli spostamenti delle molecole mediante l'attenuazione di un segnale spin-echo. Al fine di ottenere la misura è tuttavia necessario valutare i confini strutturali che influenzano la diffusione naturale

(Price,1997).
L'intensità del segnale di NMR è associata agli spin in risonanza che hanno la stessa frequenza di precessione e alla polarizzazione di fase del momento magnetico. Le rotazioni, infatti, possono perdere coerenza ma conservare la risonanza.
Il campo magnetico statico B_0 è omogeneo, tuttavia, associando un impulso, un gradiente di campo magnetico $\mathbf{g}$ (T/m) dipendente da B_0 viene aggiunto.
L'impulso di radiofrequenza viene inviato a 90° $(\pi_x/2)$ per alcuni millisecondi per segnare la posizione iniziale, quindi un impulso a 180° fa ruotare il vettore magnetizzazione attorno all'asse y, invertendo l'effetto del primo gradiente. Quindi, le molecole si diffondono e la posizione finale è identificata mandando lo stesso gradiente del primo impulso. Tuttavia, la frequenza di Larmor non può essere completamente recuperata e il segnale sarà inferiore al primo.

Pertanto, quantificando la differenza di fase tra le frequenze, è possibile identificare la variazione di posizione dell'insieme di particelle.
Modificando il tempo di diffusione è possibile ottenere vari risultati, creando una curva che mette in relazione i segnali ottenuti ed i tempi di diffusione.
Il defasamento è calcolabile tramite (Price, 1997):

$$\phi(t) = \underbrace{\gamma B_0 t}_{\text{static field}} + \underbrace{\gamma \int_0^t g(t')z(t')dt'}_{\text{pulse gradient}} \tag{1.2}$$

L'equazione 1.2 è composta da due termini: il primo riguarda lo sfasamento dovuto al campo statico, il secondo dipende dal gradiente dell'impulso inviato, dalla durata del gradiente (t) e dallo spostamento. Inoltre, nella metodologia utilizzata, g non è una funzione del tempo poiché i gradienti sono impulsi rettangolari.

$$\phi(2\tau) = \gamma g \left\{ \int_{t_1}^{t_1+\delta} z_i(t)dt - \int_{t_1+\Delta}^{t_1+\delta+\Delta} z_i(t')dt' \right\} \tag{1.3}$$

Il segnale ottenuto alla fine della sequenza si può esprimere:

$$S(2\tau)_{g=0} = S(0)exp\left(-\frac{2\tau}{T_2}\right) \tag{1.4}$$

1.6 Diffusione ristretta

Il segnale non fornisce una misura diretta dello spostamento delle particelle, ma deve essere interpretato da una funzione di autocorrelazione. Le funzioni di autocorrelazione forniscono informazioni sulla probabilità di trovare una particella in una determinata posizione dopo un certo tempo. Questa funzione P($\mathbf{r}_0$,$\mathbf{r}_1$,t) è ottenuta da un'analisi della diffusione, attraverso la prima e la seconda legge di Fick, e le annesse restrizioni dovute alla topologia del mezzo in cui avviene la diffusione.

Il segnale finale è calcolabile tramite:

$$ln\left[\frac{S(2\tau)}{S(0)}\right] = ln(E(2\tau)) \tag{1.5}$$

E l'attenuazione del segnale (da Price, 1997):

$$ln(\frac{E}{E_0}) = -\gamma^2 g^2 D\delta^2(\Delta - \delta/3) \tag{1.6}$$

Il termine $\frac{\delta}{3}$ dipende dall'ampiezza finita dell'impulso del gradiente e dal termine tra parentesi composto da Δ e δ. Un'approssimazione è possibile sapendo che $\delta \ll \Delta$, in tal caso ripetendo la misura con diverse intensità del gradiente, la curva dei segnali ottenuta ha questa forma:

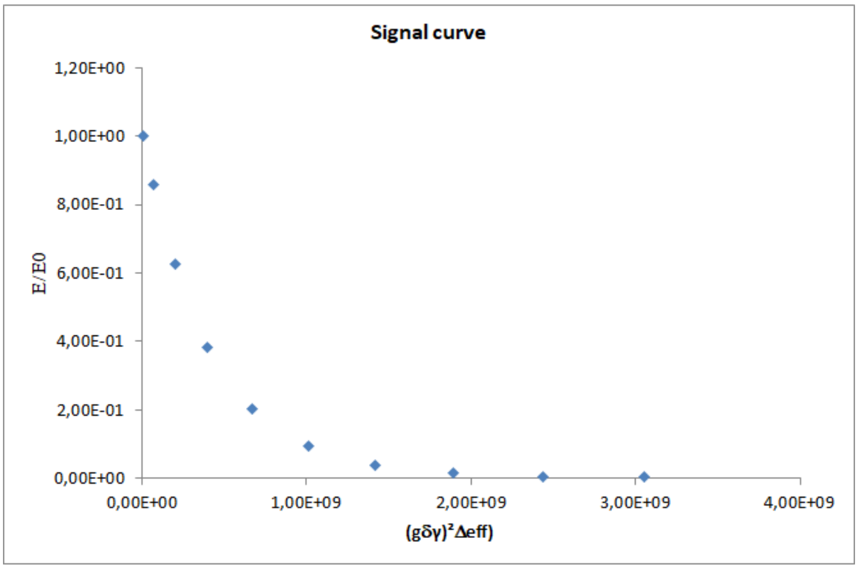

Figura 1.1: Signal attenuation curve of a PFG-NMR experiment of Acetonitrile in a porous network. Modified from Glowska, 2021

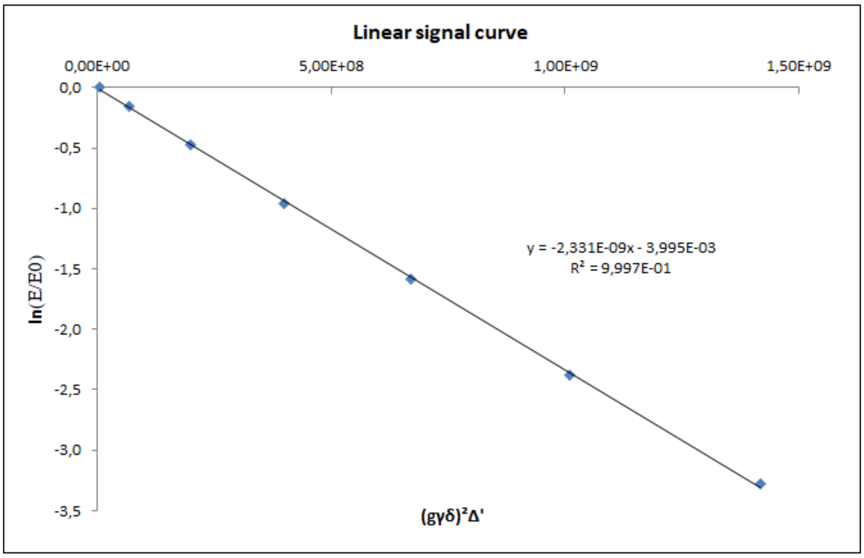

Figura 1.2: Linear signal attenuation curve of a PFG-NMR experiment of Acetonitrile in a porous network. Modified from Glowska.

Se l'attenuazione è nota, è possibile ottenere un coefficiente di diffusione apparente chiamato D_{eff}. La tortuosità della rete in cui è presente la diffusione ristretta può essere calcolata dal rapporto tra il coefficiente di diffusione reale D e il coefficiente di diffusione apparente (effettivo) D_{eff}.

$$\tau = \frac{D}{nD_{eff}} \tag{1.7}$$

n è un fattore che tiene conto della tipologia della rete. In una rete 2D n è uguale a 2, mentre in una 3D è 3.

1.7 Simulazione rete

Il progetto sviluppato è una simulazione numerica e una validazione dinamica della teoria della diffusione all'interno di una rete γ-allumina e la successiva caratterizzazione mediante PFG-NMR. La rete porosa simulata è equiparabile all'originale γ-allumina, utilizzando una simulazione ricostruita sviluppata dall'IFP-EN, istituto di Lione.

Nelle simulazioni di questa tesi, questo modello sarà semplificato perché la diffusione è un processo che richiede tempo e CPU. Utilizzando questa metodologia può essere possibile imitare e persino prevedere le prestazioni di pellets composti da γ-Al_2O_3.

L'idea principale è che considerare ogni molecola come un sistema separato in questa simulazione non è possibile ma va studiato il comportamento medio. Anche il solido reale e il gemello digitale non coincidono esattamente ma, per via della ricostruzione, le caratteristiche texturali come diametro e lunghezza dei pori sono statisticamente comparabili così da permettere una buona approssimazione.

La rete porosa è composta da due elementi che rappresentano i pori come cilindri:

La sezione trasversale dei pori influenza fortemente le proprietà macroscopiche come il trasferimento di massa all'interno dei pori (Blunt, 2001). Le forme del reticolo, d'altra parte, sono molto più variegate e cercano di adattarsi ai dati sperimentali. Quando si sceglie il modello di rete bidimensionale, si sceglie anche la topologia, che può essere regolare o casuale.

I pori hanno geometria cilindrica e i nodi sono sfere approssimabili a punti senza volume.

Il reticolo viene creato stabilendo a priori la distanza tra nodi adiacenti, misura che dà anche la lunghezza dei pori. Inoltre, viene scelto anche il numero di nodi desiderati in ciascuna dimensione così come la PEP, probabilità di esistenza dei pori, che dà la probabilità che ciascun nodo sia legato al massimo numero di pori possibili.

In una rete 1-D la connettività massima (ovvero il numero massimo di pori collegati a un nodo) è 2, in un 2-D è 4 e in un 3-D sono collegati 6 pori.

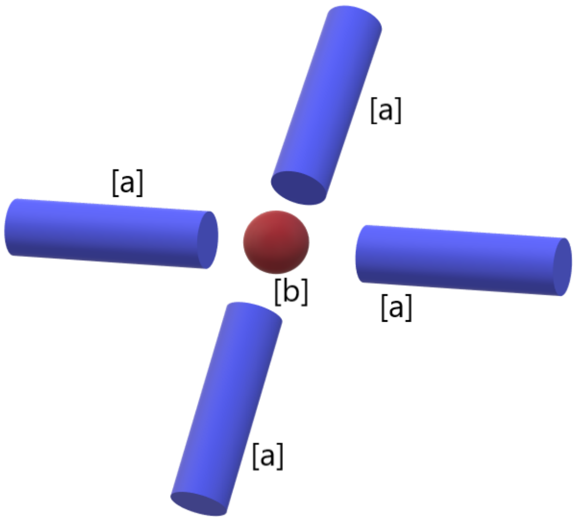

Figura 1.3: Zoom dei pori del pore network
[a] pore bodies, [b] node

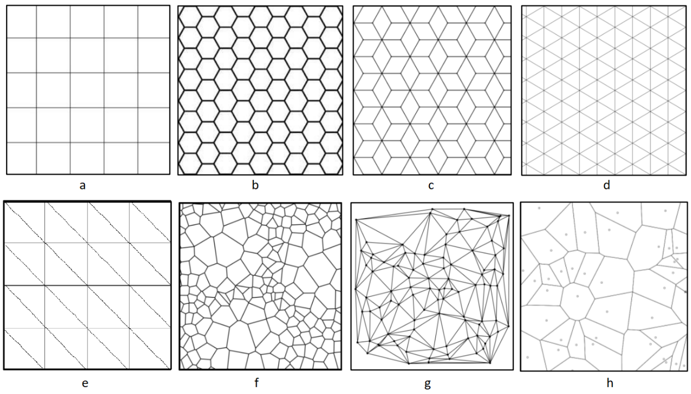

Figura 1.4: Varie tipologie di pore networks, modificato da Ledezma
(a) square, (b) single hexagonal, (c) double hexagonal, (d) triple hexagonal, (e) triangular, (f) Voronoi tessellation, (g) Delauney tessellation, (h) Voronoi-Dirichlet

Inoltre al fine di dare maggiore eterogeneità alla struttura e alla sua topologia, è possibile considerare vari diametri a seconda degli input dati.

Per dare un'idea dell'influenza dei vari parametri precedentemente descritti viene visualizzata una panoramica delle tipologie della griglia.

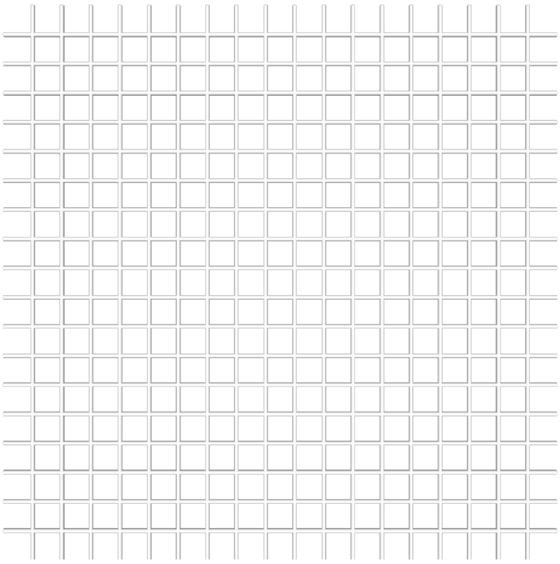

Figura 1.5: Pore network with a regular lattice and constant diameters.

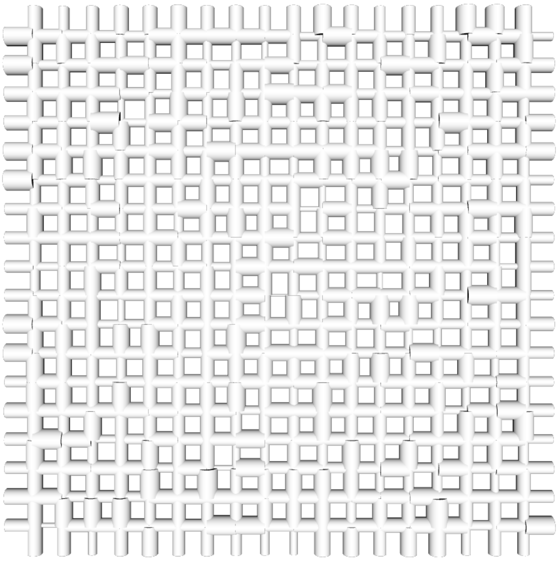

Figura 1.6: Pore network with a regular lattice and gaussian distribution in the pore diameters.

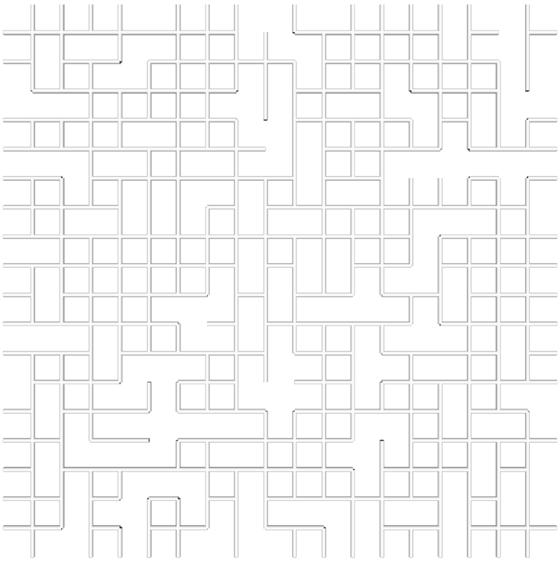

Figura 1.7: Pore network with a regular lattice and a pore existence probability of 0.75. Nodes have a mean connectivity of 75% of what they would have in a complete regular lattice.

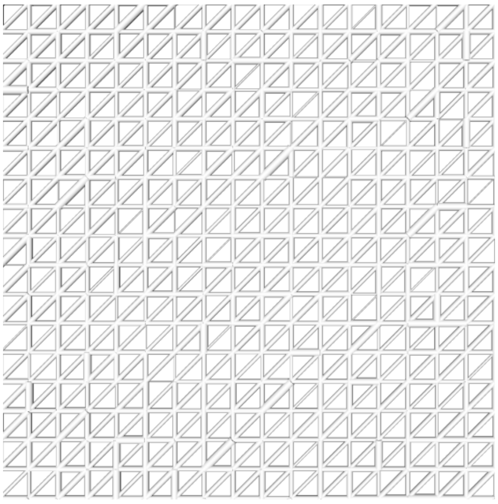

Figura 1.8: Pore network with a triangular lattice and Pore size distribution.

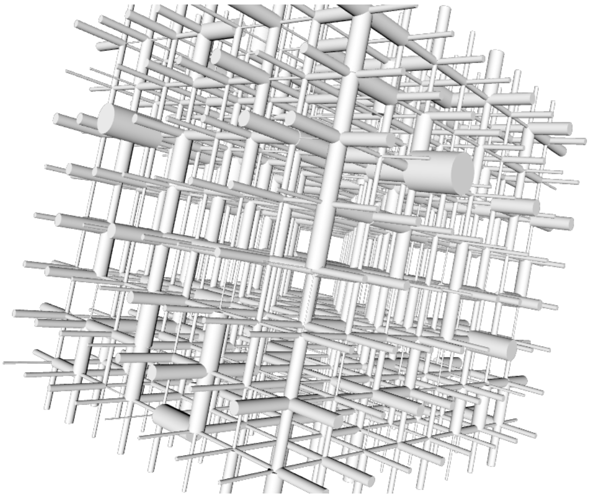

Figura 1.9: 3D Pore network with gaussian pore size distribution

1.8 Diffusione nella rete

La simulazione permette la risoluzione simultanea di un sistema di equazioni alle derivate parziali paraboliche della seconda legge di Fick (equazione 1.8) impiegando collocazioni ortogonali.

$$\frac{\partial \Phi_i}{\partial t} = -\nabla \cdot J_\phi \tag{1.8}$$

Ciascun poro è sottoposto ad un equilibrio tra le specie e la posizione del poro influenza le condizioni al contorno adottate.
Ai nodi interni del reticolo viene assegnata una condizione di Dirichlet, per cui i flussi di massa in entrata e in uscita dal nodo sono equivalenti. Per semplificare i calcoli, i nodi esterni nella rete presentano una concentrazione costante.

In Figura 1.11 è visibile una rappresentazione delle collocazioni, ovvero il luogo deputato alla misurazione della frazione molare (e quindi della concentrazione della specie). Nella figura i rettangoli grigi sono una rappresentazione 2D dei pori, il cerchio blu rappresenta il nodo comune che si sovrappone tra tutti i pori, dove il trasferimento di massa è istantaneo. Inoltre, i cerchi arancioni rappresentano la discretizzazione spaziale chiamata collocazioni ortogonali.
La discretizzazione prevede la divisione in tre collocazioni con la risoluzione in ogni poro di tre equazioni differenziali alle derivate parziali risolte in simultanea, in più vanno risolte anche le equazioni rispetto a ogni collocazione comune a più pori.

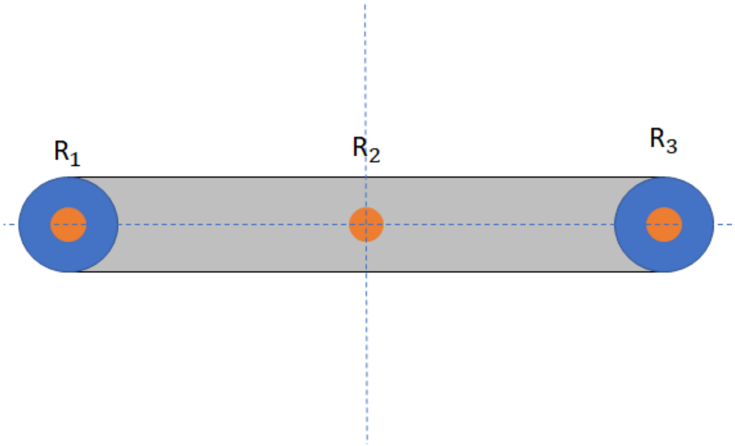

Figura 1.10: Collocation roots in a pore

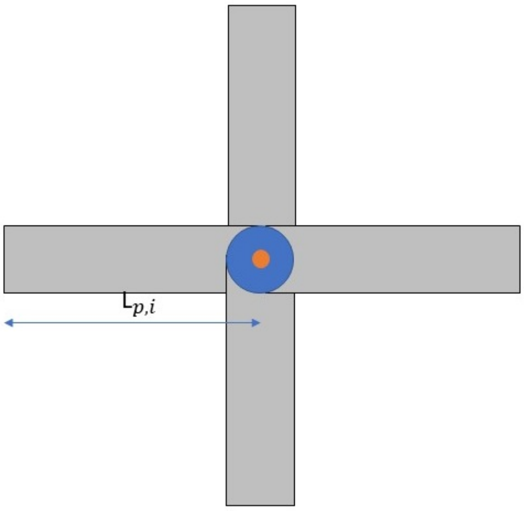

Figura 1.11: 2D representation of the common collocation in pores

Da un punto di vista matematico, considerando due pori sull'asse x, e chiamandoli i e j, i pori sono collegati in quella collocazione per cui:

$$X_{a,i,3} - X_{a,j,1} = 0 \tag{1.9}$$

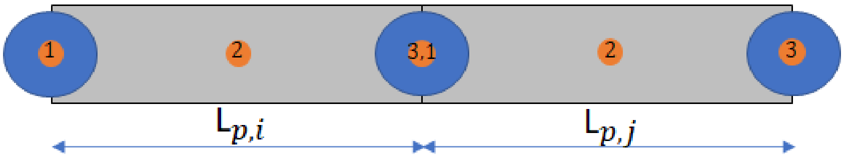

Figura 1.12: Representation of the collocations in connected pores

Per modellare l'autodiffusione viene utilizzato un artificio. Tutte le collocazioni all'interno della rete dei pori sono inizializzate con le stesse molecole al fine di simulare una concentrazione omogenea della sostanza in tutti i pori. In questo modo anche le proprietà fisiche saranno omogenee nella rete.
In uno dei pori, le molecole che vogliamo studiare saranno contrassegnate differentemente permettendo quindi di controllare la frazione molare di questa specie in ciascuna delle collocazioni della rete e di tracciare l'autodiffusione di queste molecole. Si deve quindi scegliere il poro iniziale in cui può iniziare la diffusione e questo poro da questo momento sarà chiamato *tracer pore* con frazione molare X_{tracer}.

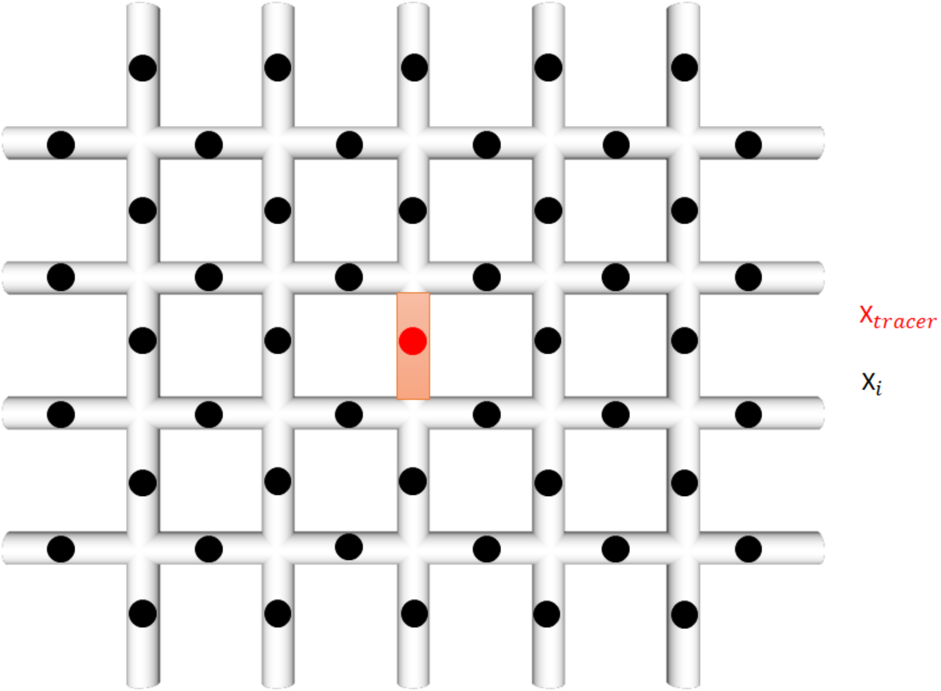

Figura 1.13: Tracer pore inside the pore network, example from Ledezma, 2021

Per prevenire la perdita di massa per fuoriuscita dalla rete, il poro con il tracciante viene scelto in una zona ristretta della rete denominata *zona attiva*.

Per calcolare questa zona, è necessario capire fino a che punto una particella potrebbe viaggiare nella rete dal poro iniziale. Tale lunghezza è calcolata dal coefficiente di diffusione della specie, D, e del tempo di diffusione adottato, Δ parametrizzando la traiettoria di una particella browniana in Formula 1.10 (Griera, 1996).

$$L_d^2 = 2D\Delta \tag{1.10}$$

La zona attiva è una similitudine dell'esperimento reale. La zona attiva rappresenta, infatti, la zona in cui viene misurato il segnale delle molecole con PFG-NMR all'interno del pellet di allumina. In questo caso, nella diffusione, è così garantito che tutte le particelle rimangano all'interno del campione e possano essere misurate.
Il metodo prevede l'utilizzo di una zona attiva costante di un'area di 80x80 nodi. Queste dimensioni sono state infatti scelte perché corrispondono alla taglia di pore network minima per ottenere delle proprietà di trasporto della massa (in scala micrometrica) e di proprietà texturali ottenute in simulazioni numeriche similari (Ledezma, 2021). Per alcuni calcoli è stato utilizzato il sistema HPC-Polito.

1.9 Algoritmo

Una sequenza ben definita è fondamentale per comprendere e riprodurre i risultati ottenuti nelle simulazioni.

Come è visibile in Figura 1.14, per rappresentare la reale tortuosità della rete dei pori, i tracer pores devono essere scelti casualmente ed è necessario verificare che non siano stati già presi in precedenti simulazioni. Infatti, ciò avrebbe un impatto sul calcolo della tortuosità del sistema delimitando la zona che viene analizzata. Sono quindi necessari numerosi e in varie zone pori traccianti. Si fa quindi la media dei risultati del segnale ottenuto, si estrapola il coefficiente di diffusione e si ottiene la tortuosità, mediante l'equazione 1.7.

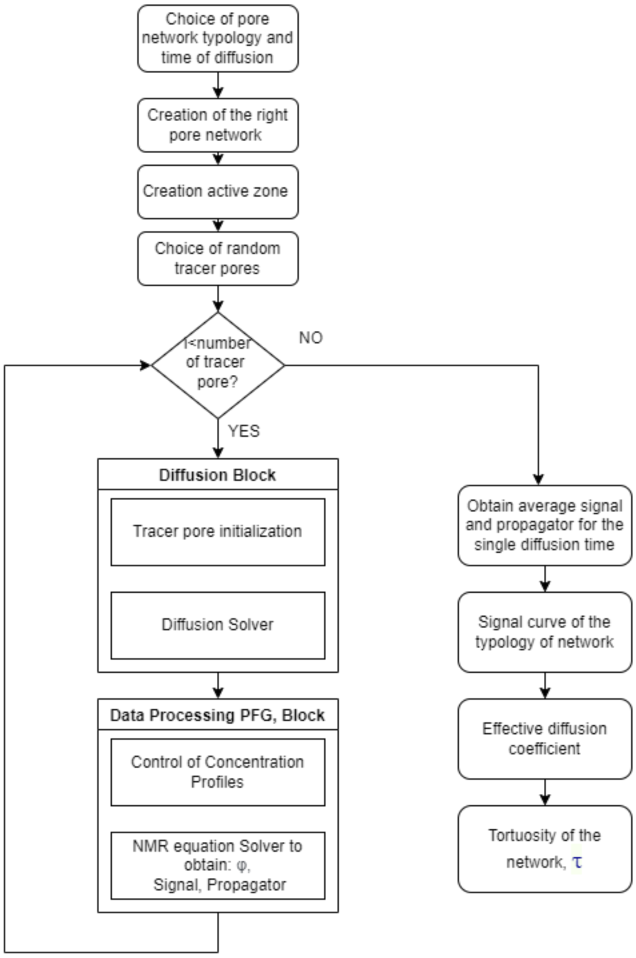

Figura 1.14: Algorithm of the simulation, i is the counter of tracer pores

1.10 Simulazione della tecnica PFG-NMR

1.10.1 Dati sperimentali

Un background sperimentale è stato necessario per un confronto realistico. I dati necessari per implementare la tecnica e validare i risultati sono stati forniti dalla tesi di Aleksandra Glowska (2021)

La diffusione di Acetonitrile liquido, CH_3CN, all'interno della rete porosa è stata caratterizzata in laboratorio mediante la tecnica PFG-NMR. L'acetonitrile ha un caratteristico γ, rapporto giromagnetico, di 2,67 x 10^8 ($\frac{rad}{sT}$), una massa molare di 41,053 ($\frac{g}{mol}$) e una densità a 25°C di 0,786 ($\frac{g}{cm^3}$).

Nelle stesse condizioni, è stato misurato il coefficiente di autodiffusione in assenza di restrizioni D pari a 1.897 x 10^{-9} ($\frac{m^2}{s}$). Questo valore verrà utilizzato come riferimento nella simulazione numerica.

La principale differenza tra il lavoro svolto nella sua tesi e nelle sezioni seguenti è che Glowska, utilizzando l'apparato PFG-NMR, ha modificato l'intensità del gradiente per modulare il segnale. In questo lavoro, tuttavia, l'intensità del gradiente è fissa e il tempo di diffusione viene variato tra 5 ms e 200 ms.

1.10.2 Metodologia

L'intensità del campo magnetico è considerato lineare e dipendente rispetto alla posizione sull'asse x nella rete. Nel caso sperimentale, il massimo del gradiente è al centro del campione e il modello tenta di replicare questo fenomeno. Nella simulazione il campo magnetico è considerato lineare (Kittler, 2017) e calcolato attraverso:

$$B(x) = -mx \tag{1.11}$$

Dove m è il gradiente (positivo) e x la posizione nella rete della collocazione in cui è misurata la concentrazione.

ϕ, la fase, è considerata una variabile temporale. Viene utilizzato al termine della diffusione e della sequenza di impulsi.

Utilizzare il vero coefficiente di diffusione significa dover modellare la diffusione all'interno di reti porose molto grandi. Il tempo di risoluzione necessario potrebbe arrivare a vari giorni di calcolo. Per risolvere questo problema considerando il fatto che il vero interesse è il calcolo della tortuosità della rete, è possibile utilizzare un coefficiente di diffusione molecolare di vari ordini di grandezza minore di quello reale. Questo permette di lavorare con reti molto più piccole abbassando in maniera significativa il tempo di calcolo.

La dimensione minima della rete è stata scelta tenendo conto di simulazioni precedenti di porosimetria ad azoto nelle quali era stata ottenuta una buona rappresentazione statistica della topologia. Una volta determinata la dimensione minima

è possibile scegliere un coefficiente di diffusione proporzionale a quello reale che garantisce il bilancio di massa all'interno della rete.
Lo sviluppo della metodologia ha determinato una scelta anche nel gradiente magnetico. Il gradiente ora utilizzato è pari a 0,086 $(\frac{T}{m})$ e calcolato supponendo la stessa variazione percentuale del gradiente nella rete simulata che si ha negli esperimenti di Glowska tra il valore di gradiente più alto e quello più basso della macchina.

Nelle simulazioni, la concentrazione viene misurata su scala nano e mesoscopica, pertanto il campo magnetico va modulato in base a questi ordini di grandezza. È stato, quindi, necessario aggiornare a un valore nell'ordine delle macchine più potenti utilizzate in PFG-NMR con un valore di $86(\frac{T}{m})$. Questo valore è anche maggiore rispetto alle macchine standard PFG-NMR presenti sul mercato, ma rimane sempre nello stesso ordine di grandezza.
Il calcolo del defasamento avviene a partire dall'equazione 1.3 utilizzando delle semplificazioni dovute alla tipologia di gradiente applicato e supponendo che lo spostamento durante l'impulso, che avviene nel tempo δ secondi, sia nullo. L'impulso a radiofrequenza B_1 consente di cumulare la fase, il defasamento cumulativo è calcolabile da:

$$\phi(2\tau) = \left\{\gamma g x_0 \int_{t_1}^{t_1+\delta} dt\right\} - \left\{\gamma g x_f \int_{t_1+\Delta}^{t_1+\delta+\Delta} dt'\right\} = \gamma g \delta (x_0 - x_f) \tag{1.12}$$

Dove x_0 e x_f rappresentano la coordinata iniziale e finale su x della molecola. In questo caso si misura la distanza dal centro del poro tracciante originario alla posizione finale. Allo scopo di ottenere un segnale rappresentativo dell'autodiffusione delle molecole, per ogni tempo di diffusione, che corrisponde a un tempo di misura, è necessario usare diversi tracer pores fino ad avere una deviazione standard del segnale minore del 5%. La media dei segnali viene calcolata tramite l'equazione 1.13. Se i pori vengono rilevati con una frazione molare maggiore di 0, vengono considerati nella misurazione del segnale:

$$E_i = \sum_{i=1}^{Np} \left\{ cos(\phi_i(t)) * \frac{S_i * L_i * \int_0^{P_{i,L}} X_i}{S_0 * L_0 * \int_0^{P_{0,L}} X_0} \right\} \tag{1.13}$$

$$\sigma = \sqrt{\frac{1}{N_{tracerpores}} \sum_{i=1}^{N_{tracerpores}} (E_i - E_{av})^2} \tag{1.14}$$

Una volta trovato il segnale per ogni tracer pore, il segnale medio per ogni tempo di diffusione è rappresentato dalla media di ogni segnale.

$$E_\Delta = \frac{1}{N_{tot}} \sum_{j=1}^{N_{tot}} E_j \tag{1.15}$$

Per trovare il valore di attenuazione del segnale va valutato il δ. Il metodo utilizzato è una calibrazione con un unico poro (un lungo tubo in cui il tracciante non fuoriesce) in cui si può ipotizzare che il coefficiente di diffusione ottenuto dal segnale è uguale a quello ideale perché la tortuosità è equiparabile a 1, come in una libera diffusione.
Per il poro unico, si ottiene un δ di 1x10^{-5}. Usando la stessa metodologia ma cambiando il poro standard in una rete di pori regolare si ottiene lo stesso delta. La stessa idea può essere replicata anche in una rete di pori 3D ideale.
L'attenuazione del segnale permette di ottenere il coefficiente di diffusione effettivo, D_{eff} come coefficiente angolare della retta interpolante. Sull'asse x, il valore utilizzato deriva dalle equazioni teoriche del PFG.
Per quanto riguarda il caso 3D per via della maggiore CPU richiesta, è stata implementata una variazione nella dimensione della rete.
La rete utilizzata è composta da un reticolo di 10x10x10 e per evitare la perdita di particelle, il coefficiente di diffusione utilizzato per le simulazioni di diffusione è stato diminuito di due ulteriori ordini di grandezza ottenendo, D=1,897e^{-15}. Con la stessa metodologia di calibrazione vista per i reticoli 2D, si ottiene un δ=6e^{-5}.

1.11 Risultati

I risultati analizzati in questo riassunto rappresentano solo alcune delle conclusioni che si possono trovare nella tesi completa di seguito.
Le differenti tortuosità delle reti 2D e 3D sono state paragonate poi a risultati sperimentali e di simulazioni numeriche con altre tecniche di caratterizzazione come la piastra semi-infinita (Ledezma, 2021).
Tutte le reti 2D hanno delle caratteristiche in comune:

Tabella 1.1: Parametri utilizzati in reti 2D

Parameter	**Value**
L_{pores} (nm)	60
G($\frac{T}{m}$)	86
δ(s)	1x10^{-5}
$\gamma\left(\frac{rad}{sT}\right)$	2,67x10^{8}
D $\left(\frac{m^2}{s}\right)$	1,897x10^{-13}

Nella Figura 1.15 si può apprezzare un esempio di curva di attenuazione. Essa è il risultato della caratterizzazione di una rete con pore existence probability (PEP) uguale a 1 e pore size distribution (PSD) con diametro medio 20 nm e deviazione standard 2 nm.

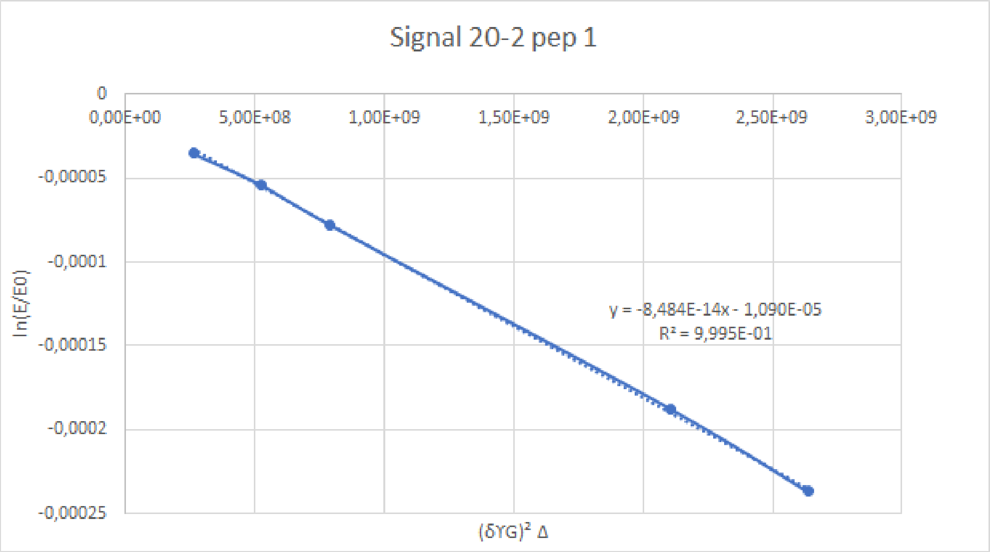

Figura 1.15: Signal attenuation in a pore network PEP 1, Diameter 20 nm, deviation 2 nm

Il valore di tortuosità ottenuto da questa rete è pari a 1,12.
Tra i risultati ottenuti è stato verificato che diminuendo la PEP, la tortuosità aumenta. Questo è dovuto al fatto che la connettività media della rete diminuisce. Modificando il diametro dei pori, le curve di attenuazioni hanno andamenti similari a ciò che è stato visto in Figura 1.15, e i risultati numerici delle tortuosità si trovano nella tabella 1.2, è presente aanche una colonna che dimostra che la variazione di deviazione standard ha un'influenza.

Tabella 1.2: Tortuosità di simulazioni con PEP 0,8

Average Diameter (nm)	**Deviation (nm)**	**Tortuosity**
10	2	1,42
20	2	1,51
20	4	1,41
20	5	1,17
50	2	1,33

Figura 1.16: Digital twin γ-alumina, obtained from Ledezma, 2021

1.12 Confronto

La strategia adottata nelle simulazioni 2D può essere replicata e adattata in reti 3D. Queste reti 3D sono concepite per riprodurre al meglio la porosità reale di $\gamma-$allumina, permettono una rappresentazione più fedele e danno risultati ancora più attendibili. Il simulatore è stato validato confrontando il valore di tortuosità misurato su un campione d'allumina e quello ottenuto con la caratterizzazione digitale del digital twin del campione. La topologia del gemello digitale è stata progettata e validata da porosimetria ad azoto (Ledezma, 2021). La deviazione relativa tra i due valori equivale al 21%. Ciò significa che è possibile prevedere il valore della tortuosità di un campione d'allumina partendo soltanto da un gemello digitale.

Tabella 1.3: Universal parameters used in 3D simulations

Parameter	**Value**
G$(\frac{T}{m})$	86
δ(s)	6x10^{-5}
$\gamma\left(\frac{rad}{sT}\right)$	2,67x10^{8}
D $\left(\frac{m^2}{s}\right)$	1,897x10^{-15}

Le tortuosità trovate sia in questo lavoro che nella tesi di Ledezma mostrano una differenza rispetto al lavoro empirico di Glowska. Nella tesi di Glowska, le tortuosità ottenute sono maggiori, e probabilmente ciò è dovuto agli effetti di ostruzione dei pori che in questo caso sono stati mitigati dalla simulazione numerica che non ne tiene pienamente conto. Un'altra pubblicazione che può essere utilizzata per

analizzare i risultati è il lavoro di tesi di Kolitcheff. Egli ha usato una tecnica sperimentale PFG-NMR e ha raggiunto dei risultati che dimostrano che l'uso di liquidi con affinità con la superficie come il toluene portano ad un fattore di tortuosità di 3,5. D'altra parte, l'uso di liquidi non affini permette di ottenere una tortuosità di 1,8 che è conforme con il valore sia di questa tesi che della tesi di Ledezma.
L'ultima pubblicazione utilizzata è un articolo che studia la tortuosità del catalizzatore di allumina mesoporosa (Kolitcheff et al., 2017). In questo articolo, si afferma che i valori di tortuosità per una rete porosa devono essere necessariamente inferiori a 1,9. Questo valore concorda con i risultati numerici ottenuti in questa tesi.

Contents

List of Figures

List of Tables

Chapter 1

Introduction

1.1 Scope

Modeling and prediction of fluid dynamics and chemical kinetics in porous media are sectors with an increasing relevance in the design of engineering apparatuses, from chemical[1] to aerospatial[2] fields. A correct characterization of phenomena involved allows to optimize the modeling and improve processes.

Computer aided synthesis of catalytic materials has been deeply studied in the last years but it has not reached a maturity of prediction comparable to traditional methods of synthesis. Although new advances are reported in many fields like: crystal structures, synthesis of support and dispersion of catalytic particles on the support,further efforts are still needed.[3]

A proper description of the topology of the porous network is vital to understand how to accurately design the catalyst, enhancing the prediction of reactions.

The goal of this thesis is to foresee the tortuosity coefficient of a γ-alumina sample through a numerical characterization of a digital twin. The innovative analysis has been developed through a simulation of Pulsed Field Gradient- Nuclear Magnetic Resonance, PFG-NMR, using the programming language **FORTRAN**.

The digital twin has been reconstructed with a stochastic simulation and the topology of the structure has been obtained and validated by nitrogen-porosimetry numerical simulations.

The results of the digital simulations achieved have been subsequently correlated to the outcomes of empirical experiences that have been both found in literature and in the results of doctorates at the research institute IFP-EN, situated in Lyon, that has also supervised this project.

The work developed creates an innovative methodology to approach porous media and to represent its physical properties, supported by experimental data. In order to understand the results obtained, many concept need to be addressed first:

- Porous media, alumina
- PFG-NMR, theoretical explanation
- Creation of the physical model of alumina
- Modelization of the analysis

Only then, it will be possible to analyse the results and compare them with similar values found in literature.

1.2 Alumina

In order to advance in the analysis, it is necessary to preliminarily understand how porosity is involved.

Porous media have been extensively studied because of their relevant role in the engineering world. As a matter of fact, diffusion and chemical reactions in porous materials appear in several industrial and scientific applications.[4] Filtration, absorption, catalyst support and catalytic activity are only some of the numerous applications that strictly relate to porous media in process engineering.[5] In all these fields, one of the most prominent porous materials is alumina. Alumina is the common name of the aluminium oxide, Al_2O_3. Alumina is a ceramic material, it has been known and used in some form, since at least seven millennia in Mesopotamia. However, only in the last two centuries and especially since the invention of Bayer and Hall-Heroult processes,[6] alumina has been commonly used in commercial applications.[7]

Alumina can be found in the natural world as a mineral called corundum. Aluminium oxides, however, exist as polymorphous materials. This means that they present various phases that are thermodynamically stable (or meta-stable) and each of those is characterized by different physical and chemical properties. Al_2O_3 exploitable in industries, is commonly achieved by a thermal treatment from a mineral precursor called gibbsite, $Al(OH)_3$, which is obtained directly from mining processes.

When partially dehydrated, gibbsite transforms into boehmite (AlO(OH)). Another possible route to obtain boehmite, starts from a monocline mineral called bayerite.[8] In addition to this, as has been evident through numerous studies,[9] several crystal structures of Al_2O_3 are obtainable depending on the intensity of the heat applied, the operative pressure, humidity and the precursor. The first metastable transition form is obtained when boehmite reaches temperature of 500-600 °C. This structure is known as γ-Al_2O_3.[8] At higher temperatures, there is a conversion to δ-alumina with a decrease of surface area and at over 1000 °C, alumina firstly becomes θ-alumina and then reaches the thermodynamic stable phase known as α-alumina (or geologically speaking corundum). Other transition phases are possible like $\eta - Al_2O_3$ or $\rho - Al_2O_3$ but as the temperature rises, alumina inevitably becomes α-alumina, the phase with the lower free energy of Gibbs.[6] The transition with respect to the temperature is visible in Figure 1.1.

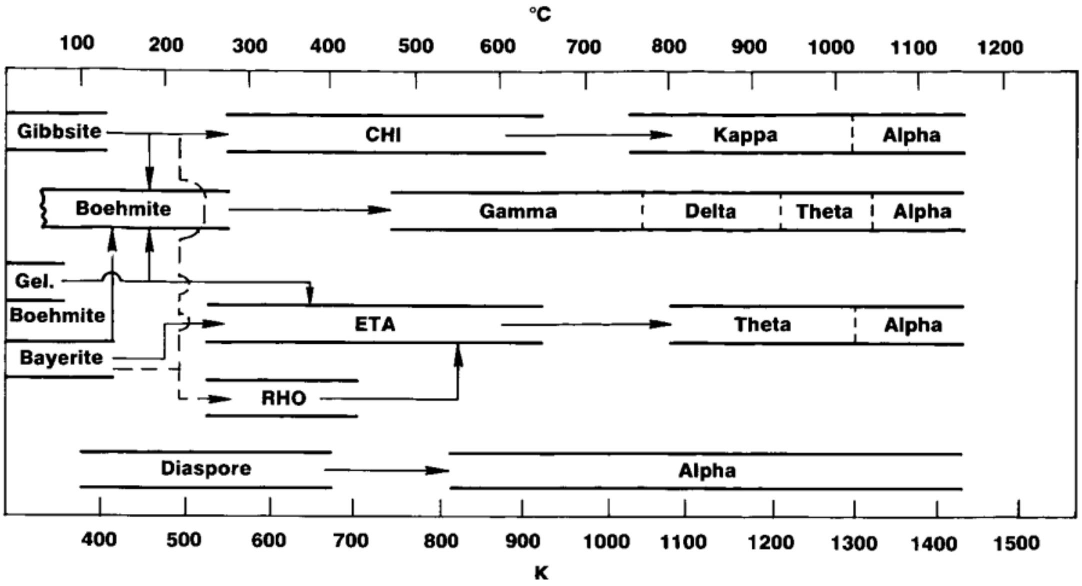

Figure 1.1: Transition sequence forms of $Al(OH)_3 \rightarrow Al_2O_3$. Obtained from.[6]

1.2.1 γ-Alumina

Among all the possible configurations, γ-Al_2O_3 is regarded as the most important transition phase of alumina. It presents the higher surface area, porosity and it has been studied and exploited for the acidity of its surface that promotes catalytic performances.
The industrial significance of this phase is even increasing, as a matter of fact, it is used as a catalyst support in numerous fields where heterogeneous catalysis is involved like automotive (where it covers around 70% of 850000 tons of ceramic materials implicated in the market[10]), cracking and petroleum refining, where can be used for molecules cracking or polymerization,[11] fuel cell applications as a sol-gel support for catalytic steam reforming of methanol or oxidation of gasoline with water gas shift.[12] In addition to these "catalytic" processes, γ-alumina has proved to be useful in a number of different application. It is employed as surface protection and insulation as a ceramic coating to mitigate the flow of electrons due to its high dielectric properties.[13] Another application exploits the low density of alumina to create a micro channel combustor which could improve combustion phenomena in industrial applications enhancing efficiency of mass and heat transfer.[14]

To fully understand how to take advantage of γ-Al_2O_3 and how to reproduce it with a numerical simulation, it is vital to define its structure and its topology. The first atomic description in 1935 portrayed alumina as a cubic spinel like $MgAl_2O_4$.[15]

Afterward, γ-Al_2O_3 has been considered having this structure but with a tetragonally-distorted lattice at low temperatures that varies as the temperature raises.[8] In addition to this, a further burden to overcome is that alumina presents a poorly ordered structure. A single crystal of suitable scale for diffraction analysis is not so easily obtained in laboratory scale,[8] consequently a proper interpretation of the arrangement is hampered and the subsequent representation too. At a mesoscopical scale, alumina structure presents a hierarchical organization, this is a potential explanation of the high porosity of γ-Al_2O_3 that is conflicting with the high tortuosity of the material. It also helps explaining the different tortuosities found among similar samples. This implies that many porosity levels exist inside the network with pores of different diameter that range from 1-2 nanometers up to mm scale.[16]

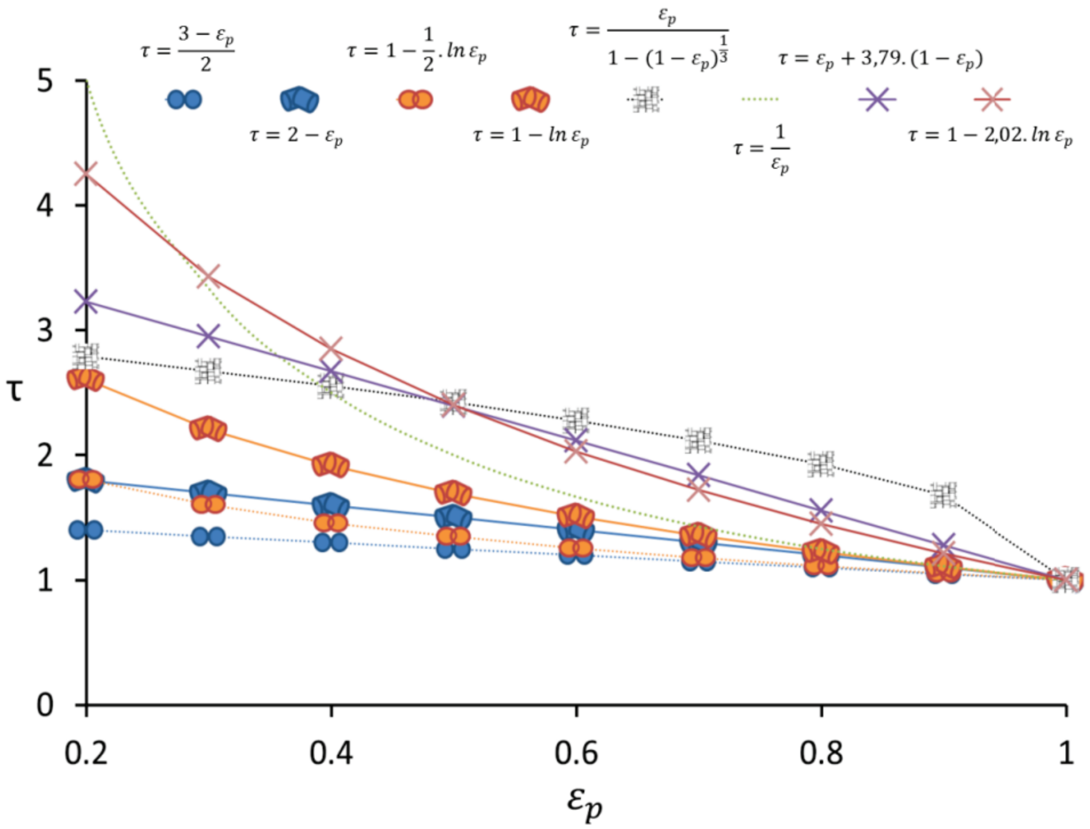

Figure 1.2: Tortuosity with respect to porosity of γ-Al_2O_3. Obtained from.[16]

In fact, in order to investigate and characterize the topology of any porous material (and especially alumina) there are two classes of methods[17] that can be adopted:

- **Reconstruction methods**: represent the pore structure from the real experimental structure data of the material.
- **Mimetic simulation**: the simulation of the material derives from the synthesis processes as a copy to mimic it.

Both these methodologies are widely used for their flexibility and CPU intensity.[18] The first approach will be important in the third chapter of the thesis.

1.3 FORTRAN

The simulation of the diffusion, the PFG-NMR technique and part of the data analysis are coded in FORTRAN 90 using a Visual studio environment. FORTRAN, acronym of Formula Translation, is a compiled imperative programming language developed since 1954 at IBM to execute large mathematical calculations computationally intensive. Due to this, FORTRAN is a common language in the scientific and engineering community and is used in some of the world's fastest supercomputers and HPC, high performing computing.[19] Its longevity caused the development of various versions in order to upgrade the language and modifying it into an Object-oriented programming support. Fortran is so universal that in 1993, Cecil Leith called FORTRAN "the mother tongue of scientific computing".[20] Some of the routines used in the simulations were built in FORTRAN 77 compatible with FORTRAN 90 and are dated as far as the year 1993.

Chapter 2

Pulsed Field Gradient- Nuclear Magnetic Resonance

2.1 Introduction of NMR

Nuclear Magnetic Resonance is a physics Nobel winning phenomenon discovered by Felix Bloch and Edward Purcell research groups at the end of the World War II.[21] NMR in the last century has had a relevant role in the fields of science and engineering providing numerous possibilities.

One of the most prominent grounds is the topic of this thesis: mass transport inside a porous network.

NMR creates the possibility to look inside the porosity like a "spy" providing information of the internal structure and what is happening within, without any external interference.

From 1950 NMR has been adopted to study molecular diffusion within liquids. Subsequently, through the application of gradients with a higher intensity (and with a pulsed field gradients mechanism that will be explained later in this chapter of the dissertation) the use of nuclear magnetic resonance switched also to the analysis of diffusion inside porous materials. Since its discovery NMR has been applied into petrophysical studies in order to study and map the presence of oil and into the geologic formations aiming to recover more hydrocarbons.[22] Many features of NMR signals are related to physical parameters like temperature and viscosity. In order to discern the signal inside the rocks, it is possible to exploit the different physical properties of bulk water and oil to deduce the concentration of the two liquids.

Moreover, surface modifies the properties of the molecules of the liquids because of possible interactions (like adsorption) with the walls, so it can be adopted to collect information regarding the pore size distribution and the permeability of the

fluids. Another possibility that has seen the use of NMR is the measurement of water diffusion inside zeolites, a microporous material typically employed in chemical engineering as a catalyst, catalyst support and molecular sieve.[23] In the first experiments with NMR with a primordial synthesized zeolite, it was found that the diffusion of neat water was comparable to the one within the porosity. This baffled the chemist Bloch and allowed to understand that mass transport inside porosity has a resistance due to the different crystallites present in the bulk of the zeolite that has to be taken into consideration.[22]
Furthermore, NMR has had a great success in the biological fields where complex structures can be approached as a porous medium[22] . With studies on HeLa cells (immortal cell line of a human cervical tumor used in scientific research[24]) it was possible to obtain results in the growing field of MRI (Magnetic Resonance Imaging) and with studies on biomolecules when NMR is used as a spectroscopy instrument it is possible to obtain spectra of protein structures previously modeled.[21]

NMR has not yet expressed all its possibilities and it is still a significant subject of discussion. In fact, with a scheduled cadence, International Bologna conferences are organized since 1990 to examine the breakthroughs in the field.

Table 2.1: Timeline of NMR development. Obtained from.[22]

1946	Discovery of NMR by Bloch (Standford) and Purcell (Harvard)
1948	Russell Varian files patent for Earth's-field NMR magnetometer
1950	Spin echo, Hahn (U. Of Illinois)
1952	Russell Varian files patent for Earth's-field NMR well logging
1953	Nobel Prize in physics awarded to Bloch and Purcell
1954	Carr and Purcell devise spin-echo pulse train Harold Schwede (Schlumberger) files patent application for permanent magnet well logging tool
1956	Discovery of reduced fluid relaxation time in porous media by Brown, Fatt and others
1960	First Earth's-field NML tool – Chevron Research Lab and collaborators
1960s	Laboratory and theoretical studies in various university and petroleum laboratories of the effect of restricted diffusion of T1 and relationship of T1 and permeability
1960s	Several companies offer NML commercial logging service NML fails to live up to advance billing; NML gains bad reputation in petroleum industry
1978	Schlumberger introduces new, improved NML tool
1978	Jackson at Los Alamos, invents first 'inside-out' pulsed RF NML logging technique
1980	Laboratory demonstration of Los Alamos technique
1983	Proof-of-principle demonstration of Los Alamos logging technique at Houston API test pit
1984	NUMAR formed to commercialize advances in medical NMR technology Schlumberger begins development of permanent magnet/pulsed NMR technique
1985	NUMAR obtains license for Los Alamos inside-out NMR patent
1985	NUMLOG demonstrates increased S/N for new magnet/RF scheme in laboratory scale model
1989	First field test of full scale NUMAR logging tool in Conoco test hole, Ponca City, OK
1990	NUMAR announces commercial availability of MRIL logging service based on Series B single frequency tool
1992	Schlumberger starts field test of skid-type pulsed NMR tool
1993	Numar and Western Atlas sign cooperative agreement for MRIL services
1994	NUMAR introduces dual frequency MRIL Series C tool Western Altas logs MRIL in combination with conventional tools
1995	Schlumberger announces commercial introduction of CMR tool Peoples Republic of China purchases two logging systems from Western Altas, including MRIL
1996	NUMAR and Halliburton sign cooperative agreement for MRIL services
1997	Halliburton buys NUMAR
1990s	Laboratory and theoretical studies of the effect of restricted diffusion on T2 (most NMR logging data use T2)
2000	NMR logging-while-drilling prototype

2.2 Theory of NMR

The previous section briefly explained the advancement of NMR and how it is applied in modern life in biological and chemical fields. This section is developed in order to understand the theoretical fundamentals of nuclear magnetic resonance and the related mathematical expression.

As stated by the discoverer E. Purcell, nuclear magnetic resonance is a physical near-field phenomenon. When placed in a strong constant magnetic field, atomic nuclei, and perturbed by an oscillating field, react by producing an electromagnetic signal with a characteristic frequency that depends on the magnetic field at the nucleus. When the frequency of oscillation of the radiation is equal to the frequency of the nuclei, the process of nuclear magnetic resonance occurs.

Firstly, it is needed to explore the spin of the atomic nuclei. Spin is an intrinsic form of angular momentum carried by the particle itself.[25] Nuclear magnetic moment arises from the spin of protons and neutrons in the nuclei. The nuclear spin is not associated to a real rotation of the particle but to an intrinsic property, however in order to get an idea of what the spin is, it is possible to associate it to the rotation of macroscopic objects. Spin is in fact described as a vector.

Spin depends only on the type of particle taken into account and is invariable. The spin-statistics theorem states that two values of spin are possible. Photons, gluons and bosons are described by Bose-Einstein statistics and retain an integer spin. On the other hand, fermions such as quarks and leptons (and therefore neutrons, protons and electrons) follow Fermi-Durac statistics having an half-integer spin.[26]

Moreover, fermions' half-integer spins are present in two states: up and down, that can be related to the sign of the vector of the spin of the particles. Up is a positive half-integer ($+1/2$) and down the opposite ($-1/2$).

However, it is not possible to identify with certainty the spin of a singular particle, therefore, it is needed to approach the total spin using an ensemble of a population following the Boltzmann distribution and looking for the probability of a certain state.

In addition to this, it is possible to modify the orientation of the ensemble applying an external magnetic field and unifying the total orientation.

2.2.1 Spin theory

Representing ideally the atomic nuclei as spheres, each of the nuclei possesses a magnetic moment, a vector with a recognizable direction. Without the application of an external magnetic field, each of the nuclei has a spin that points to a random direction. In order to measure the deviation of the spins, it is vital to obtain a common initial state, polarizing the system to a single direction. However, the spin is still present and it creates a precession of its vector (which is inclined) about the external magnetic field B_0.
Precession is a change in the direction of the rotation axis in a rotating body, and the precession frequency of the spin is called Larmor precession (after the discoverer J. Larmor). The external magnetic field torque $\vec{\tau}$ is calculated by:

$$\vec{\tau} = \vec{\mu} \times \vec{B} = \gamma \vec{J} \times \vec{B} \tag{2.1}$$

$\vec{\mu}$ represents the magnetic dipole moment (rad/s), $\vec{B}$ (T) is the external magnetic field, $\vec{J}$ is the angular momentum and γ is the gyromagnetic ratio, a constant that is related to the characteristics of the nuclei and gives a correlation between magnetic and angular moment through a ratio $(\frac{rad}{Ts})$.

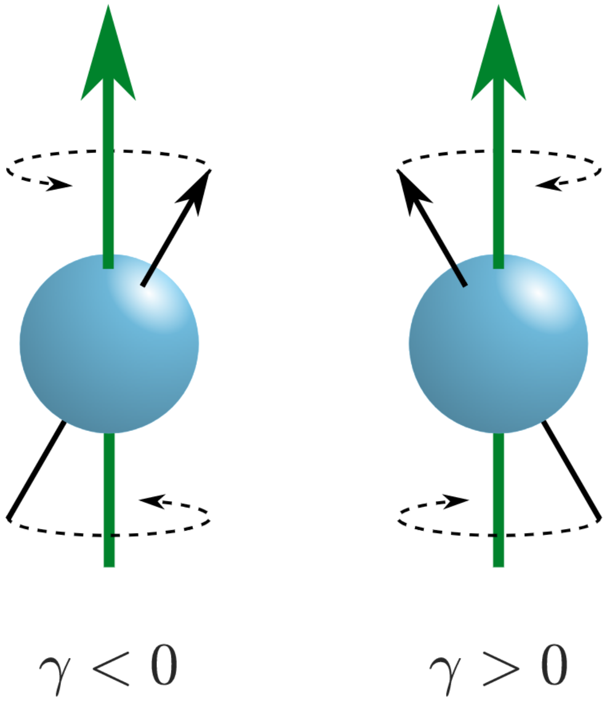

Figure 2.1: Precession of the spin in a particle with respect to the sign of the Gyromagnetic ratio. Obtained from.[27]

The magnetic dipole moment is a function of γ and $\vec{J}$ which represent the angular momentum vector. $\vec{J}$ precesses about the external field with a known angular frequency called Larmor frequency.

$$\omega = -\gamma B_0 \tag{2.2}$$

B_0 represents the intensity of the external magnetic field, is oriented in the z-direction and is spatially homogeneous. γ is the gyromagnetic ratio. As a result, ω is a constant of a sample when a specific magnetic field is applied.
The spins that are precessing about z present a higher population in the lower energy level which is at $+1/2$ and the net magnetic moment is pointing towards the direction of B_0.[18] The static magnetic field modifies the ground energy levels of the nuclear state causing a splitting called nuclear Zeeman splitting. NMR is in fact the spectroscopy of the nuclear Zeeman sublevels.[25]

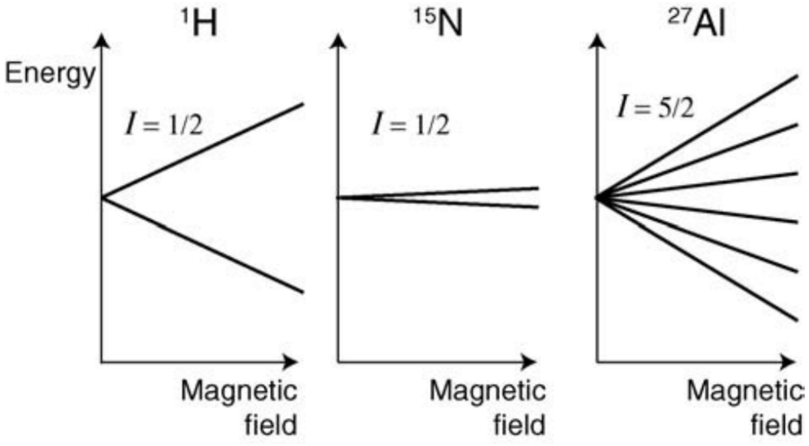

Figure 2.2: Nuclear Zeeman sublevels of different nuclei. Obtained from.[25]

2.2.2 Time and relaxation

The magnetic field B_0 align the spins and abruptly creates a common state.
In order to obtain the deviations it is needed to use an alternating magnetic field B_1 with the same Larmor frequency as the spins and pulsed with a wanted sequence. When the energy of the pulse equalizes the energy level of the population at the resonance frequency of the nuclei, the vertical component of the magnetic moment is neutralized and only the horizontal direction remains, obtaining a component in the transversal plane, that is measured. The net magnetic moment obtained is called transverse magnetization.

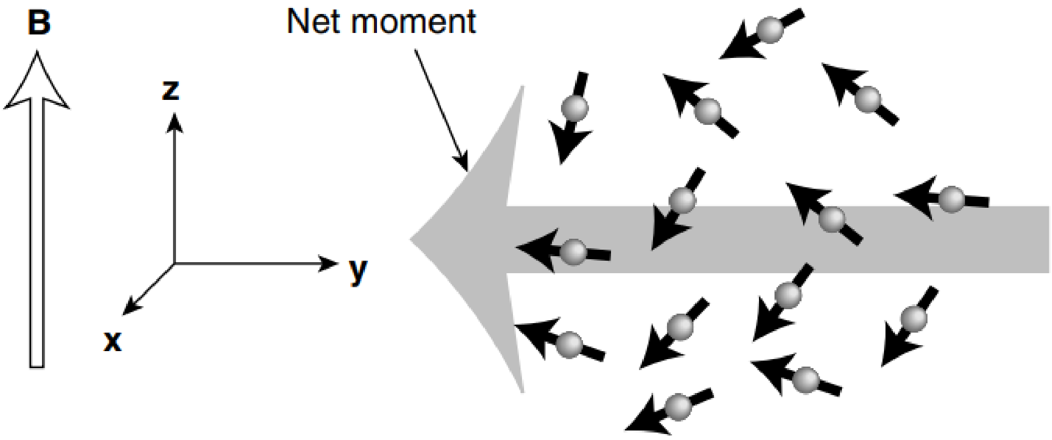

Figure 2.3: Polarization of the transverse magnetization vector. Obtained from.[25]

The production of the transverse magnetization induces a signal in the detector that is then amplified. The return of the longitudinal component of the magnetization vector back to the original status is called spin-lattice relaxation and the loss of coherence (characteristic of the spins to have transverse polarization vectors, visible in Fig. 2.4[25]) is called spin-spin relaxation.[28]
The relaxation is divided into two processes and is characterized by two separate time constants:

- $\mathbf{T}_1$: Responsible for the loss of resonance after the pulse.

- $\mathbf{T}_2$: Affecting the coherence of the magnetization vector perpendicular to the field B_0.

$\mathbf{T}_1$ is the time needed for spins to align with the external magnetic field, growing from zero magnetization in z up to 63% of the maximum value after being exposed to a 90° pulse, which is a valuable information for the NMR technique. $\mathbf{T}_2$ is at a lower scale than $\mathbf{T}_1$ because transversal relaxation is faster than longitudinal. This relaxation arises from the interaction between spins, so that the $x-y$ magnetization in this plane while in resonance, dephasing by precessing at different frequencies, decays by the 69% of the initial value in this time. T_2 is therefore the time that the spins take to lose the phase coherence. Similarly to T_1, also T_2 is a valuable characteristic for the NMR technique.[28][18]
In order to look for a higher precision, it is vital to also determine the errors present in the signal. The first error is related to the field B_0 that can present inhomogeneity and therefore, the intensity of the field may locally vary. Secondly,

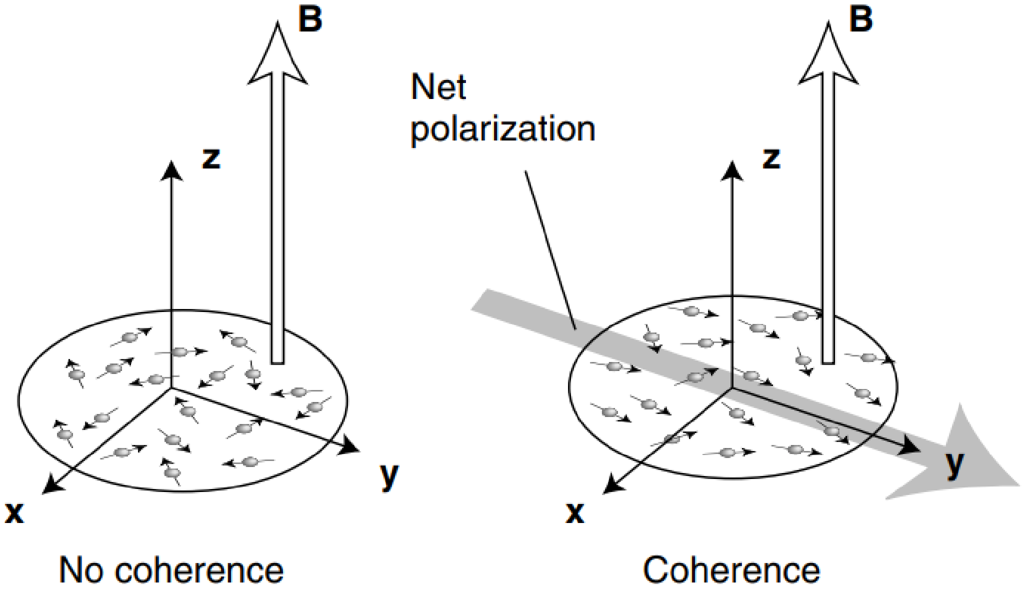

Figure 2.4: Alignment of spins in the transversal plane. Obtained from.[25]

molecular electrical interactions in the chemical environment may lead to induced fields with magnetic moments influencing the measurement.
The field inhomogeneity creates a relaxation process that strictly depends on the location of each molecule. Thanks to the possibility to control this obstacle,[29] it was possible to expand the prospect of use of NMR, growing new techniques like PFG-NMR.

2.2.3 Signal

To sum up, the application of a pulse of radio-frequency close to the Larmor frequency, equalizes the population and create coherence for the spin (hence pointing in the same direction in a rotating system). The total magnetization is measured perpendicularly to the magnetic field. The observable NMR signal generated by the nuclear spin magnetization precessing about the magnetic field is called free induction decay (FID).
The spins follow the direction of the field, generating a rotating magnetization that is detectable. The variation of the magnetization vector in the sample situated in the NMR spectrometer (which can be idealized as a coil) induce a voltage, that results in a signal.
The signal obtained is related to T_2 and T_1 but the only component that is assessed, is in the transversal direction. The curve of the signal obtained has the frequency

of ω and the initial amplitude is proportional to the magnetization moment.[18]
In order to obtain a proper signal and avoid the errors in the measurement, different pulse sequence called Inversion-Recovery and Spin-Echo are usually exploited .
Inversion-Recovery consists in a 180° pulse, the magnetization moment is inverted with respect to B_0 and becomes antiparallel to the magnetic field. Then, a subsequent 90° pulse is sent so that the actual magnetization vector is detectable in the transverse plane. This sequence allows to measure T_1 as the time of the recovery rate.[28]
The Spin-Echo sequence starts by exciting the spin system with a 90° pulse, the spins dephase in the transversal plane, then a 180° pulse allows a refocusing. The faster spins with the pulse at 180° have to recover the space left behind and this mechanism creates an echo in the signal and enables the measurement of T_2. If multiple echoes are sent, T_2 is reflected by the envelope of the peaks of the echoes.

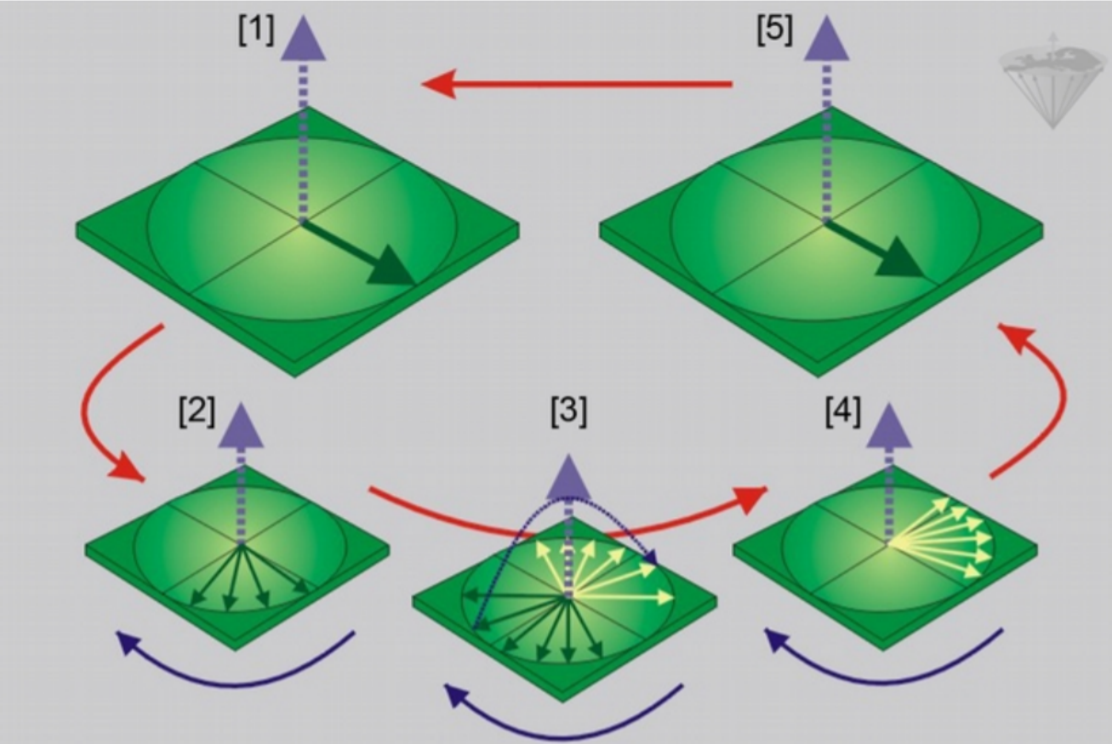

Figure 2.5: Spin-echo experiment
excitation by a 90° pulse, (2) dephasing, (3) 180° pulse, (4) the faster spins now are behind the slower, (5) returning to the original position they create an echo. Obtained from.[28]

The dynamics of the magnetization and its mathematical treatment will not be detailed in this report, however the model used in the modern NMR was described by Bloch and Torrey in the '50s. In any case, if it is needed to deepen the knowledge in the field or to understand more about the subject, every doubt can be dispelled in their work.[30]

2.3 PFG-NMR

Because of its noninvasive nature, NMR has proven to be an incredible tool for studying molecular dynamics in chemical systems. The analyses typically focus on self-diffusion coefficients in confined media. Two methodologies can be applied:

- **Analysis of relaxation data**: sensitive to rotational diffusion.
- **Pulsed-field gradient**: measuring translational diffusion.

Analysis of relaxation data obtains the diffusion coefficient by using the Debye and Stokes-Einstein equations. However, to use these equations, many simplifications and assumptions are needed, creating many controversy with the model like the need to know a priori the size of each particle, the relaxation mechanism of the specie and imagining each particle of the species as spherical.[31]

PFG-NMR, also known in literature as PGSE NMR, NMR diffusometry and DOSY NMR, creates the possibility to track molecular ensembles along their diffusion pathways.[32] This technique does not allow to measure the displacement of a single molecule but the best results are found with a displacement distribution along one dimension in a time scale of milliseconds. The PFG-NMR method allows to measure motion by the attenuation of a spin-echo signal from the dephasing of nuclear spins due to the combination of gradient pulses and translational motion of the spins. No assumptions are needed in the experiments but structural boundaries that affect the natural diffusion need to be assessed.[31]

The intensity of the signal of NMR is associated to the spins in resonance which have the same precession frequency, and to the phase polarization of the magnetic moment. The spins, in fact, may lose coherence but conserve resonance.

As it was already mentioned, the static magnetic field B_0 is spatially homogeneous. However, through the addition of a pulsea magnetic field gradient $\mathbf{g}$ (T/m) dependent to B_0 is also added .

$$\mathbf{g} = \nabla B_0 \tag{2.3}$$

It is fundamental to express that when a homogeneous gradient is imposed, the Larmor frequency becomes a spatial label to the direction of the gradient.[32]

$$\omega(\mathbf{r}) = \gamma(B_0 + (\mathbf{g} \cdot \mathbf{r})) = \gamma(B_0 + gz) = \omega_0 + \gamma gz \tag{2.4}$$

Where $\omega(\mathbf{r})$ is the effective frequency and is linearly spatially dependent. The sequence used in order to label the position of a spin is directly connected to the equation 2.4 that gives the basis to measure the diffusion of the species. The approach is visible in figure 2.6 where there is a simplification to the Hahn spin-echo pulse sequence, through a gradient pulse of a time span of δ into each τ period. By using this expedient, it is possible to avoid many experimental limitations because:

1. It is possible to measure more than one diffusion coefficient in the chemical mixture contemporaneously.
2. It is possible to measure smaller diffusion coefficients by using larger gradients.
3. The time, being defined by pulses, is well determined, which is an important feature in restricted diffusion.
4. Since the applied gradients are present as pulses with higher intensity than background gradients, it is possible to eliminate the influence of spin-spin relaxation.

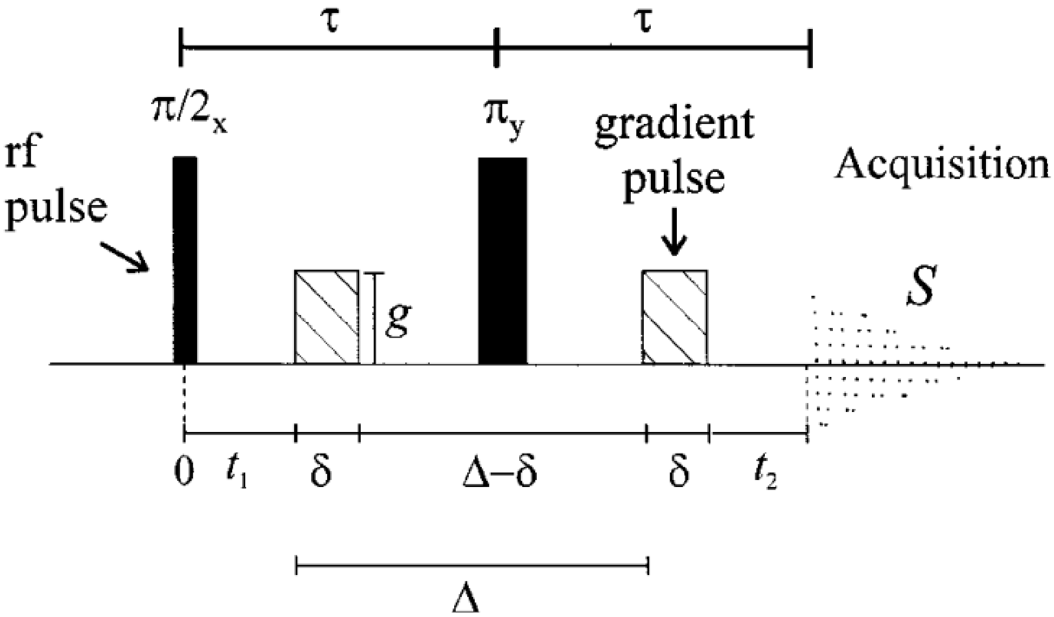

Figure 2.6: Stejskal and Tanner pulsed-field gradient NMR sequence. Obtained from.[33]

The radiofrequency pulse is sent at 90° ($\pi_x/2$) for a few milliseconds to mark the initial position, then a pulse at 180° to rotate the magnetization around the y-axis, inverting the effect of the first gradient. Then, the molecules diffuse and the final position is proportional to the frequency by pulsing the same gradient as the first pulse. The Larmor frequency is not fully recovered and the signal will be lower than the first one.
Therefore, by quantifying the phase difference between frequencies, it is possible to identify the variation of position of the ensemble.

Table 2.2: Gradient intensity with regards to the Stejskal and Tanner sequence.[34]

Gradient intensity	Time interval
$\mathbf{g}_0$	$0<t<t_1$
$\mathbf{g}_0+\mathbf{g}$	$t_1<t<t_1+\delta<\tau$
$\mathbf{g}_0$	$t_1+\delta<t<t_1+\Delta>\tau$
$\mathbf{g}_0+\mathbf{g}$	$t_1+\Delta<t<t_1+\Delta+\delta<2\tau$
$\mathbf{g}_0$	$t_1+\Delta+\delta<t$

By modifying the diffusion time it is possible to obtain various results and a curve that relates signals obtained and diffusion times.

The cumulative phase shift, in the case of a single quantum coherence is found by using:[31]

$$\phi(t) = \underbrace{\gamma B_0 t}_{\text{static field}} + \underbrace{\gamma \int_0^t g(t')z(t')dt'}_{\text{pulse gradient}} \tag{2.5}$$

The equation 2.5 is composed of two terms: the first one concerns the phase shift due to static field, the second one depends on the applied gradient pulse proportionally to γ (that is a constant of the nuclei), the duration of the gradient (t) and the displacement of the spin along the space.

$$\phi(2\tau) = \left\{\gamma B_0\tau + \gamma g\int_{t_1}^{t_1+\delta} z_i(t)dt\right\} - \left\{\gamma B_0\tau + \gamma g\int_{t_1+\Delta}^{t_1+\delta+\Delta} z_i(t')dt'\right\} \tag{2.6}$$

In the methodology used, g is not a function of time as the gradients are known to be rectangular pulses and therefore can be isolated from the integral. Moreover, the limits of the integral are changed and the time of evaluation of the equation is 2τ. Rearranging:

$$\phi(2\tau) = \gamma g\left\{\int_{t_1}^{t_1+\delta} z_i(t)dt - \int_{t_1+\Delta}^{t_1+\delta+\Delta} z_i(t')dt'\right\} \tag{2.7}$$

It is necessary to use an integral because the pulse of the gradient, although having a low period, is not instantaneous.

In order to define the signal, it is vital to stress that an ensemble of nuclei is taken into account at different positions and that the phase shift is promoted by the diffusion and relaxation that cause a signal attenuation.

A phase-distribution P(ϕ,2τ) is used to measure the ensemble of the spins. Where:

$$\int_{-\infty}^{\infty} P(\phi,\Delta) = 1 \tag{2.8}$$

The signal obtained can be described by:

$$S(2\tau) = S(2\tau)_{g=0}\int_{-\infty}^{\infty} P(\phi,\Delta)e^{i\phi}d\phi = S(2\tau)_{g=0}\int_{-\infty}^{\infty} P(\phi,\Delta)cos(\phi)d\phi \tag{2.9}$$

By definition, the integral of the population (equation 2.8) is equal to 1 as it is a normalized function. This definition can be used in the estimation of the signal equation 2.9 that comprehends an imaginary exponential that is modified through the De Moivre's formula.

Relaxation, however, through the use of pulses, decreases its importance.

$$S(2\tau)_{g=0} = S(0)exp\left(-\frac{2\tau}{T_2}\right) \tag{2.10}$$

In the equation 2.10, S(0) is the signal without relaxation attenuation, or the signal right after the 90° pulse. With diffusion and gradient pulses it is possible to derive an equation with independence between attenuation due to relaxation and due to diffusion.

$$S(2\tau) = S(0)\ \underbrace{exp\left(-\frac{2\tau}{T_2}\right)}_{\text{due to relaxation}}\ \underbrace{f(\delta,g,\Delta,D)}_{\text{due to diffusion}} \tag{2.11}$$

The last term of equation 2.11 depends on diffusion with many variables: δ is the gradient duration (that must be lower than Δ), g the gradient intensity (commercially up to 35 T/m[35]), Δ the diffusion time (typically between 1 ms and 1 s) and D the molecular diffusion coefficient. Hence forward this nomenclature will be used.[18]

2.4 Restricted diffusion

The PFG experiment takes advantage of the echo attenuation along the gradient axis that depends on the displacement of the particles. However, the signal does not give a direct measurement of the movement, but needs to be interpreted by a self-correlation function. The self-correlation functions give information regarding the probability of finding a particle in a certain position after a certain time. This function P($\mathbf{r}_0$,$\mathbf{r}_1$,t) is obtained from an analysis of the diffusion, through first and second Fick's laws, and the annexed restrictions due to the topology of the media where the diffusion occurs.

The analysis of the self-correlation function allows to calculate the mean-squared displacement of particles through diffusion.

$$MSD = \left\langle (x(t) - x_0)^2 \right\rangle = nDt \tag{2.12}$$

Mean squared displacement equation: 2.12, MSD represents the variation of position. D is the diffusion coefficient, n represents the dimensions and t the diffusion time. In the case of free diffusion, the mean squared displacement is linear with time. In the case of restricted diffusion an apparent diffusion coefficient is obtained, which is not ideal. What is exactly restricted diffusion? Supposing to have a particle freely moving inside a sphere with reflecting walls, restricted diffusion is a diffusion where the particle placed inside the sphere can not escape from it. It is possible to analyze the restricted diffusion using a dimensionless number:

$$\xi = \frac{D\Delta}{R^2} \tag{2.13}$$

If $\xi \ll 1$, it means that Δ is an infinitesimal value, and the diffusion inside a sphere is free. If $\xi \approx 1$, Δ is a finite value and the particle starts to feel the effects of the boundaries. If $\xi \gg 1$, Δ is a high value, the maximum distance travelled is much lower than how it would have been in free diffusion, the effects of boundaries are evident and the mean squared displacement will become constant. To visualize the effect, figure 2.7:

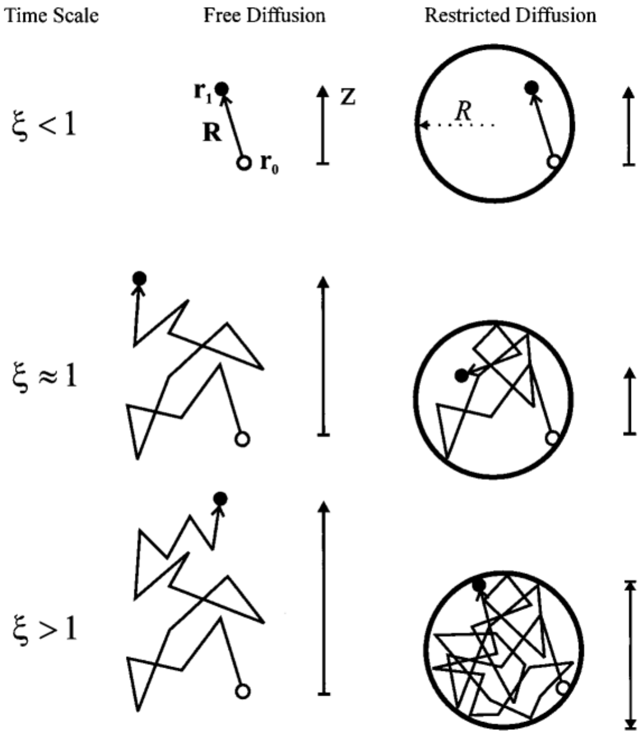

Figure 2.7: Difference between free and restricted diffusion in a sphere. Obtained from.[31]

Therefore, while free diffusion is linear to the time. In the case of a sphere, there are three different situations that need to be addressed and each gives a different typology of signal.
In the presence of diffusion from a time equal to 0 to 2τ

$$ln\left[\frac{S(2\tau)}{S(0)}\right] = ln(E(2\tau)) \tag{2.14}$$

The attenuation is obtained by Price in[31] , the results obtained are visible in equation 2.15:

$$ln(\frac{E}{E_0}) = -\gamma^2 g^2 D\delta^2(\Delta - \delta/3) \tag{2.15}$$

The term $\delta/3$ depends on the finite width of the gradient pulse and the term inside the parenthesis that is composed of Δ and δ. An approximation is possible by knowing that $\delta \ll \Delta$, in that case by repeating the measurement with different intensity of the gradient, the curve of the signals obtained has this shape:

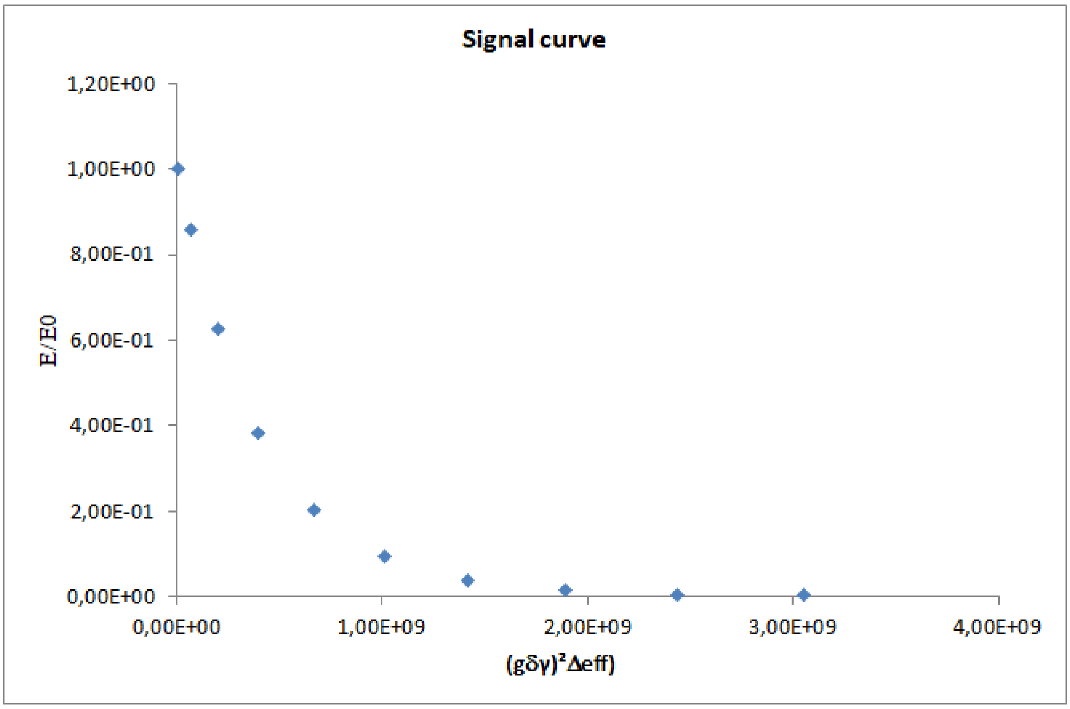

Figure 2.8: Signal attenuation curve of a PFG-NMR experiment of Acetonitrile in a porous network. Modified from[36]

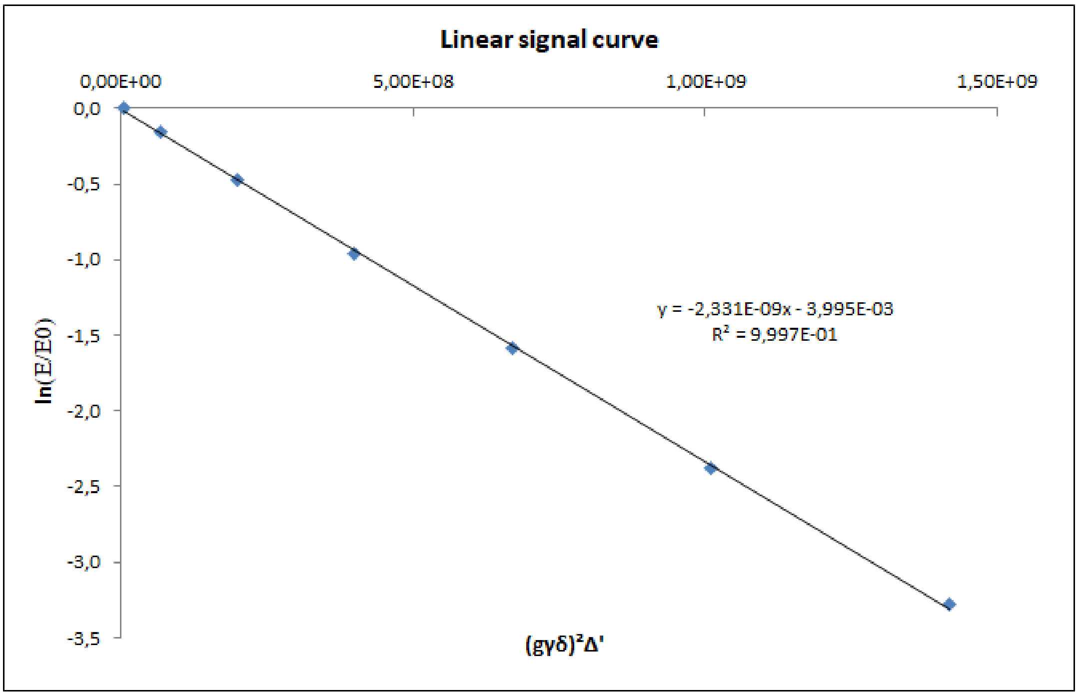

Figure 2.9: Linear signal attenuation curve of a PFG-NMR experiment of Acetonitrile in a porous network. Modified from[36]

If the attenuation is known, it is possible to obtain an apparent diffusion coefficient called D_{eff}. The tortuosity of the network where restricted diffusion is present can be calculated by the ratio between the real diffusion coefficient D and the apparent (effective) diffusion coefficient D_{eff}.

$$\tau = \frac{D}{nD_{eff}} \tag{2.16}$$

n is a factor that takes into account the typology of the network. In a 2D network, n is equal to 2, while in a 3D, it is 3.

2.5 Approximations: GPD and SGP

2.5.1 Gaussian Phase Distribution

This approach approximates the phase distribution used in the signal attenuation as a Gaussian, it means that measuring the displacement after a time shift in a free diffusion regime and in 1-Dimension, it will have the characteristics of a Gaussian.

The phase-distribution function:

$$P(0,z,t) = (4\pi Dt)^{-\frac{1}{2}} exp\left(\frac{-z^2}{4Dt}\right) \tag{2.17}$$

Through some mathematical passages that involves the fact that the integral of a Gaussian variable is also Gaussian, it is also possible to demonstrate that:

$$P(\Phi,2\tau) = (2\pi \left\langle \Phi^2 \right\rangle_{av})^{-\frac{1}{2}} exp\left(\frac{-\Phi^2}{2\left\langle \Phi^2 \right\rangle_{av}}\right) \tag{2.18}$$

Manipulating $\langle \Phi^2 \rangle_{av}$ in the equation 2.18, knowing that the mean-squared displacement is a function of both space and time, eq. 2.19 is obtained. This equation is equivalent to equation 2.15 obtained in the case of pure Spin-Echo sequence.

$$ln(E) = -\gamma^2 g^2 D\delta^2(\Delta - \delta/3) \tag{2.19}$$

Therefore, GPD is a good approximation and can be used to estimate the signal in a diffusion.

2.5.2 Short Gradient Pulse

Short Gradient Pulse represents an approximation that ignores the effects of motion and phase change during the pulse, therefore imagining the pulse as instantaneous (like a Dirac's delta). Experimentally this condition can be achieved if $\delta \ll \Delta$. Neglecting in the phase change the term derived by the static field, equation 2.20 is obtained :

$$\phi(\mathbf{r}) = \gamma\delta\mathbf{g}\cdot\mathbf{r} \tag{2.20}$$

The scalar product is due to the fact that only the direction parallel to the gradient is taken into account in the spin change. If no relaxation happens between the radio-frequency pulse and the gradient pulse, the signal obtained is:

$$E(g,\Delta) = exp(-\gamma^2 g^2 D\delta^2\Delta) \tag{2.21}$$

In case of free diffusion both approximations work consistently with the initial model. However, GPD is a better approximation in a restricted diffusion geometry because the gaussian is preserved even with boundary interactions. On the other hand, SGP only works for $\delta \to 0$. In addition to this, numerical simulation results with brownian motion confirm that GPD is a better approximation in the case of both $\xi<1$ and $\xi>1$, while SGP works well only if the gradient has a low strength.[37]

Chapter 3

Network Simulation

3.1 Introduction

The pore network model used in this thesis was developed during the PhD work of Ledezma at IFPEN. This model looks forward to be a reconstruction of the original γ-alumina. It consists of a stochastic reconstruction that represents statistically the textural properties of the real solid. Using this model, it is possible to create digital twins that will be further characterized using PFG-NMR simulation.[18]
By using this methodology it may be possible to mimic and even predict the performance of crystallites and (in a higher scale) pellets composed by γ-Al_2O_3. In addition to this, it may be necessary to know a priori the scale of porosity that is gonna be studied. For example, in a macroporosity it is needed to consider capillarity differently than in a microporous alumina.
Even the real solid and the digital reproduction do not match exactly but the statistical relevant textural features are comparable and it is obtained a model that represents a good fictitious approximation.

3.2 Introduction to pore network models

The simulation of this thesis is divided basically into two phases:

1. Creation of the pore network, where diffusion occurs.
2. Simulation of the diffusion and treatment of data obtained by a PFG-NMR methodology.

The most fundamental properties of a catalyst are influenced by its physical structure. A proper description is needed because different pore sizes develop different activities and selectivities. The controlled model like the one that was used in these simulations is an example.

Using as a background the work of Wheeler,[38] it is vital to know from a catalyst material: average pore size, pore size distribution and the connection between pores.

Pore network models have nowadays become a routine in many applications.

The first models were simplifications of the pore spaces of the porous media called sphere pack and bundle of tubes. However, they quickly became outdated because of a low capacity of prediction of physical properties. Indeed, sphere pack model has a coherent value, with respect to the real media, only for the estimation of surface area, but does not represent the interconnection of pores. On the other hand, bundle of tubes does not represent accurately the flow properties of liquids inside the porosity but represents fairly well the distribution of diameters in pores. In the 1950s a new model was created by Fatt[39] to represent multiphase flow in porous media. This new model unifies the sphere pack model and the bundle of tubes, obtaining the advantage of having interconnected pores with a proper dimension description. This model, although being a 3-D model, could be even simplified into a 2-D. This reduction of dimensions helps and simplifies the simulation.

By the early 1990s however the interest in pore-scale models diminished because other typologies of models, called predictive, were introduced. Nonetheless, in the last years the interest has returned due to the possibility to explore a large range of phenomena, like the effects of wettability, three-phase flow, hysteresis and mass transfer.[40]

Pore network models have to be defined by their typical features. In this thesis, the lattice was considered composed of two parts: nodes and pores, visible in figure: 3.1.

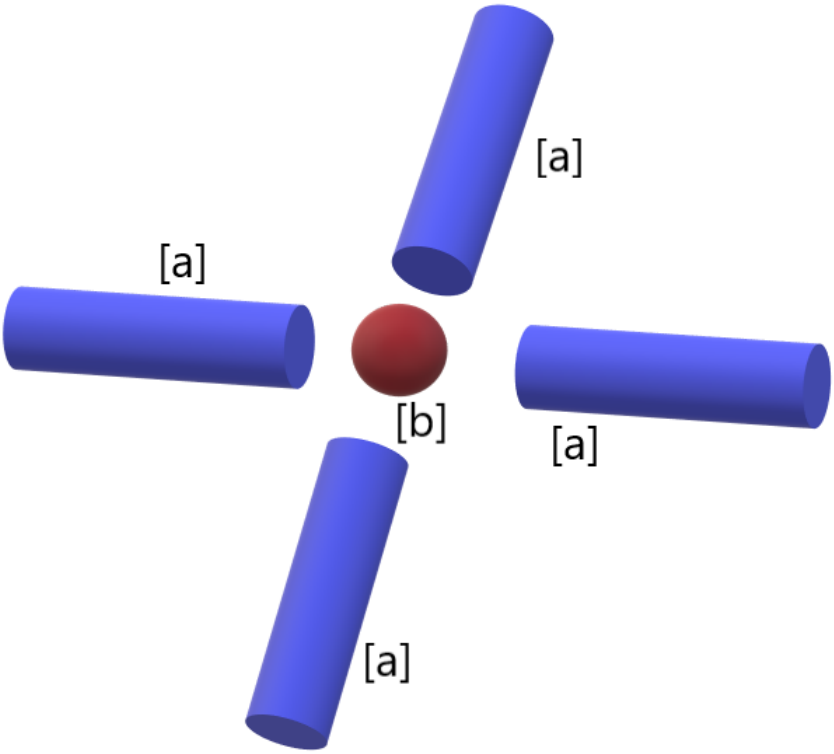

Figure 3.1: Zoom of the pores of the lattice used in the simulation
[a] pore bodies, [b] node

In this work many aspects of a porous network were considered:[18]

- **Pore geometry:** Pores can be simulated with regular geometries like cylinders, spheres or cubes. Each of these influences the mass transport and the diffusion because of the edges present. In addition to this, it is also possible to modify the textural properties like the inclusion of smoothness or roughness in the surface of the pores.
- **Dimension of the pore:** The pore geometry chosen implies the need to assess the dimensions. A cylindrical pore needs both diameter and length, a parallelepiped pore needs two edges (for the basis) and the length etc.
- **Nodes:** Nodes are considered spherical points between the pores with a null volume.

- **Connections**: Connections represent the edges of the pores connected to a node.
- **Architecture and hierarchy:** The lattice can be modified into having pores of different diameter sizes according to a distribution function chosen a priori and different levels of pores can be included in the lattice, reshaping the structure.

As mentioned above multiple geometries can be chosen, in Figure 3.2 some of the various possibilities are shown.

Figure 3.2: Most used pore sections in networks

The cross-section of the pores influences highly the macroscopic properties like mass transfer inside the pores and permeability.[40] However, among all the possible sections available, the most used pores are circular, leading to cylindrical tubes. The network shapes, on the other hand, are much more variegated and tuned to match the experimental data of porous media. When it is chosen the two-dimensional network model, it is chosen also the topology, which can be regular or random.

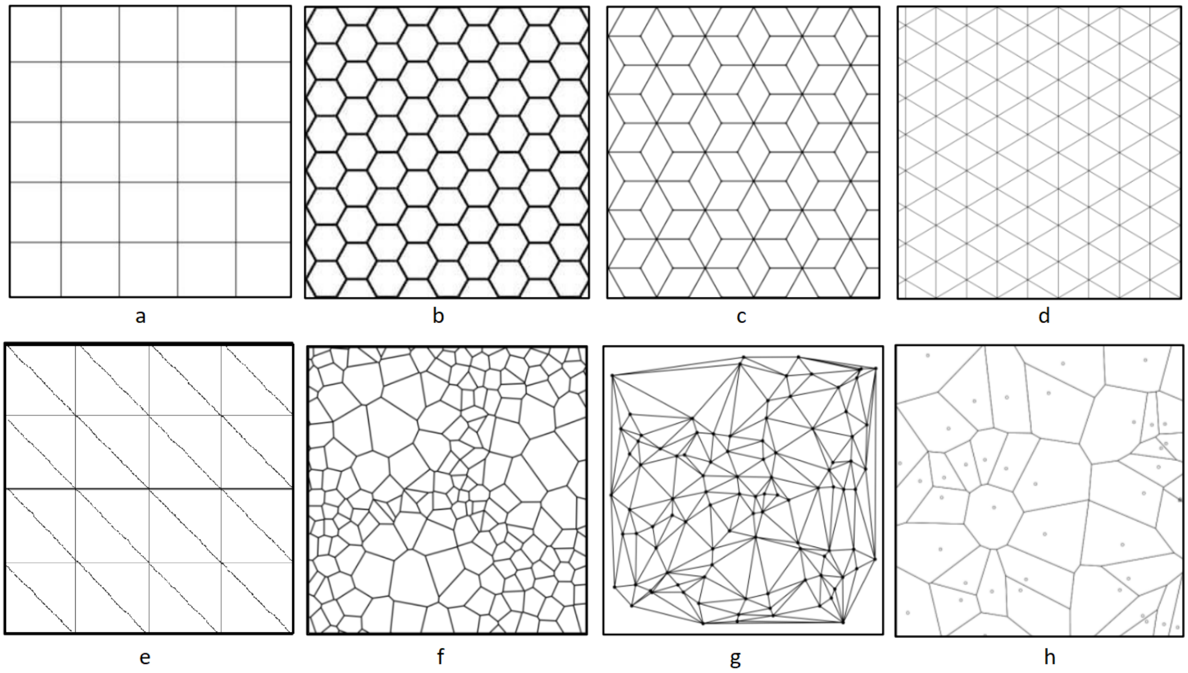

Figure 3.3: Different pore networks, modified from[18]
(a) square, (b) single hexagonal, (c) double hexagonal, (d) triple hexagonal, (e) triangular, (f) Voronoi tessellation, (g) Delauney tessellation, (h) Voronoi-Dirichlet

Thus far, only 2-D network were shown. However, networks in 3-D are a common representation of porous media. In order to perceive the ability to reproduce the real porosity, a 3-D porous network is displayed in Figure 3.4. This network, for example, was used to mimic shale formations and the flow of oil and gas phases through them. It is created by basic elements like cubes with volume to represent pore bodies while nodes (that in this article are called throat) are reproduced without volume but are the only component that provides resistance to the flow of the two phases.[41]

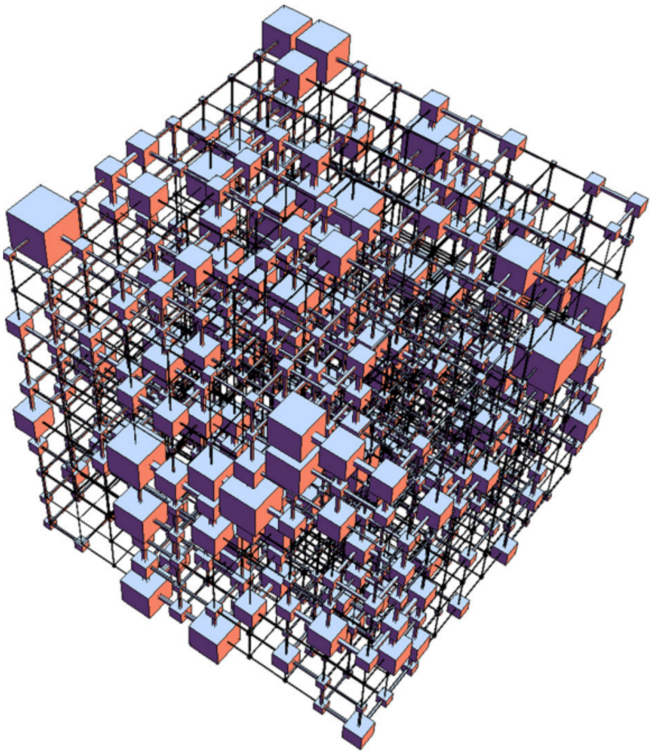

Figure 3.4: Example of a network in 3-D. Obtained from[41]

3.2.1 Generation of the pore network

The previous section described the development over time of pore network models, how they depict the reality and some of the rules necessary to provide a good representation of porous media.

In this section, it is explained the generation of porous network of this thesis.

A discrete reconstruction method is used and a stochastic algorithm, a Monte Carlo, generates the pore network from input data. As it was seen in Figure 3.1, pores are composed of cylindrical pores and spherical volumeless nodes that overlaps. A network can even be generated in the three dimensions as will be seen in the thesis. In this essay many typologies will be presented: 1 dimension pore, which reproduces a tube, 2-D and 3-D.

The lattice is created by establishing a priori the distance between adjacent nodes, which also gives the length of the pores. Moreover, the number of nodes wanted in each dimension is also previously chosen as well as the PEP, pore existence probability, which gives the probability that each node is linked to the maximum number of pores possible in its position.

One of the main features is, in fact, the connectivity of the network. This number represents how many pores are connected to each node.

Indeed, in a regular square lattice, as case a in Figure 3.3, only pore bodies between two nodes can be accepted. In a 1-D the maximum connectivity is 2, in a 2-D is 4 and in a 3-D, 6 pores are connected like in Figure 3.6. In other regular lattices, the connectivity may differ and be higher for the nodes like in a case of triangular 2-D pore network as case d in Figure 3.3, where connectivity can have a value of 6. In irregular lattices where the spacing and the presence of pores between nodes may vary, the connectivity could change substantially, from the minimum of 0, which means that the node is not connected, to a maximum of 18.[18]

In addition to this and to provide more heterogeneity to the structure and to its topology, it is even possible to consider various levels of pores in the lattice, obtaining pores of disparate diameters according to the inputs given.

The last feature that can be implemented in order to obtain a higher unpredictability is called Grid distortion. The initial grid can be slightly reshaped by a factor that reallocates the node. This correction modifies the length of the pores. It is possible to decide the dimension of the distortion, shown in Figure 3.5 a, where an orange square represents the possible area of movement of the node. In 3.5 case b it is shown a node that has already been moved from the original position and in the third case, c, it is shown the impact on pores of the new node position and their new shapes. To clarify more how this works:

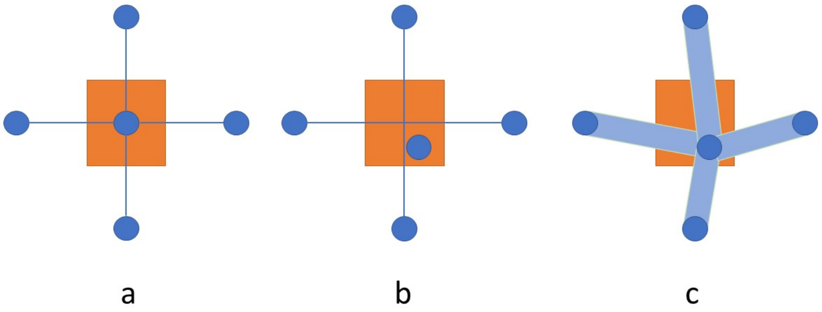

Figure 3.5: Grid distortion in the lattice

3.2.2 Pore network model

The algorithm to obtain the network works by selecting the node, then uses the pore existence probability given as an input and evaluates the possibility to either create or not a connection between the nodes. If the connection is possible there is the generation of a pore.

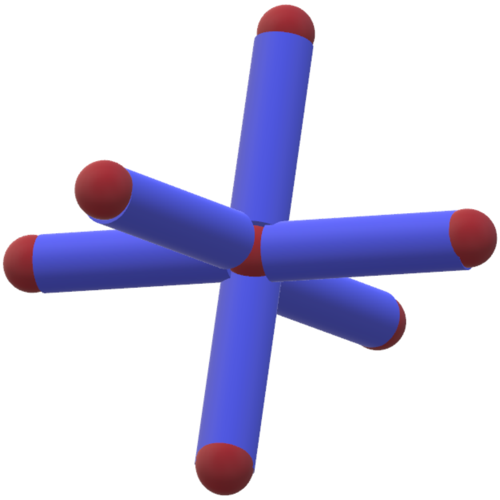

Figure 3.6: Pore network connections in 3 Dimensions.

The reproduction of the alumina pore network is shown in Figure: 3.7. In this magnified picture, it is possible to see the pores in a lattice. As an input it was chosen a regular lattice but modified with a gaussian distribution to obtain different diameters to try to reproduce adequately the multiple pore dimensions of the real γ-alumina.

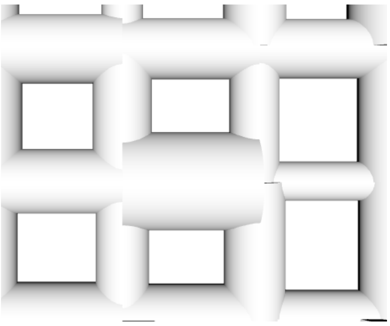

Figure 3.7: Zoom of the pore grid from the simulation.

In order to give an idea of the influence of the various parameters previously described, an overview of the typologies of the grid is displayed. The pictures below help to visualize instantaneously the role of the parameters and the influence they have on the lattices. However, a tangible approach is needed in the diffusion simulations. Numerical outputs of this first simulation are a necessity.

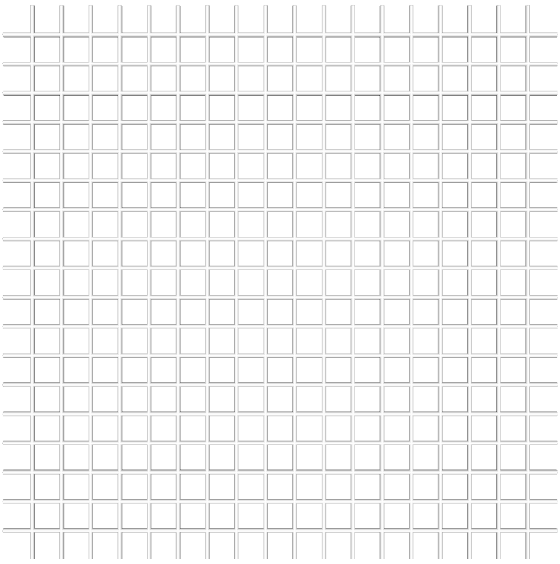

Figure 3.8: Pore network with a regular lattice and constant diameters.

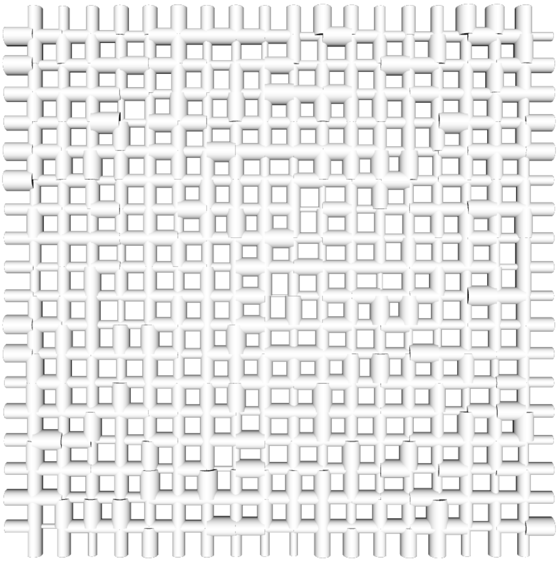

Figure 3.9: Pore network with a regular lattice and gaussian distribution in the pore diameters.

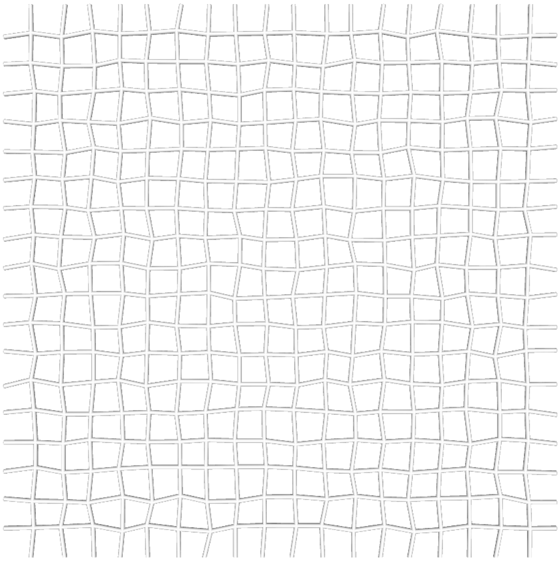

Figure 3.10: Pore network with a regular lattice modified with a grid distortion.

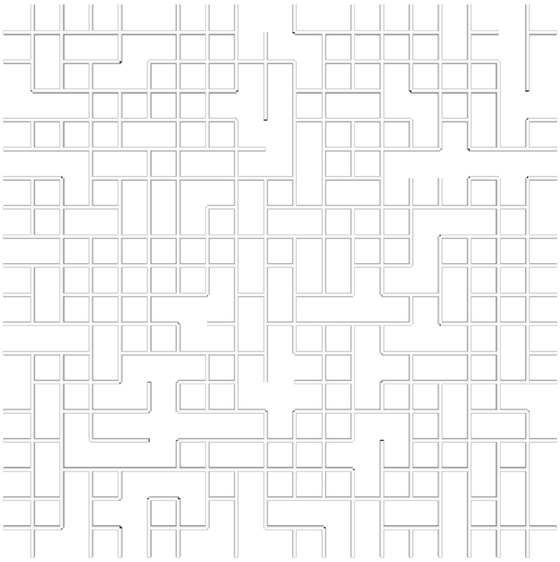

Figure 3.11: Pore network with a regular lattice and a pore existence probability of 0.75. Nodes have a mean connectivity of 75% of what they would have in a complete regular lattice.

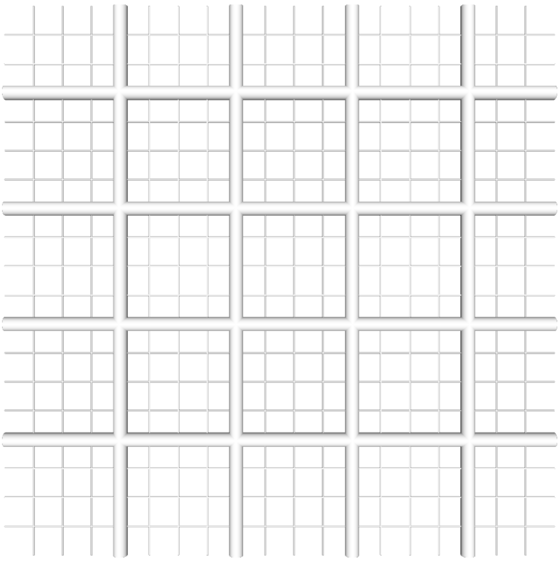

Figure 3.12: Pore network with a regular lattice and 2 levels of pore sizes.

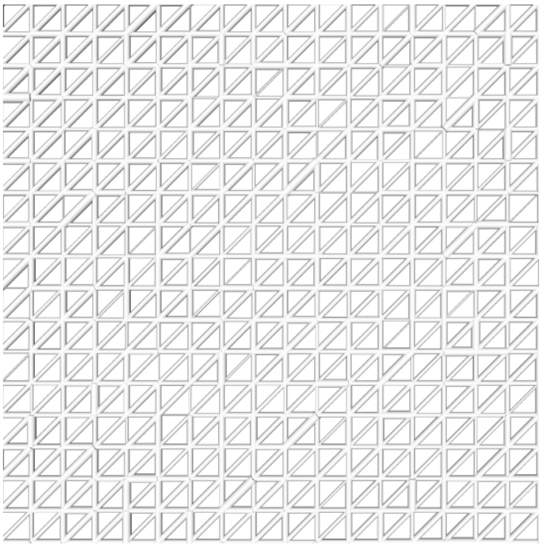

Figure 3.13: Pore network with a triangular lattice and Pore size distribution.

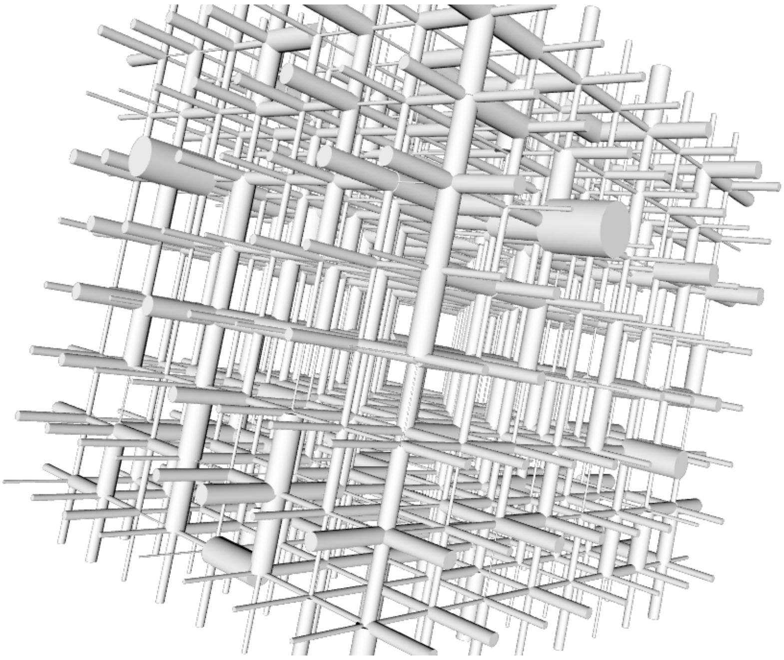

Figure 3.14: 3D Pore network with gaussian pore size distribution

Firstly, as it is evident the total number of nodes is the product of the nodes, given as input, of each of the three dimensions. Each pore has a surface that can be easily calculated according to the fact that the pore are chosen cylindrical with a known length L (distance between nodes).

$$S_i = 2\pi r_i L \tag{3.1}$$

Volume likewise can be calculated with the common formula:

$$V_i = \pi r_i^2 L \tag{3.2}$$

The first file obtained gives a report of the connections of each node and the direction of each connection. In table 3.1 are given the results of a regular network 2-D of 15x15.

Table 3.1: Connectivity matrix

Node	Z	Connectivity Matrix			
1	0	0	0	0	0
2	1	1	0	0	0
3	1	2	0	0	0
4	1	3	0	0	0
5	1	4	0	0	0
6	1	5	0	0	0
15	0	0	0	0	0
16	1	14	0	0	0
17	4	-1	-14	15	16
18	4	-2	-15	17	18
29	4	-13	-37	39	40
30	1	-39	0	0	0
31	1	41	0	0	0
32	4	-16	-41	42	43
223	1	-362	0	0	0
224	1	-364	0	0	0
225	0	0	0	0	0

The table 3.1 is just a compressed version of the total output file but can be used to highlight the most important features: The first column gives the node that it refers to, the second number, called Z, gives the total connectivity of the node, that is the number of nodes connected to that node. The last four numbers refer to the name of the pore created by the connection between the two nodes and the sign is given by the direction of the connection as it is visible in Figure 3.15.

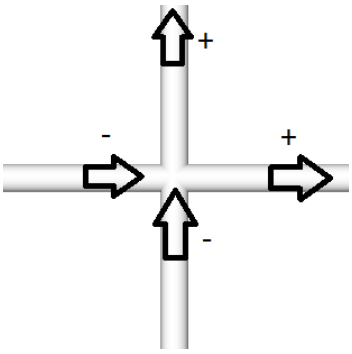

Figure 3.15: Sign of the connections

As it is visible in Figure 3.16, Node 1 (located in left down corner) is not connected to any node, therefore, its connectivity is equal to 0. Node 1 (right to node 0) is connected only to node 17. Node 17 has a Z of 4 because is fully connected etc.

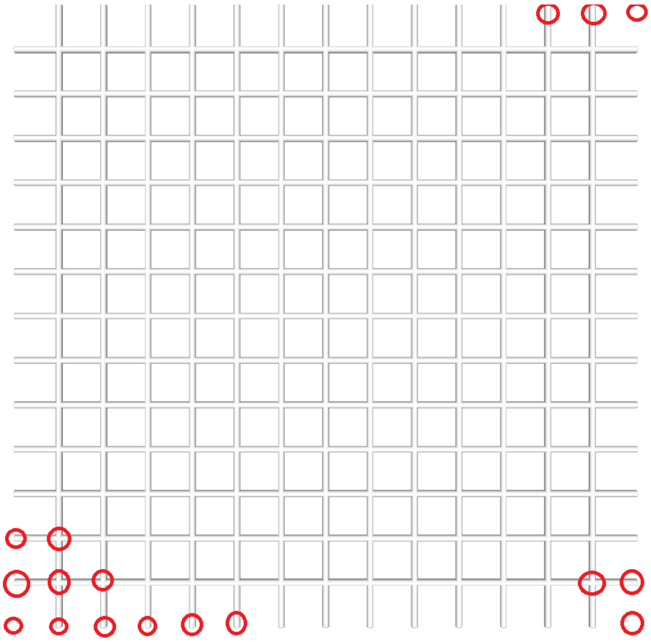

Figure 3.16: Pore network with a regular lattice related to the table 3.1 where the nodes are highlighted

An output file gives the coordinate of each node in the space (x,y,z), feature important for the PFG analysis.
An output file, called Global Parameters, gives the average parameters needed as input for the diffusion like:

- Maximum number of nodes
- Nodes connected to at least a pore
- Maximum number of pores
- Number of effective pores
- Maximum connectivity
- Average connectivity
- Pore length (maximum, minimum and average)
- Pore diameter (maximum, minimum and average)

An output file, correlates each pore to its connection nodes and gives each length and diameter. For example in figure 3.16, pore 1 connects Node 2 and Node 17. In addition to this, in that regular lattice length and diameters are constants.
The last output file used gives a number to understand if the node is connected to other nodes. In a regular lattice this file is unnecessary. However, in highly irregular lattices, with PEP<1 it gives important information as some internal nodes may be totally isolated from the other nodes.

Chapter 4

Simulation

4.1 Diffusion

In order to simulate diffusion inside the network the classical laws of Fick were used. Fick's law are constitutive laws to describe the variation of concentration in space. The first law is:

$$\vec{J} = -D\vec{\nabla}\Phi \tag{4.1}$$

and the second that regards the temporal aspect is:

$$\frac{\partial \Phi_i}{\partial t} = -\nabla \cdot J_\phi \tag{4.2}$$

The simulator solves simultaneously a system of parabolic partial differential equations from Fick's second law employing orthogonal collocations. Each pore will be subjected to an equilibrium between the species and the position of the pore influences the boundary conditions adopted. Internal nodes of the lattice have a Dirichlet condition, so that the mass flow entering and leaving from the node are identical, while in order to simplify the calculations, external nodes present a constant concentration.

Table 4.1: Diffusion boundary conditions

Node Type	Boundary Condition
Internal	$\sum_{i=1}^{N_{tot}} J_i S_i = 0$
External	$C_i = C_{ex}$

In order to understand more how the pores are connected and how boundary conditions of diffusion are implemented, it is presented a representation in Figure 4.1. Grey rectangles are a 2D representation of pore bodies with a known length

$L_{p,i}$, the blue circle is a representation of the common node that overlaps between all the pores and where mass transfer can be instantaneous. Moreover, the orange circles represent the spatial discretization called orthogonal collocations.
Collocation is the zone of the pore where diffusion is controlled, because as an output it gives the molar fraction of the species. In the figure, these circles overlaps because the collocation is also common to each pore and consequently each pore in that collocation has to have the same concentration (molar fraction) of each specie. Each pore of the network was spatially discretized using an orthogonal method created by Villadsen and Stewart.[42] The resolution of the differential equations was done through an adaptive time integration called DASPK routine created by Van Keken.[43] Collocations allow to understand how the molecules are diffusing by giving a numerical value of the molar fraction.

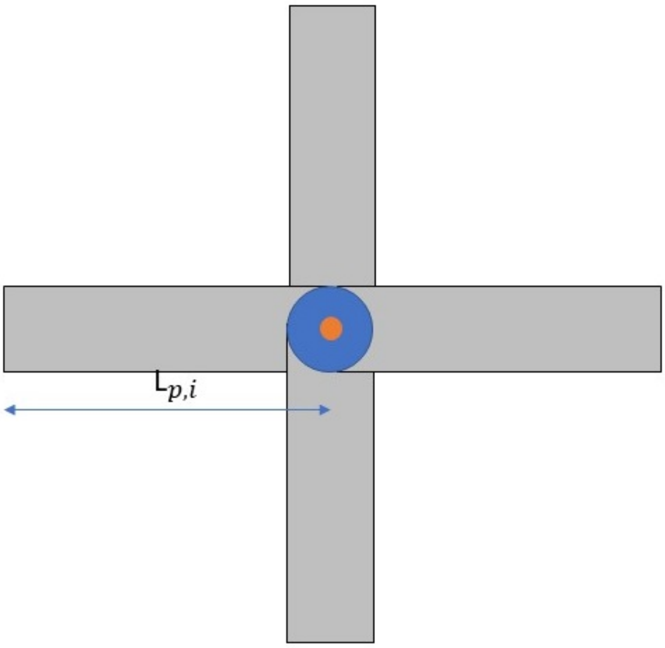

Figure 4.1: 2D representation of the common collocation in pores

In the simulations, the pores were splitted in three collocations. One collocation is present in each face and one at the center of the pore as visible in Figure 4.2. Because of this discretization there are three partial differential equations that have to be solved simultaneously for each pore.
In a mathematical point of view, considering two connected pores in the x-axis, as visible in Figure 4.3, and calling them i and j, the molar fractions in the common

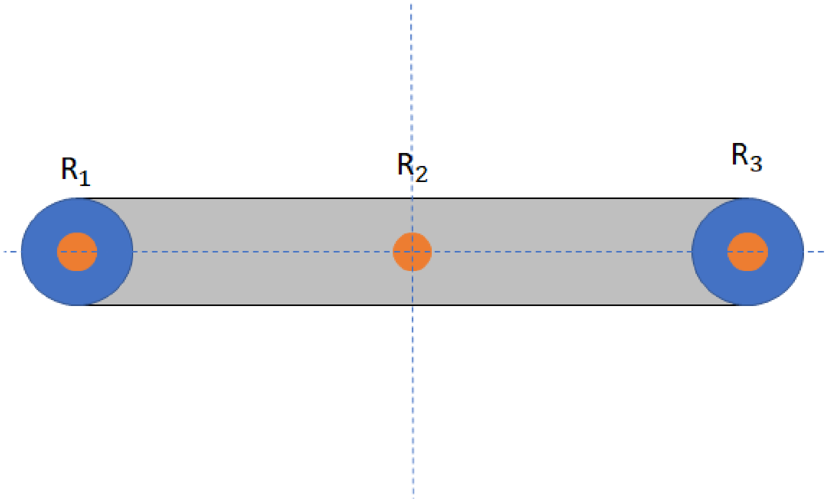

Figure 4.2: Collocation roots in a pore

collocations are the same:

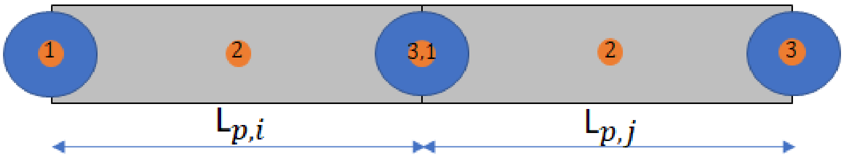

Figure 4.3: Representation of the collocations in connected pores

$$X_{a,i,3} - X_{a,j,1} = 0 \tag{4.3}$$

As was introduced in the second chapter, Fickian diffusion in a porous network is not free but restrained and is therefore called restricted diffusion. The diffusion coefficient, called apparent or efficient, associated to this diffusion will be lower than the ideal diffusion coefficient. The molecules after the diffusion will have a gaussian distribution and the MSD, Mean Squared Displacement, will be related to the Diffusion coefficient as seen in formula 2.12.

Molecules diffusing are considered as an ensemble in a Fickian environment. The use of a totally brownian motion strategy, like a lagrangian for each molecule, is a CPU-intensive strategy that is not available for a common single data processing system. The discrete simulation that should be comparable to a random walker (in this case numerous molecules in brownian motion) is in fact substituted by a fickian simulation.

As a confirmation, pores in the simulation are chosen in the meso range, where Fickian diffusion can be seen as continuous.

4.1.1 Strategy: Diffusion in the network

In order to model the auto-diffusion, an artifice has been used. All the collocations inside the pore network are initialized with the same molecules in order to guarantee the same concentration and physical properties homogeneously in the network. However, only in the pores in charge of having the molecules that have to diffuse, the molecules will be renamed, so that after the diffusion has happened, it is possible to check the molar fraction of this specie in each of the collocations of the network.
The first thing to do is to chose the initial pore where diffusion can start and initialize it with the labelled molecules. This pore from this moment will be called *tracer pore* with molar fraction X_{tracer} .

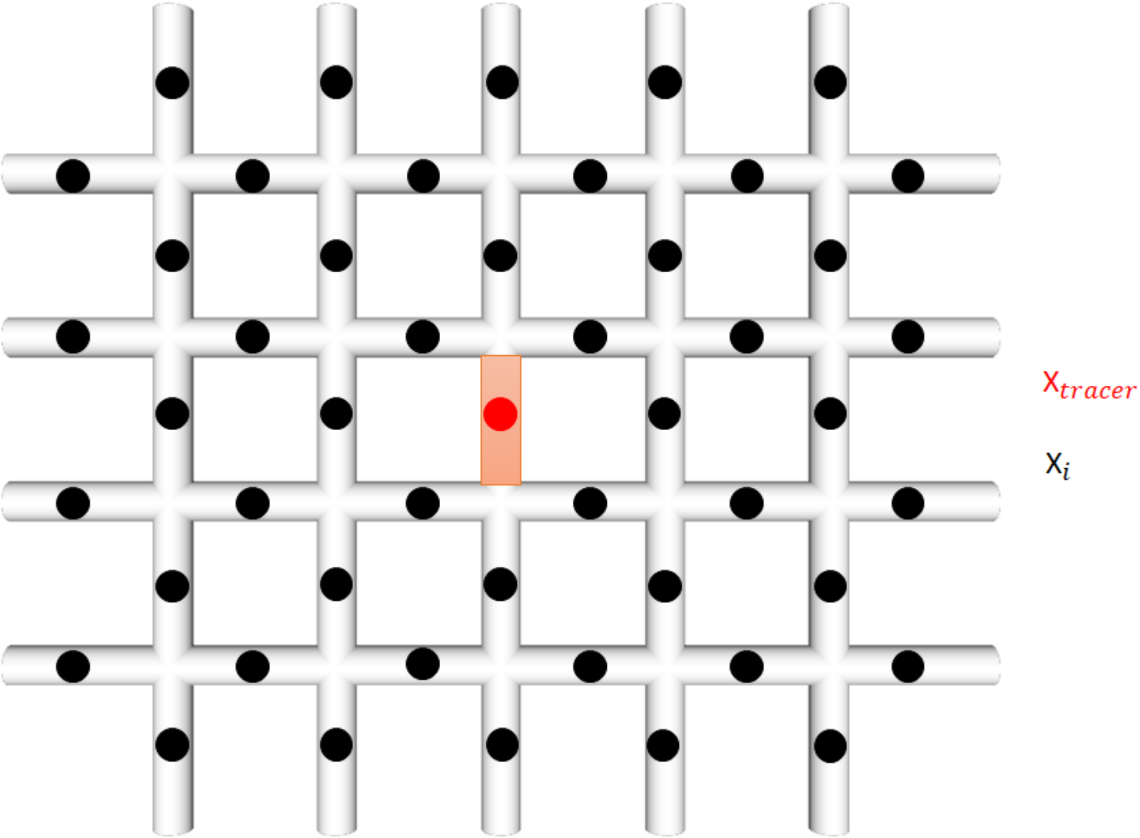

Figure 4.4: Tracer pore inside the pore network, example from[18]

As will be explained in the next section, the loss of matter has to be avoided at all costs in order to obtain the real signal in the PFG-NMR characterization where all particles need to be taken into account.
In order to prevent the leak, the tracer pore is chosen in a restricted zone of the

network that is called *active zone*.

To calculate this zone, it is necessary to understand how far a particle could travel in the network from the tracer pore. This length is calculated knowing the diffusion coefficient of the specie, D, and the diffusion time adopted, Δ through the Einstein-Smoluchowsky equation that parametrizes a Brownian particle's trajectory, and therefore unrestricted diffusion, in Formula 4.4.[44]

$$L_d^2 = 2D\Delta \tag{4.4}$$

The zone of the possible tracer pores has to be distant from the borders of the network of this length L_d.

The dimensions of the network are known a priori because of the choice of the number of nodes in each direction and the length of the pores (even with grid distortion the total length of the edge of the network is basically the same). The total length of the network is called L_n.

The dimension of the active zone can be deducted from the other lengths.

The active zone used in the simulations in the 2D simulation is squared and in 3D is a cube. The motivation lies on the fact that by using a squared active zone, it is possible to consider each pore inside in its totality without having to eliminate any of the collocations that would create problems in the case of initialization of a tracer pore on the border of the zone, like in the case of a circular active zone. In addition to this, it is evident that in Figure 4.6 there are two different lengths L_{max} and L_{min}. This would create heterogeneity in the distance to the borders of the network. This problem is avoided by choosing a squared active zone.

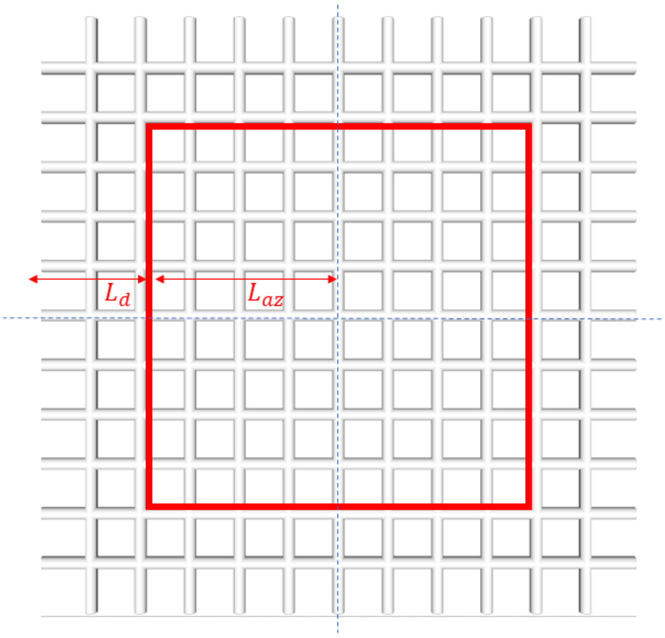

Figure 4.5: Squared active zone with L_d and L_{az}

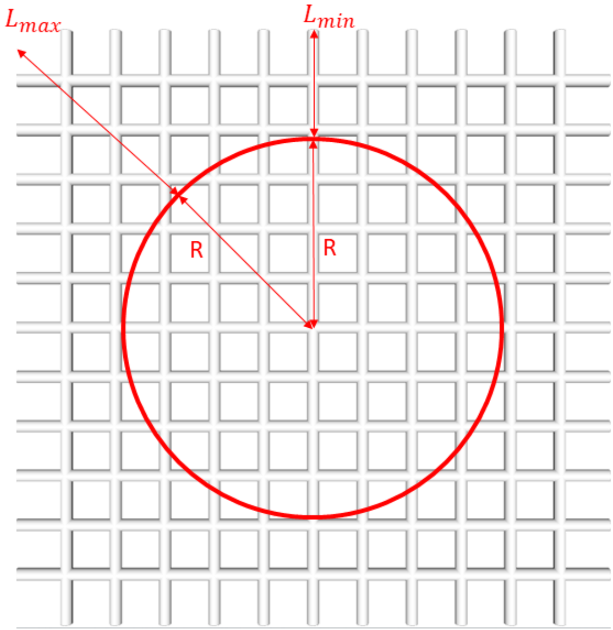

Figure 4.6: Circular active zone and the difference between lengths

In the chosen case of a squared active zone, by dividing the L_D found through Einstein-Smoluchowsky equation by the length of an average pore, it is obtained the number of pores that have to be distanced from the borders and the dimension of the active zone are found by:

$$L_{az} = L_n - 2L_D \tag{4.5}$$

In a realistic perspective, active zone is a similitude to the real experiment. Active zone represent indeed the zone where PFG-NMR is measured inside the alumina pellet. In that case, the sample is big enough so the main contribution to the signal comes from the molecules that remain inside of the sample during the measure. As a comparison it is also needed in the numerical simulation an hypothesis that can have the same value.

The first strategy adopted to characterize the network was to analyse the area of diffusion and considering the active zone as a percentage of the total area of the pore network.

This approach was unsuccessful, in fact in order to avoid the loss of particles and obtain a proper size of the active zone of 90% of the area of the network, it would be necessary to increase the size of the network. The problem is that the number of pores increases quadratically, in fact the number of pores in a regular squared pore network as a value of:

$$N_{totpores} = 2(N_x - 1)(N_x - 2) \tag{4.6}$$

This methodology was therefore avoided. The second method saw the use of a constant active zone of an area of 80x80 nodes. This area was in fact chosen because previous results in similar numerical simulation of alumina This area was chosen because it correspond to the minimum pore network size that should be used to obtain representative textural and transport properties (micrometric scale) according to similar numerical simulations.[18] Because of this, the pore network that will be used in regular lattices is calculated as equation 4.5 with a constant L_{az} and L_D that depends on the diffusion time.

However, even if this strategy was less CPU-intensive, an additional help was necessary in any case, so for some calculations it was used the Academic computing system HPC-Polito.[45]

4.2 Hypothesis

The PFG-NMR analysis is the step consequent to the diffusion. The characterization involves many hypothesis and simplification due to the many passages required.
Hypothesis for the PFG analysis are needed:[18]

- Spin diffusion is the only simulation model used, spin dynamics (Bloch equations) is not considered.[46]
- Magnetic field inhomogenities are neglected.
- It is not modeled the full pulse gradient sequence.
- The magnetic moment is measured only in the transversal plane.
- The interactions of molecules are neglected, so that local magnetic fields are not present.
- Loss of molecules from the porous network is not present and the signal does not decrease because of it.

In addition to this, a simplification that it has been already seen is the compatibility of PFG-NMR with brownian motion. Brownian motion considers each particle, but in a numerical simulation it is not possible to take into account every interaction and it is necessary to evaluate ensembles and concentration of species. In a way, the effect of the concentration profile should not modify the signal obtained by the PFG-NMR sequence. The signal in fact, would decrease linearly in a free diffusion, while in a restricted diffusion the signal is modified because of the topology of the network.
To understand more the assumptions done, it is possible to exploit the hypothesis used in real experiments, where the magnetic field created by the coil is constant in the sample, Figure 4.8 and field inhomogeneities are neglected.[33]

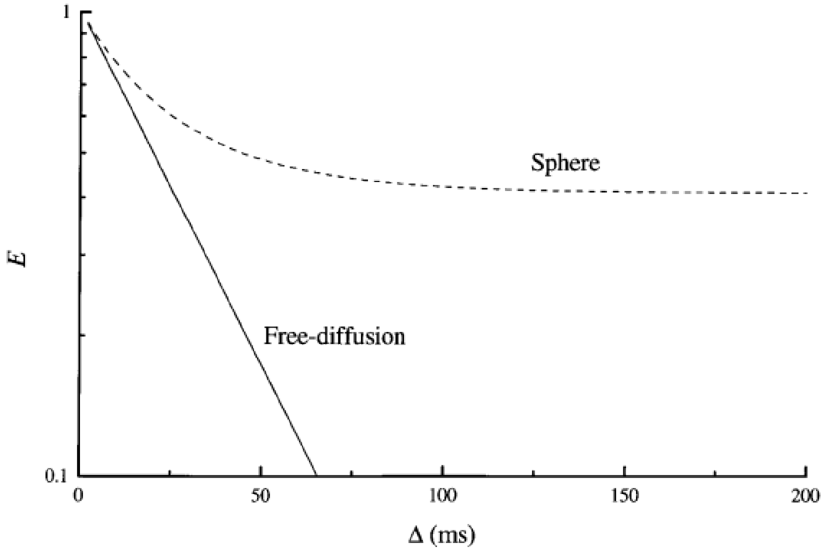

Figure 4.7: Simulated echo attenuation in the case of free and restricted diffusion in a sphere with GPD approximation against time Δ. Obtained from[31]

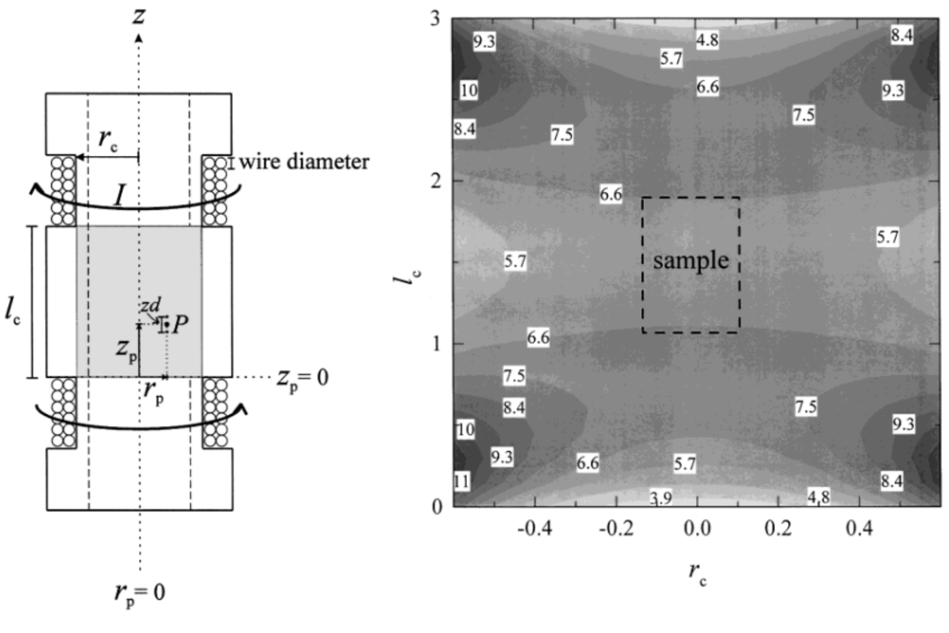

Figure 4.8: Schematic description of the coil of a PFG-NMR machine and constant gradient in the sample. Obtained from[33]

4.3 Algorithm

The previous sections of this chapter and the previous chapters introduced the creation of the pore network and the two main blocks of the thesis. Moreover, a well defined sequence is vital to understand and reproduce the results obtained in the simulations.
As it is visible in Figure 4.9, to represent the real tortuosity of the pore network, tracer pores have to be chosen randomly. It is also necessary to check that each tracer pore was not already taken in precedent simulations. In fact, if it was previously chosen, this would have an impact on the calculated tortuosity of the system losing the potentiality to represent the pore network. Numerous and differently positioned tracer pores are therefore needed. The results of the signal obtained are subsequently averaged, diffusion coefficient extrapolated and the tortuosity, through equation 2.16, is obtained.

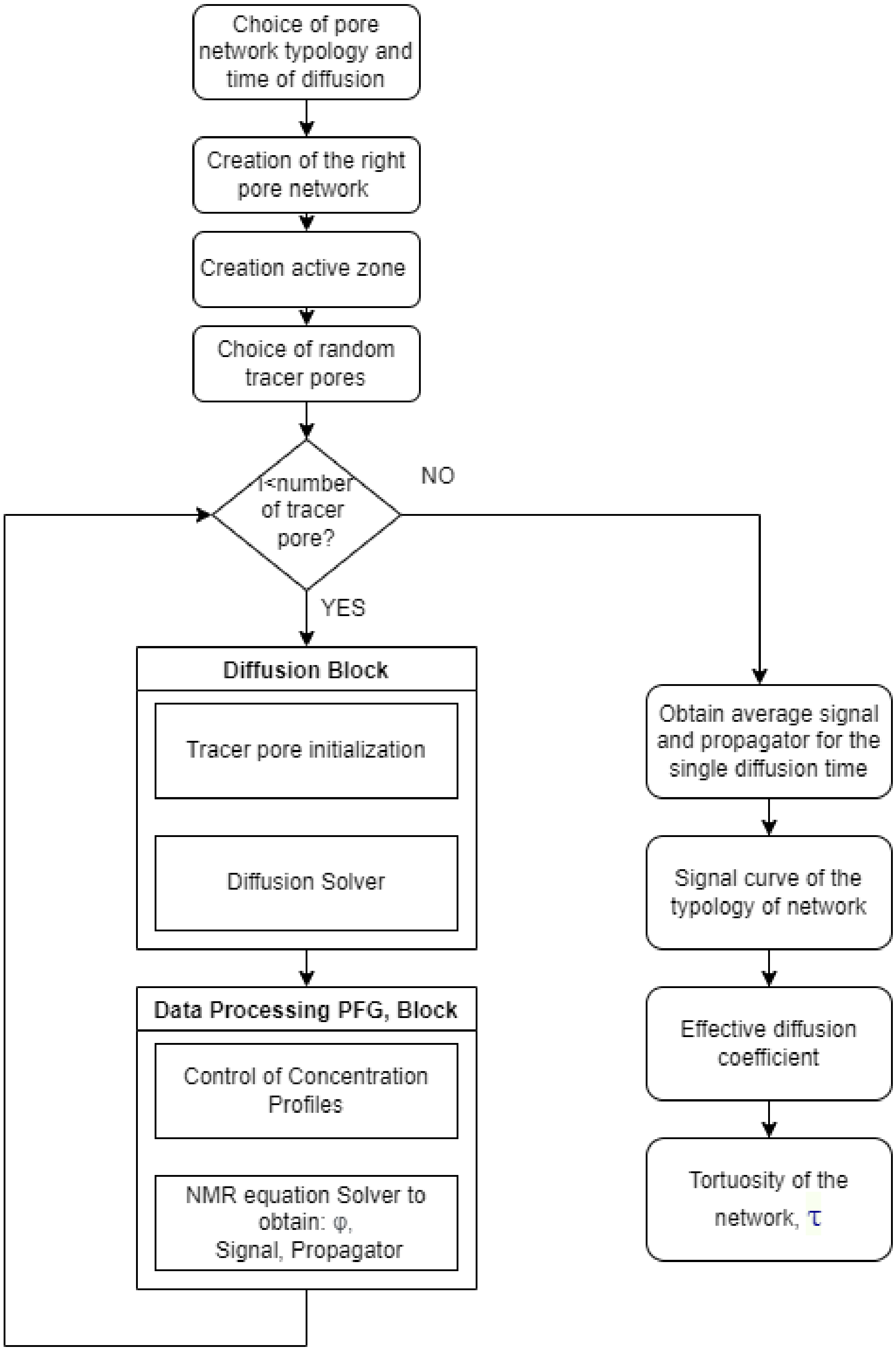

Figure 4.9: Algorithm of the simulation, i is the counter of tracer pores

4.4 Simulation of PFG-NMR

4.4.1 Origin of experimental data

In order to approach the PFG-NMR technique and to have a realistic comparison, an experimental background was needed. The data necessary to implement a good approximation and validate the results were provided by the thesis of Aleksandra Glowska.[36]

The diffusion of the organic liquid called Acetonitrile, CH_3CN, inside the porous network has been characterized in the laboratory by Glowska through a PFG-NMR technique.

γ-alumina was analysed using an organic liquid substance, Acetonitrile, CH_3CN. Acetonitrile has a characteristic γ, gyromagnetic ratio, of 2,67 x 10^8 $(\frac{rad}{sT})$, a molar mass of 41,053 $(\frac{g}{mol})$, and a density at 25°C of 0,786 $(\frac{g}{cm^3})$.

In addition to this, in her work she found an unrestricted self-diffusion coefficient D of 1,897 x 10^{-9} $(\frac{m^2}{s})$. This value will be used as a reference in the numerical simulations.

The main difference between the work done in her thesis and in the following sections is that Glowska using the PFG-NMR apparatus, modified the gradient intensity as a way to modulate the signal. In this work, however, the gradient intensity is fixed and the diffusion time is varied. The diffusion times used are the same to the times used by Glowska.

Table 4.2: Diffusion times

Diffusion time Δ (ms)
5
10
20
50
100
140
200

4.4.2 Methodology

Firstly, it is needed to understand how to express the gradient and the typology of the gradient used in the PFG-NMR analysis formulas.

The profile of the magnetic field is considered to be linear and dependent on the position of the particle with respect to the position on the x-axis on the network. In the experimental case in Figure 4.8, the maximum of the gradient is at the center of the sample and the model tries to replicate this phenomenon. In the simulation the intensity of the magnetic field is considered as linear[47] and calculated through:

$$B(x) = -mx \tag{4.7}$$

Where m is the positive gradient and x the position in the network of the collocation where the concentration is controlled. Although being confirmed in articles,

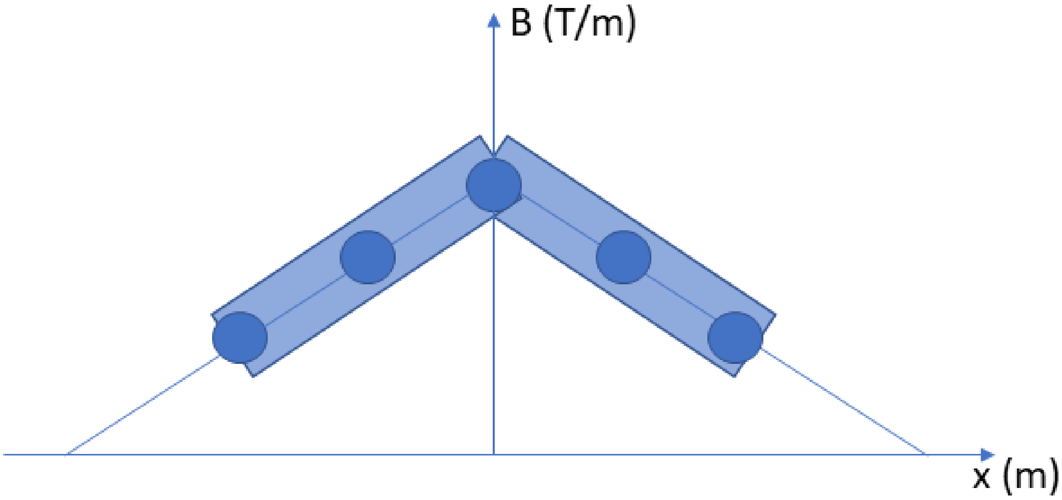

Figure 4.10: Idealization of the linear profile gradient along the pores in the network

the linearity can be thought as a simplification. In fact, another representation is that the gradient may even be quadratic, however since the scale of the network is small, it is possible to simulate the gradient linearly. This choice is supported by literature (Price) in[31] where during spin excitation a first order magnetic field with a 90° pulse is applied.
The first equations to obtain phase shift were seen in equation 2.6. In that case ϕ is considered a temporal variable. It is used at the end of the diffusion and the contemporary pulse sequence.
All the integrals seen in the equations of this section were initially analysed with two methods: trapezoidal rule and a quadrature formula. Because of the composition of the collocations and the initialization of the tracer pores, by analysing the results of the integrals it became evident that the best choice was the quadrature with the use of roots and weights that are given as an output value by the program. Trapezoidal integration in fact gave results not compatible with the results that were expected.

To further approach the methodology, it is vital to guarantee that molecules remain inside the pore network but at a distance that can be detected as a signal with the equations used.

The initial diffusion coefficient did not assure that molecules did not escape from the network. The use of this real coefficient means that it is needed to model the auto-diffusion in huge pore networks. The CPU and the time needed to work with these networks are above our means because it would take days or even weeks of calculations.

In order to solve this problem and because the goal is not to measure the "real" effective coefficient but to obtain the tortuosity of the pore network, it is possible to simplify the calculations by decreasing by orders of magnitude the diffusion coefficient used.

Doing so, it is possible to decrease the dimension of the networks and therefore reduce significantly the calculation time.

The minimum dimension of the network was calculated by taking into considerations precedent numerical simulations by nitrogen porosimetry[18] that well represented the statistical topological characteristics of the network. Once this dimension was addressed, it was possible to chose the diffusion coefficient, proportional to the initial one, with the aim to guarantee that the mass balance inside the network was constant.

The mass balance of the pores of a network 80x80 found by diffusion at a time of t= 0,005 s, which is the lowest among the diffusion time, gives a quite total loss at 10^{-9}, a 12% at 10^{-11} and then at 10^{-13} the loss is practically nil.

The experimental value is in fact a classical value found for liquids. On the other hand, D=1,897x$10^{-13}\frac{m^2}{s}$ is four order of magnitude lower. The deviation from ideality is so high that the mass diffusion coefficient is in a range classical to gas diffusion in solid lattices.

However, it can be seen as an initial numerical simulation that can be scaled up with a higher capacity CPU.

Another possibility approached in order to avoid the loss of particles was to change the boundary conditions of the external nodes creating a sort of bouncing impassable boundary rather than imposing a constant concentration. However, the use of this strategy limits the possibility to exploit MSD as the molecules can not move freely and therefore restricting the calculations of the effective diffusion coefficient and the tortuosity. For this reason, although these impenetrable conditions could allow to use higher diffusion coefficients, the proper choice was to avoid them and use a lower diffusion coefficient.

Propagator is used to visualize the dispersion of the particles from the original tracer pore. Using the gaussian hypothesis and imagining the propagator as a

product between a line with linear coefficient of 1 that represents the distance from the tracer pore and the molar concentration found, it would be obtained a gaussian because in the short distances the mass would be high. In fact, although the distance is short the concentration is at the highest, at a medium distance we would obtain the higher value from the product because it would have both the contributes and as the distance from the origin (tracer pore) increases the mass would be so low to be equal to 0.
Regarding the propagator, it can be calculated as the average of the displacements in the network.

$$d_i = \frac{\int_0^{P_{i_L}} X_m(x)\sqrt{(x-x_0)^2+(y-y_0)^2}dx}{\int_0^{P_{i_L}} X_m(x)dx} \tag{4.8}$$

An example of the propagator profile obtained in a network is visible in Figure 4.11

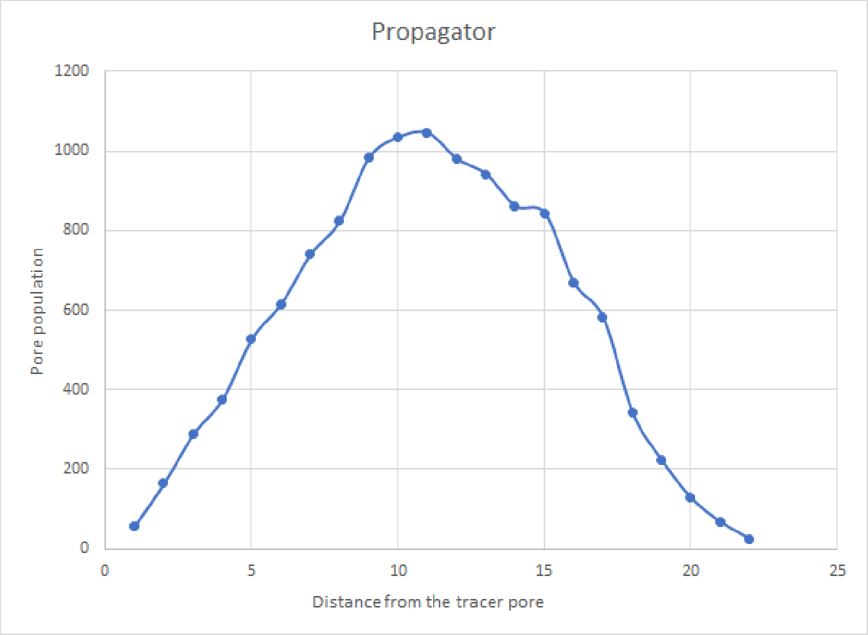

Figure 4.11: Propagator profile in a 80x80 network (discretized on 2 pores)

The evaluation of the signal when the concentration is near 0 is practically impossible because it means that the molecules had had a high time of diffusion and the mass profile will be basically constant in the range of collocations near the one in examination. In this case the profile is not anymore similar to a bell. In these analyses, signal is measured through equations while in experimental setup the calibration is done by the machine and losses of signals due to this low local values are already accounted by the system.

The use of the gaussian hypothesis can be improved by modifying the initialization of the original tracer pore. In fact, in this case it is useless to use a constant concentration in each pore but it is preferable to take advantage of the gaussian mass distribution with a magnetic field that is linear. Because of this new strategy, from now on a gaussian profile has been employed to improve, in the case of low times of diffusion, the concentration profile. The initialization has been developed by supposing to divide the gaussian curve in 5 points where the borders are 0, the new strategy initializes at 1 the center collocation, the boundary collocations are equal to 0,32 while avoiding to use the 0 values and creating a sort of gaussian bell.

The development of the methodology determined a value of magnetic gradient. The gradient m, equation 4.7, used is equal to 0,086 $(\frac{T}{m})$ and calculated supposing the same gradient percentage variation in the simulated pore network as in the experiments of Glowska[36] between the highest and lowest gradient value of the machine.

In the simulations, concentration is traced at nano and mesoscale. Due to this, gradient intensity has to be modulated on these orders of magnitude. Therefore it was needed to upgrade it into a value that is in the order of the most powerful machines used into PFG-NMR with a value of 86, three orders of magnitude higher $(\frac{T}{m})$ than the previous approximation. This value is higher than standard and PFG-NMR machines present in the market, but in the same order of magnitude. However, this is an analogy to the dimension of the network with regards to the real pellet. Indeed, the zone of the pore network that is analysed is in the orders of some μm, while in experimental pellets are in the order of mm, so the variation of orders of magnitude is similar to the variation of the intensity of the gradient. The displacement of the phase is calculated from equation 2.7 to quantify the cumulative phase shift for the system, in fact B1 radiofrequency pulse allows to cumulate the phase. If the displacement during the pulse δ is neglected:

$$\phi(2\tau) = \left\{ \gamma g x_0 \int_{t_1}^{t_1+\delta} dt \right\} - \left\{ \gamma g x_f \int_{t_1+\Delta}^{t_1+\delta+\Delta} dt' \right\} = \gamma g \delta (x_0 - x_f) \tag{4.9}$$

Where x_0 and x_f represent the initial and final coordinate on x of the molecule. In this case the pore is considered completely as the value of molar fraction given by the central collocation and the distance is measured from the center of the original tracer pore to the final position. If the pores are detected with a tracer molar fraction higher than 0, they are considered in the signal measurement:

$$E_i = \sum_{i=1}^{Np} \left\{ cos(\phi_i(t)) * \frac{S_i * L_i * \int_0^{P_{i,L}} X_i}{S_0 * L_0 * \int_0^{P_{0,L}} X_0} \right\} \tag{4.10}$$

$$\sigma = \sqrt{\frac{1}{N_{tracerpores}} \sum_{i=1}^{N_{tracerpores}} (E_i - E_{av})^2} \tag{4.11}$$

The number of tracer pores is calculated by checking that the standard deviation of the signal values has to be lower than 5%.

$$E_{\Delta} = \frac{1}{N_{tot}} \sum_{j=1}^{Ntot} E_j \tag{4.12}$$

Two conditions need to be verified in this methodology, $\delta \ll \Delta$ and $\frac{1}{q} \gg L_{pore}$ where q represents $q = \gamma g \delta$ as.[48] The minimum time is 5 ms which is lower than the δ that will be found and $\frac{1}{q}$ is in the order of magnitude of 10^{-6} while L_{pores} is 60 nm.

In the methodology, it is needed to assess the value of δ. The method used is a calibration by a theoretical hypothesis that in a unique pore (like a long tube where no mass has the possibility to leave it) the efficient diffusion coefficient obtained is equal to the ideal one because the tortuosity can be thought as equal to 1, like in a free diffusion.

By a recursive trying function between an initial delta and the obtained signal and vice versa, it is obtained a δ of 1x10^{-5} for the solo pore. By using the same methodology but changing the standard pore to a regular lattice pore network the same delta is obtained although it has been proven that even at higher delta in the same magnitude the tortuosity found is equally valid. The same idea can be replicated even in a 3D ideal pore network.

The signal attenuation allows to obtain the effective diffusion coefficient, D_{eff} as the linear coefficient of the plotting line. The constant term represents on the other hand the slight variation of the idealized line and helps to understand the validity of the model. On the x-axis, the value used derives from equations 2.19 and 2.21.

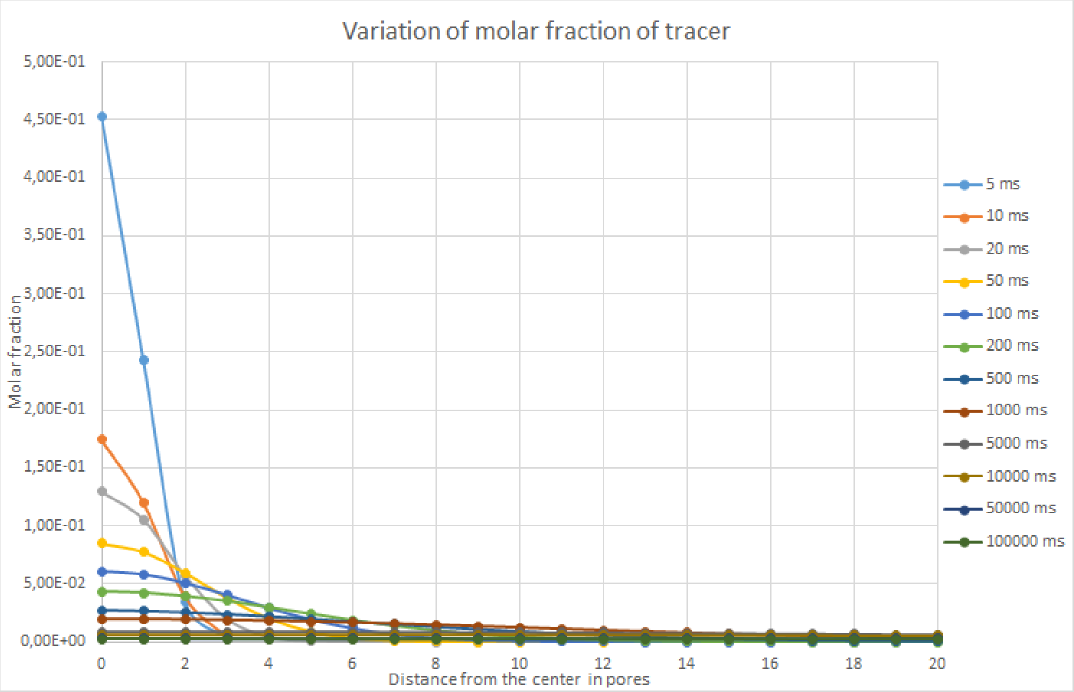

Figure 4.12: Variation of the concentration of tracer in the single calibration pore

The Figure 4.12 represents the molar fraction obtained in the single calibration pore at different diffusion time, it is possible to immediately visualize the effect of time on the dispersion of the particles.

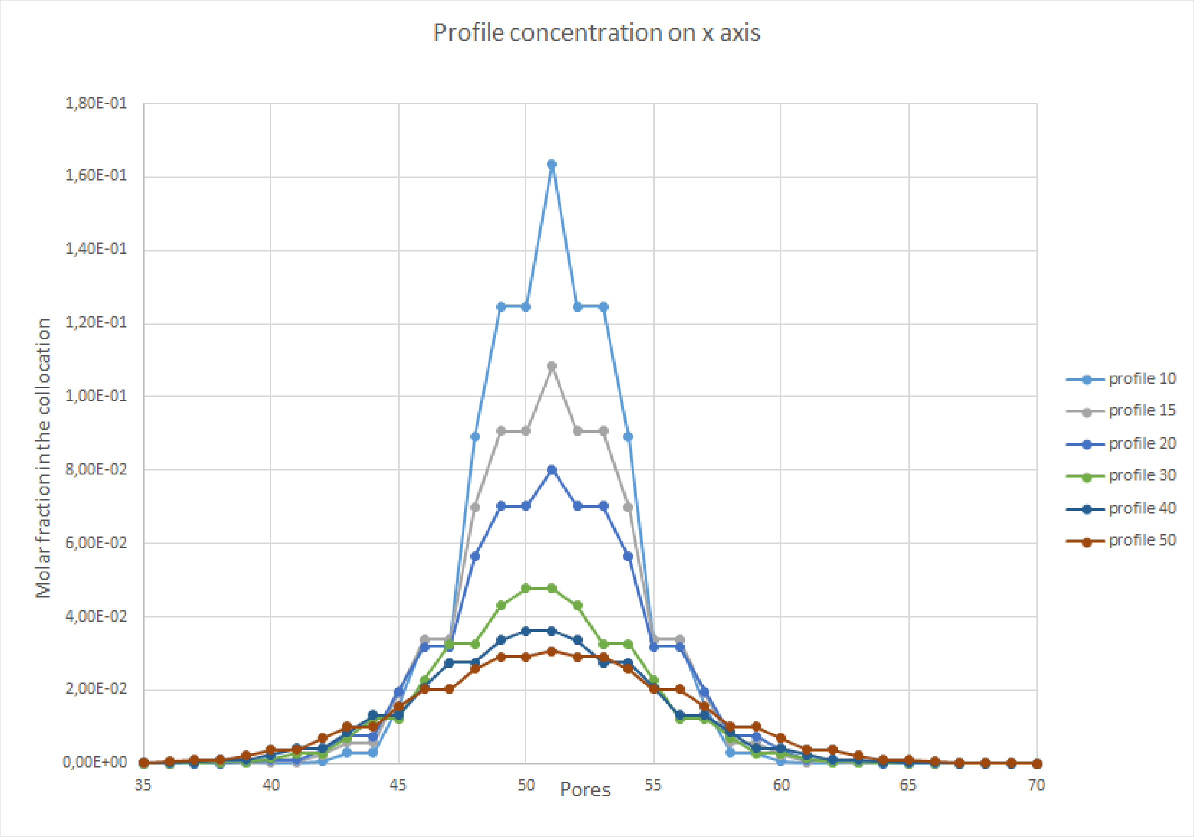

Figure 4.13: Variation of the concentration of tracer in the x direction in a regular pore network, τ=1

Figure 4.13 is a visual representation of the molar fraction of the various pores' collocations starting from the same tracer pore at different diffusion times.

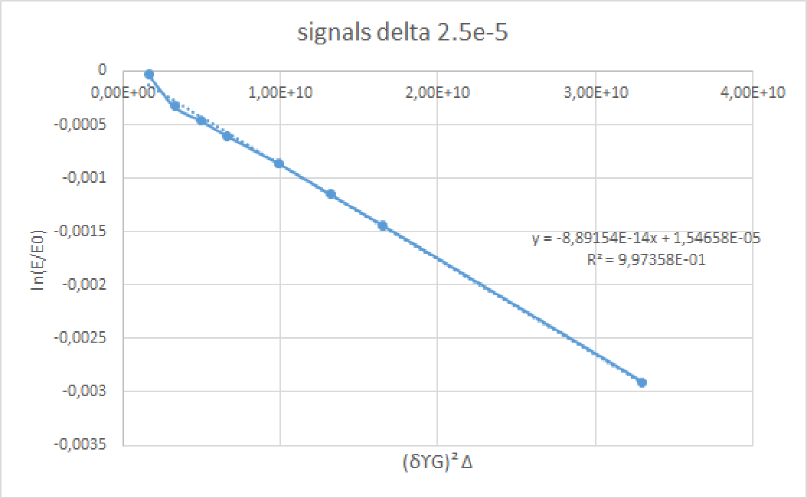

Figure 4.14: Signal attenuation in the calibration solo pore network with delta 2.5e-5, τ=1.06

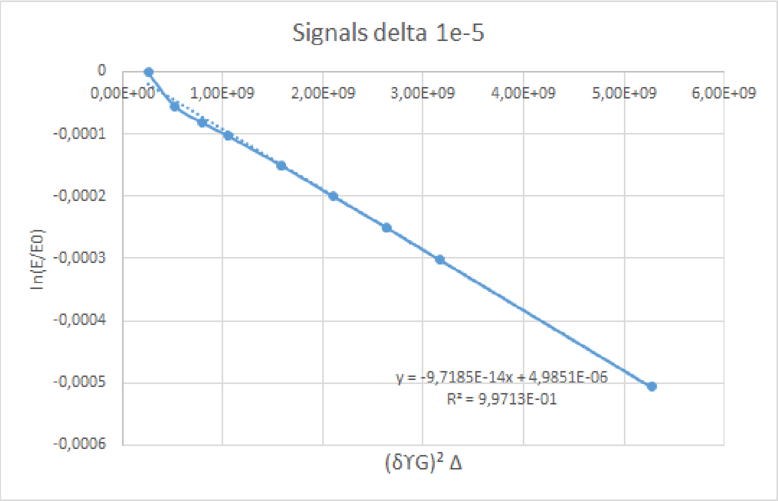

Figure 4.15: Signal attenuation in the calibration solo pore network with delta 1.e-5, τ=0.98

4.4.3 3D network

The 3D networks are more CPU-intensive than the original 2D networks. This is a direct consequence of the increment of nodes and pores in the lattice. Due to this, a variation has been implemented in the dimension of the network.
The network used is composed by a lattice of 10x10x10. As a consequence, in order to avoid the loss of particles, the diffusion coefficient used for the diffusion simulations has been decreased by two orders of magnitude obtaining, D=1,897e^{-15}.
As it has been done in 2D simulations, a calibration with a regular lattice 3D was adopted and the Diffusion coefficient refitted. With the same calibration methodology seen for 2D lattices, it is obtained a δ=6e^{-5}

Chapter 5

Results

The methodology developed in the forth chapter, section ultimate methodology, has proven to be flexible and allows to use various pore networks obtaining the different tortuosities. The pore networks analyzed are regular 2D and their variations. In fact, the proposed results derive from tests on various 2D pore size distributions and networks with various pore existence probabilities. In addition to these tests, different 3D networks were analysed presenting a known pore size distribution and various pore lengths.

5.1 2D Pore networks

Pore size distribution, PSD, and Pore Existence Probability, PEP, allow to obtain a more realistic pore network with a variety of pore sizes in a normalized distribution function with wanted standard deviations and blind pores to reproduce, at the best possible, the porosity in $\gamma-$alumina with respect to the idealized lattice with equal pore sizes.

Table 5.1: Universal parameters used in 2D simulations

Parameter	**Value**
L_{pores} (nm)	60
G$(\frac{T}{m})$	86
δ(s)	1x10^{-5}
γ $\left(\frac{rad}{sT}\right)$	2,67x10^{8}
D $\left(\frac{m^2}{s}\right)$	1,897x10^{-13}

5.1.1 PSD Only

A standard network with PSD was presented in Figure 3.9, the Figure 5.1 represents the signal attenuation with regards to $(\delta\gamma G)^2\Delta$ in a PSD network.

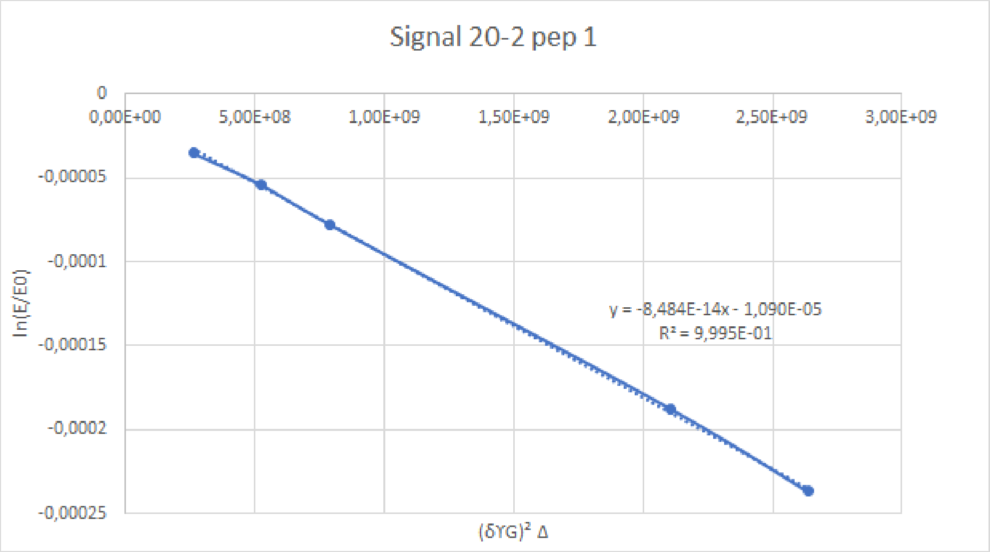

Figure 5.1: Signal attenuation in a pore network PEP 1, Diameter 20 nm, deviation 2 nm

This typology of network presents a tortuosity of 1,12. This value is comprehensibly near the ideal value of 1 obtained with the same δ in a regular and mono-diameter pore network.

5.1.2 PEP and PSD

Different average diameters and standard deviations modify the signals obtained and therefore their tortuosities. Various pore network with a known PEP of 0.8 were investigated and the results analysed. An example network of this typology is visible in Figure 3.11 .

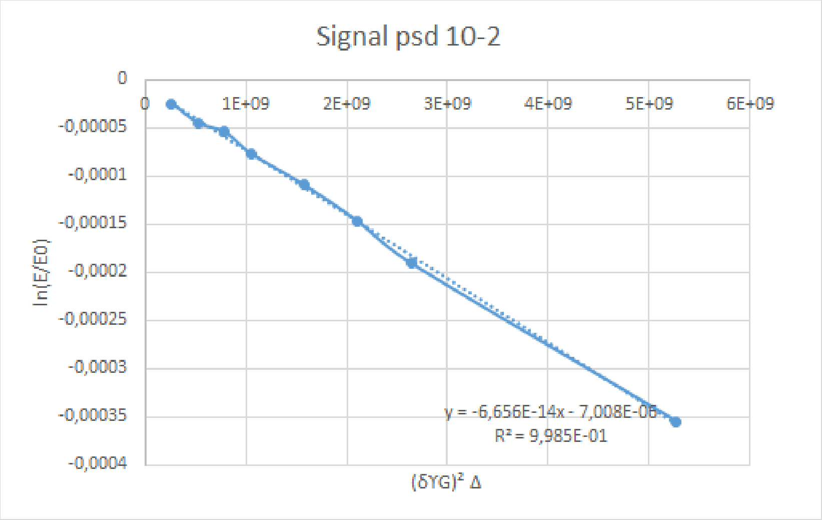

Figure 5.2: Signal attenuation in a pore network PEP 0,8, D 10 nm, deviation 2 nm

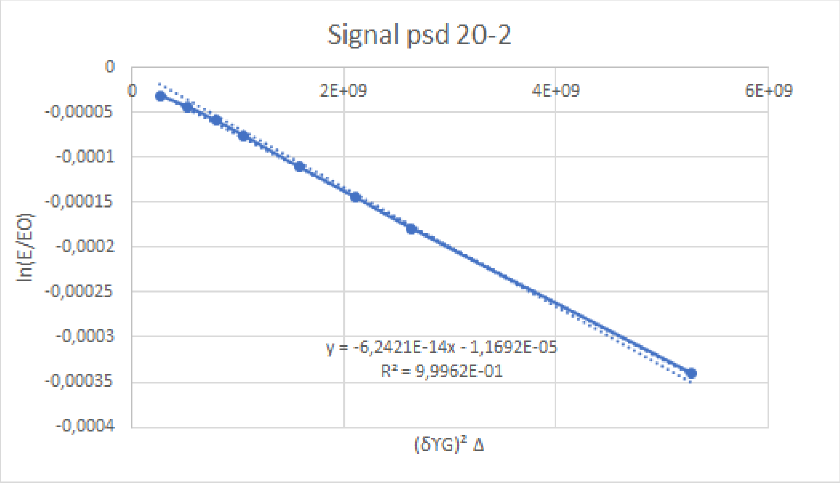

Figure 5.3: Signal attenuation in a pore network PEP 0,8, D 20 nm, deviation 2 nm

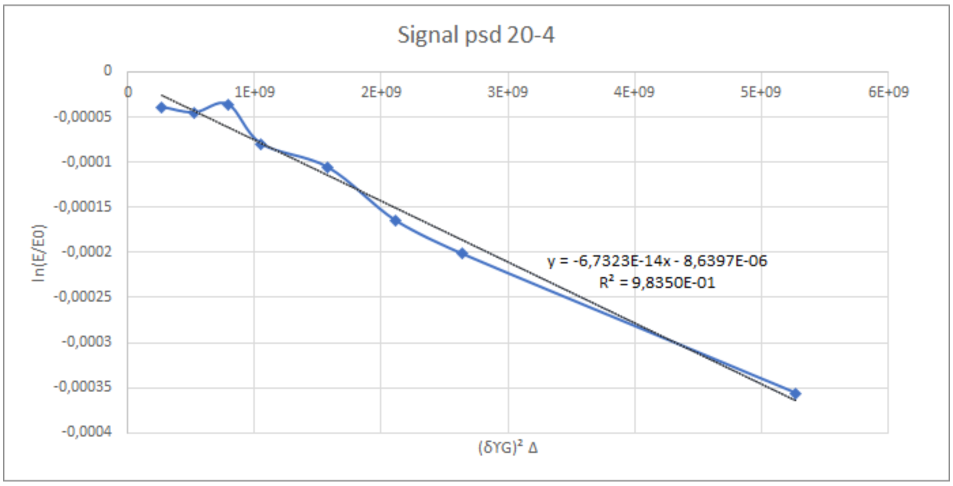

Figure 5.4: Signal attenuation in a pore network PEP 0,8, D 20 nm, deviation 4 nm

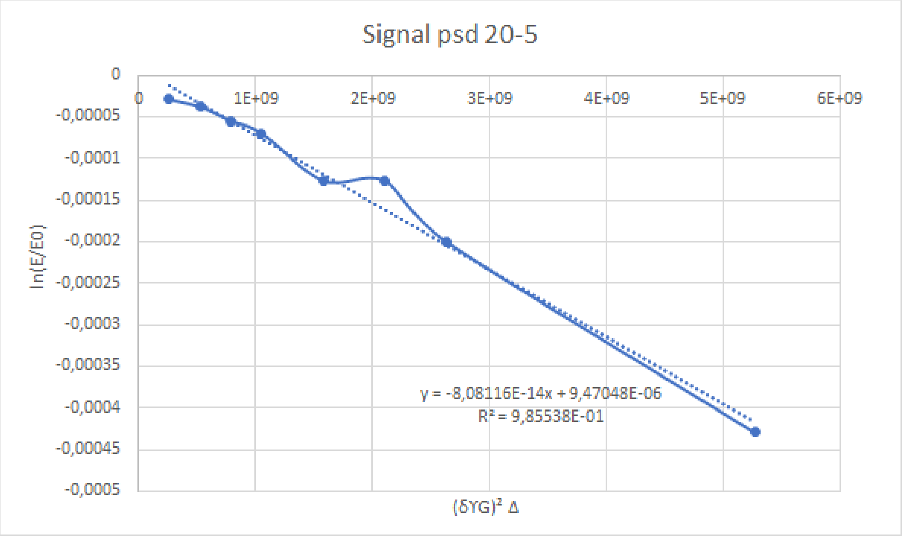

Figure 5.5: Signal attenuation in a pore network PEP 0,8, D 20 nm, deviation 5 nm

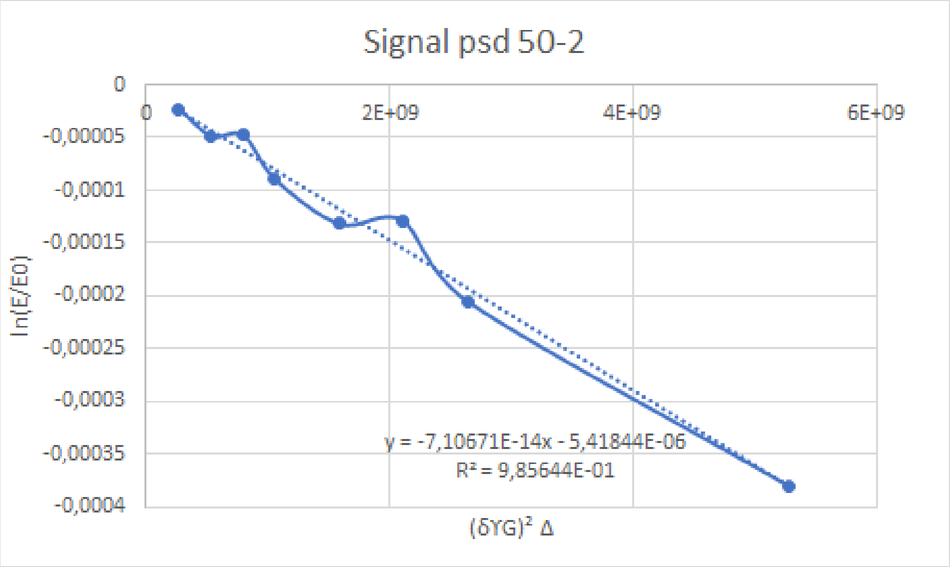

Figure 5.6: Signal attenuation in a pore network PEP 0,8, D 50 nm, deviation 2 nm

Table 5.2: Tortuosities obtained in simulation of pore networks with PSD and PEP 0.8

Average Diameter (nm)	**Deviation (nm)**	**Tortuosity**
10	2	1,42
20	2	1,51
20	4	1,41
20	5	1,17
50	2	1,33

The results visible in Figures (5.2, 5.3, 5.4, 5.5, 5.6) and the numerical values obtained in Tab: 5.2 have to be interpreted.

Analysing the tortuosities, it is visible that a trend between pore diameters cannot be deduced but a tendency in the case of different deviation with the same average diameter is present and probably depends on the fact that in PEP<1 the possibility to have bigger diameters may help the diffusion.

5.1.3 PEP Variation

An additional investigation regarded the impact of different Pore Existence Probabilities in a network with a constant PSD and mean Diameter. The case study regarded pore networks with a mean diameter of 10 nm, this case was researched more in depth.

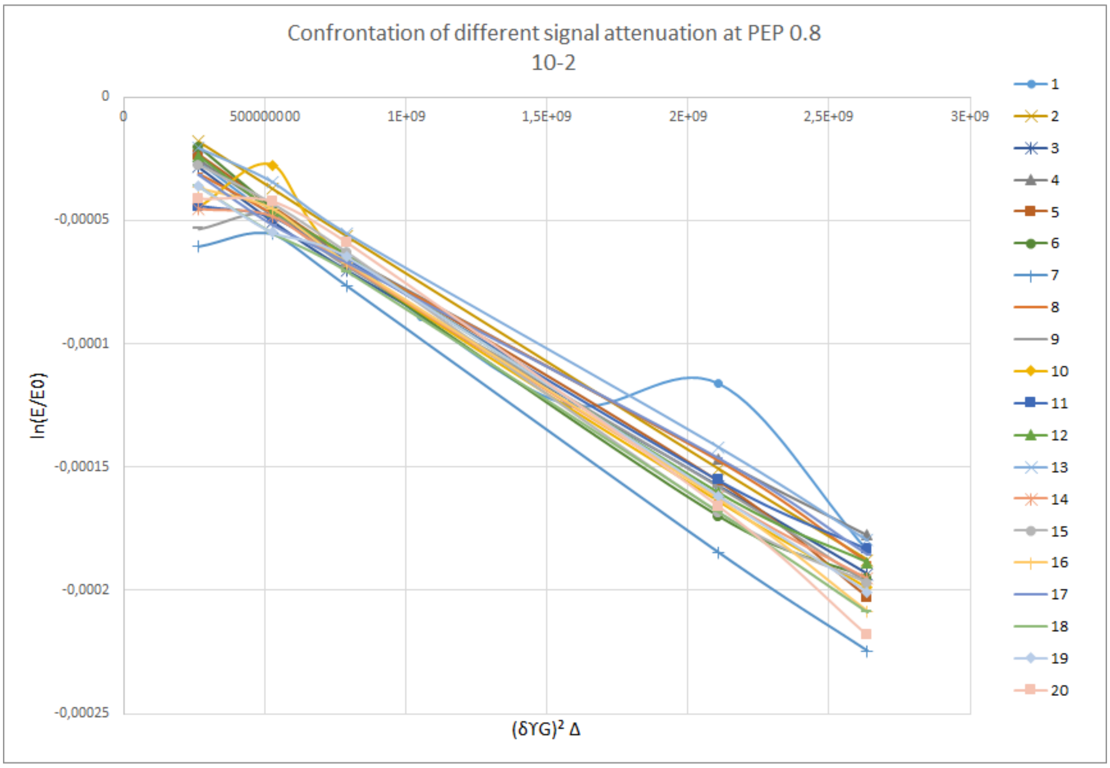

Figure 5.7: Confrontation of signal attenuation in various pore network PEP 0,8, D 10 nm, deviation 2 nm

In the table 5.3 and the similar tables below, it is possible to visualize all the values found in the simulations with the different pore networks, the tortuosity obtained and the standard deviations of the tortuosities.

Table 5.3: Tortuosity and the evolution of the standard deviation in simulations of pore networks used for the simulations with PSD 10-2 and PEP 0.8

Number of simulations	**Tortuosity obtained**	**Standard deviation**
1	1,30	0
2	1,33	0,012
3	1,38	0,035
4	1,50	0,075
5	1,28	0,077
6	1,27	0,077
7	1,27	0,076
8	1,45	0,080
9	1,46	0,084
10	1,31	0,081
11	1,53	0,092
12	1,36	0,088
13	1,41	0,085
14	1,42	0,083
15	1,28	0,084
16	1,29	0,083
17	1,50	0,087
18	1,30	0,086
19	1,36	0,084
20	1,22	0,087

The correlation in Figure: 5.7 is just an example of all the correlations that have been done in the PEP simulations but help to understand how, although some variations are present, the overall trends tend to overlap. Mean tortuosity of the pore networks PEP 0,8: 1,36

Table 5.4: Tortuosity and the evolution of the standard deviation in simulations of pore networks used for the simulations with PSD 10-2 and PEP 0.7

Number of simulations	**Tortuosity obtained**	**Standard deviation**
1	1,46	0
2	1,54	0,043
3	1,57	0,049
4	1,49	0,045
5	1,08	0,178
6	1,41	0,162
7	1,96	0,240
8	1,50	0,224
9	1,74	0,225
10	1,65	0,216
11	1,37	0,211
12	1,79	0,215
13	1,37	0,213
14	1,87	0,222
15	1,63	0,216
16	1,83	0,218
17	1,71	0,214
18	1,46	0,210
19	2,17	0,243
20	1,59	0,237
21	1,27	0,242
22	1,64	0,236
23	1,34	0,237
24	1,42	0,234
25	1,44	0,231
26	1,79	0,231
27	1,75	0,229
28	1,67	0,225
29	2,02	0,235
30	1,69	0,231
31	1,54	0,228
32	2,00	0,234
33	1,58	0,231
34	1,53	0,228
35	1,50	0,226
36	1,34	0,227
37	1,70	0,224
38	1,37	0,225
39	1,69	0,222
40	1,35	0,223

Mean tortuosity of the pore networks PEP 0,7: 1,59

In this case (tab: 5.4) the standard deviation is higher than in the case of PEP 0,8 because the variability of the pore network are more present. In this case the standard deviation is stabilized at 22% which is higher than the 8% of PEP 0.8. This value is measurement of the highest variance of the stochastic pore network.

Table 5.5: Tortuosity and the evolution of the standard deviation in simulations of pore networks used for the simulations with PSD 10-2 and PEP 0.9

Number of simulations	**Tortuosity obtained**	**Standard deviation**
1	1,30	0
2	1,15	0,077
3	1,13	0,076
4	1,21	0,066
5	1,19	0,060
6	1,14	0,058
7	1,16	0,055
8	1,25	0,056
9	1,11	0,058
10	1,34	0,072
11	1,18	0,069
12	1,19	0,066
13	1,22	0,064
14	1,47	0,094
15	1,38	0,099
16	1,23	0,096
17	1,22	0,093
18	1,09	0,096
19	1,21	0,093
20	1,20	0,091

Mean tortuosity of the pore network PEP 0,9: 1,22. Even in this case the standard deviation is below 10%, which is a treshold value that is expected in PEP networks.

By analysing the various tortuosities obtained in the various simulations it is possible to obtain a trend in Figure: 5.8. As the pore existence probability increases, the variability of the network decreases and therefore the tortuosity.

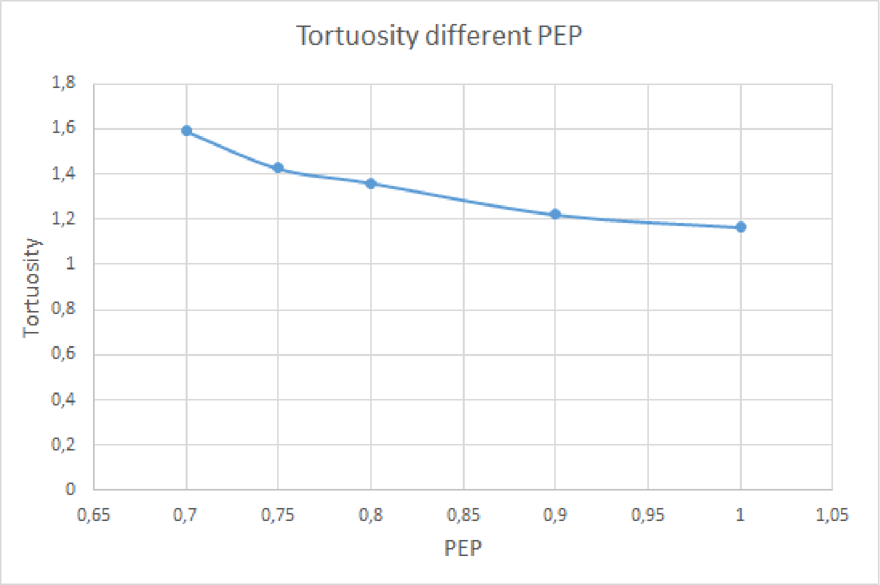

Figure 5.8: Tortuosity obtained with different PEP

5.2 Validation pore network 3D

The strategy adopted in the 2D simulations can be replicated and adapted in 3D pore networks. These networks are conceived to be more similar to real porosity of $\gamma-$alumina and therefore their representation has a higher value than the 2D simulations.They represent in fact the digital twin of an industrial alumina.

The pore network referenced is similar to the one in Figure 3.14. The digital twin developed is visible in Figure 5.9

Figure 5.9: Digital twin γ-alumina. Obtained from[18]

The digital twin was created using statistical parameters already developed[49] in Figure 5.10.

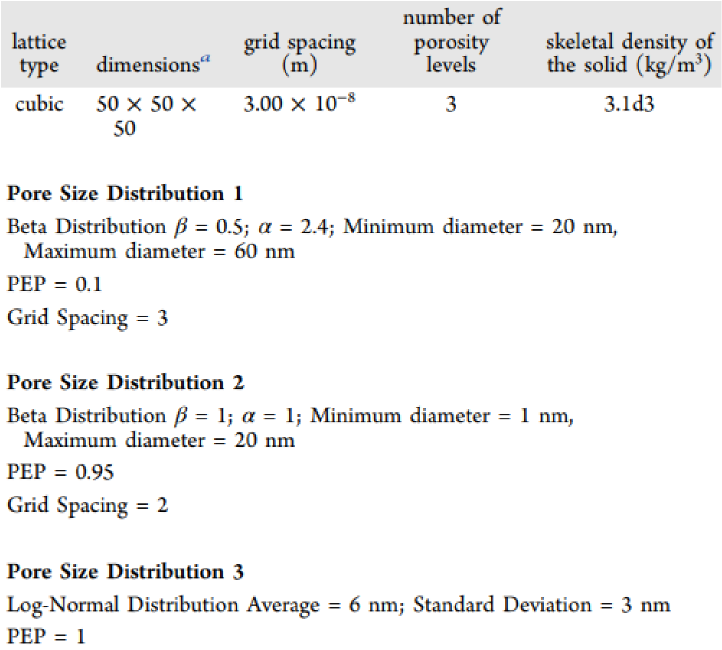

lattice type	dimensions[a]	grid spacing (m)	number of porosity levels	skeletal density of the solid (kg/m^3)
cubic	50 × 50 × 50	3.00×10^{-8}	3	3.1d3

Pore Size Distribution 1

Beta Distribution $\beta = 0.5$; $\alpha = 2.4$; Minimum diameter = 20 nm, Maximum diameter = 60 nm

PEP = 0.1

Grid Spacing = 3

Pore Size Distribution 2

Beta Distribution $\beta = 1$; $\alpha = 1$; Minimum diameter = 1 nm, Maximum diameter = 20 nm

PEP = 0.95

Grid Spacing = 2

Pore Size Distribution 3

Log-Normal Distribution Average = 6 nm; Standard Deviation = 3 nm

PEP = 1

Figure 5.10: Parameters used in the construction of the digital twin with a dimension 10x10x10. Modified from[49]

Table 5.6: Universal parameters used in 3D simulations

Parameter	Value
G$(\frac{T}{m})$	86
δ(s)	6x10^{-5}
$\gamma \left(\frac{rad}{sT}\right)$	2,67x10^{8}
D $\left(\frac{m^2}{s}\right)$	1,897x10^{-15}

The pore networks used have the same number of pores but at different sizes. One network has a pore length of 30 nm and the second 60 nm. In the first network the signal attenuation obtained is Figure:5.11

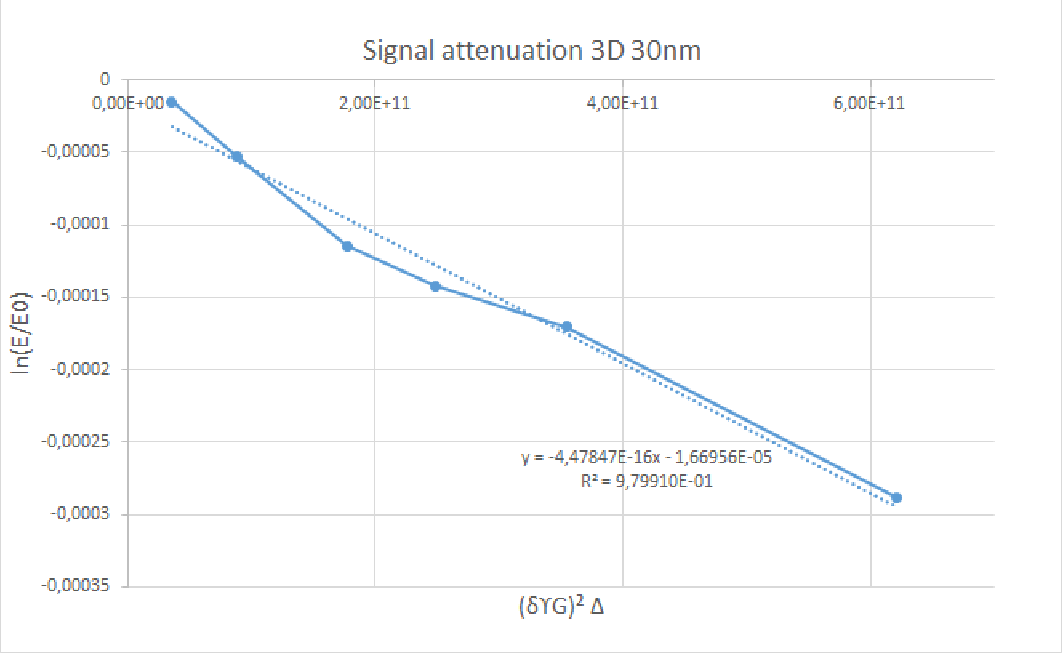

Figure 5.11: Signal attenuation 3D network 30 nm, digital twin

The tortuosity obtained in a 3D network with 30 nm pores is 1,42.
In the second network with a higher pore length the tortuosity obtained is 1,29.
The times used (Δ) between the two 3D networks are different because of the different possibility to trace various tracer pores due to the diversity in lengths.

Table 5.7: 3D simulations Tortuosities

Pore length	**Tortuosity**
30 nm	1,42
60 nm	1,29

The digital twin is represented by the pore network with pore length of 30 nm.

5.3 Comparison

The topology of γ-alumina and its tortuosity is a classical topic in chemical engineering publications. The results found in literature has been therefore correlated to the findings of this thesis. The highest tortuosity acquired is 1,59 in the case of a pore network with a pore existence probability of 0,7. On the other hand the lowest value in a 2D network is 1,12 in a simple 20 nm Diameter PSD network. Furthermore, the results obtained in the 3D networks fall in this range.
In other simulations with a numerical methodology called the semi-infinite pore network that represents an ideal infinite plate in a percolation analysis,[18] the tortuosity increases if the PEP decreases, like it has been observed in the previous section of this thesis. Ledezma found that at a PEP of 0,7 corresponds a τ=1,4 which is slightly lower than the value found in this work. On the other hand at a PEP of 1, it was found a tortuosity of 1,18 which is similar to the findings of this work.

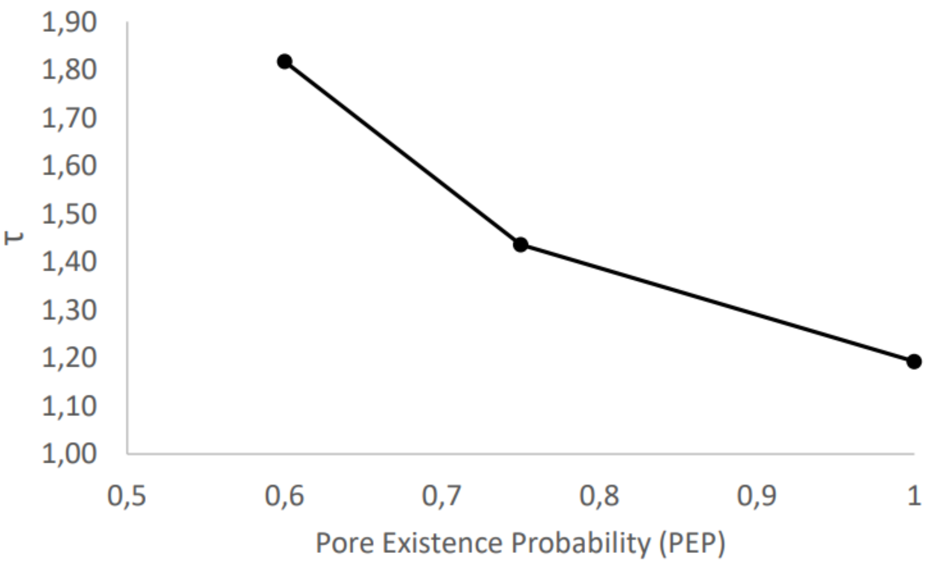

Figure 5.12: Tortuosity PEP network. Obtained from[18]

On the other hand, Ledezma found a net correlation between the increment of diameter and the decrement of tortuosity which was not evident in this work, although the values at 10 and 20 nm are similar to his findings.
The last comparison show a contrast to his work where he finds a slight increase in the tortuosity as the standard deviation in PSD increases while in this work the tortuosity decreases.
The tortuosities found in both this work and Ledezma[18] show a difference towards

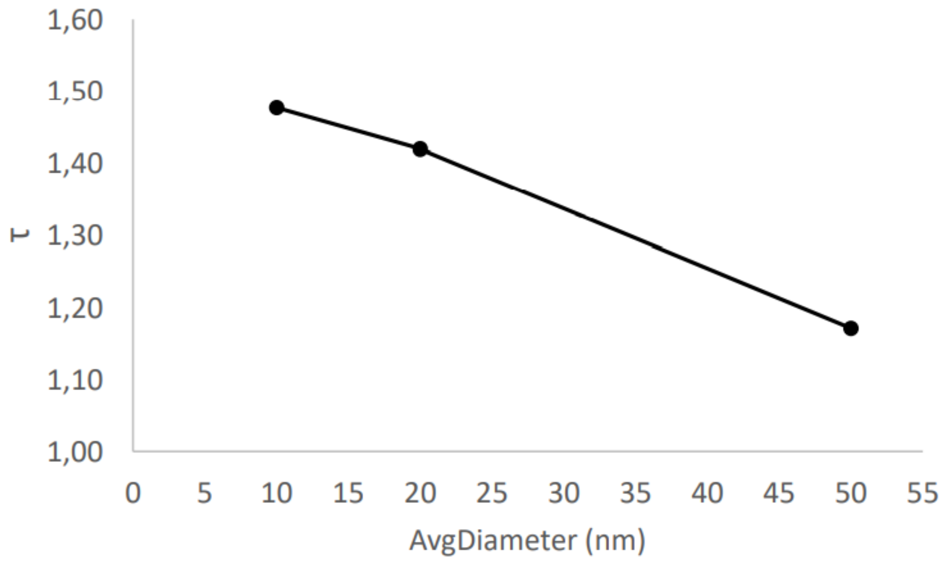

Figure 5.13: Tortuosity networks with different diameters . Obtained from[18]

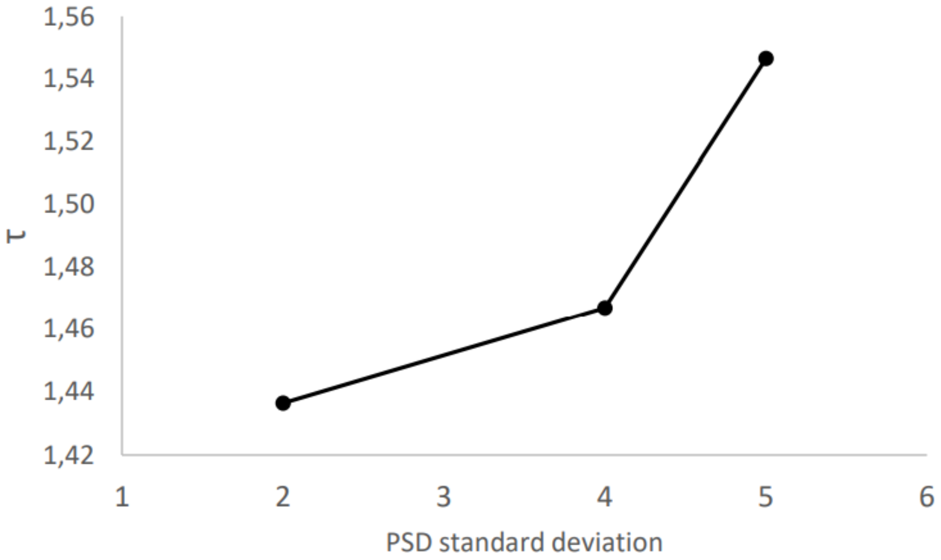

Figure 5.14: Tortuosity networks with different standard deviation. Obtained from[18]

the empirical work of Glowska[36] shown in Figure 5.15. In her work the tortuosities obtained are higher, probably this is due to the effects of pore blocking that in our case have been mitigated by the simulation that does not fully take it into account.

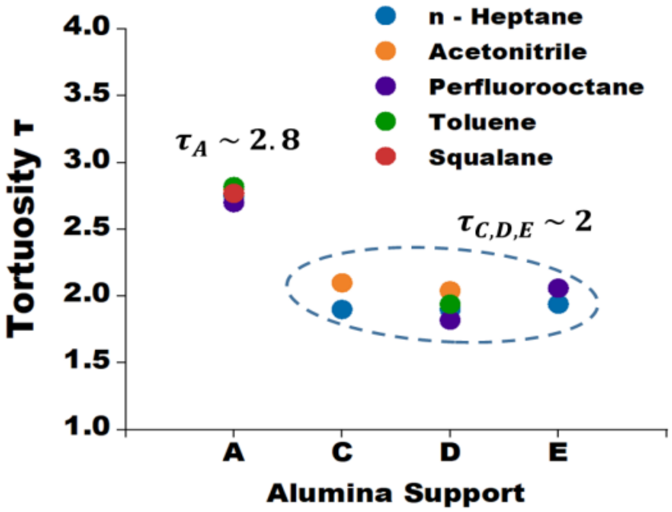

Figure 5.15: Tortuosity measurements in γ-alumina PFG-NMR. Obtained from[36]

Another publication that can be used to analyse the results is the work of Kolitcheff.[16] He used an experimental PFG-NMR technique and discovered that the use of liquids with affinity with the surface like toluene implied a tortuosity factor of 3,5. On the other hand, the use of non-affine liquids allowed to obtain tortuosity of 1,8 which is in accordance with the value of both this and Ledezma's work.
The last publication used is an article that studies the tortuosity of mesoporous alumina catalyst.[50] In this article, the statement is that tortuosity values for a porous network are expected to be below 1,9. This value agrees with the numerical results obtained.
The tortuosity of the 3D network has been directly correlated to the results of Ledezma with nitrogen porosimetry of the same digital twin. In this characterization the tortuosity is 1,42, while in his work is 1,8. It is therefore acceptable to obtain a variation of the two values of 21%.

Chapter 6

Conclusion and Future Works

A fast PFG-NMR simulation module able to characterize the tortuosity of a $\gamma-$alumina digital sample was developed. The novelty of this methodology relies on the implementation of a Fickian diffusion module to simulate the PFG-NMR techique at the mesoscopic scale.

The influence of the pore distribution and the porosity of the sample on the tortuosity values obtained from PFG-NMR simulation show the same found on the literature and experimental works.

The simulation was validated by characterizing a digital twin of an industrial $\gamma-$alumina sample. The tortuosity value obtained differs by 21% of the experimental value. It means that although a variation is present, a prediction of the value of the tortuosity in a γ-alumina sample is possible by starting with a digital twin.

6.1 Future works and perspectives

Although the results have exceeded the expectations creating a new valid tool to analyse the topology of a porous network, improvements in a short and medium scale could certainly refine the model.

- Roughness has not been incorporated in the model. The corrugated pore statistical model could be used to understand the influence.
- The size of the networks are smaller than the real pore network and the topological analysis may be affected.
- The run-time is a problem and the system resources of a single computer are limited.
- The code is not parallelized and it decreases the chances of use in a HPC system.
- A better calibration tool has to be created to properly analyse the topology of various typologies of pore networks
- The integration of reactions as a catalytic system would create infinite possibility of usage.

List of Symbols

γ-Al_2O_3, γ-Alumina
PFG-NMR, Pulsed field gradient-Nuclear Magnetic Resonance
NMR, Nuclear Magnetic Resonance
γ, gyromagnetic ratio in NMR
ω, Larmor frequency
FID, Free Induction Decay
δ , the gradient duration (s)
Δ, diffusion time (s)
g, gradient intensity (T)
D, molecular diffusion coefficient ($\frac{m^2}{s}$)
MSD, Mean squared Displacement
D_{eff}, Effective (also called apparent) Diffusion coefficient
GPD, Gaussian Phase Distribution
SGP, Short Gradient Pulse
PEP, Pore Existence Probability
PSD, Pore Size Distribution
$C_{a,i}$, Concentration of specie a in pore i
$X_{a,i}$, Molar fraction of specie a in pore i
L_{az},dimension of the active zone
L_n, total length of the pore network
L_D, distance of the active zone to the borders of the pore network
τ, tortuosity

Bibliography

[1] L. Ma, D. B. Ingham, M. Pourkashanian, E. Carcadea, «Review of the Computational Fluid Dynamics Modeling of Fuel Cells», *Journal of Fuel Cell Science and Technology* **2005**, *2*, 246–257.

[2] P. R. Nivea, A. Asif, A. Zahid, M. S. A. D., L. V. D'Souza, «Computational Fluid Dynamics in Turbomachinery: A Review of State of the Art», *Archives of Computational Methods in Engineering* **2017**, 467–479.

[3] J. Bravo-Suárez, R. Chaudhari, B. Subramaniam, «Design of Heterogeneous Catalysts for Fuels and Chemicals Processing: An Overview», *ACS Symposium Series* **2013**, *1132*, 3–68.

[4] M. O'Sullivan, S. Zarrouk in Proceedings of 23rd New Zealand Geothermal Workshop, Auckland, New Zealand, **2001**.

[5] L. Sharifi, S. Ghanbarnezhad, S. Ghofrani, S. H. Mirhosseini, «High Porous Alumina Bodies: Production and Properties via Gel-Casting Technique», *International Journal of Advanced Science and Technology* **2014**, *65*, 59–70.

[6] K. Wefers, C. Misra, Oxides and Hydroxides of Aluminum, Alcoa Technical Paper No. 19, Pennsylvania, USA, **1987**.

[7] P. R. Bridenbaugh, K. R. V. Horn, J. T. Staley, Aluminum processing, https://www.britannica.com/technology/aluminum-processing, **2018**.

[8] G. Paglia, Determination of the Structure of *gamma*-Alumina using Empirical and First Principles Calculations combined with Supporting Experiments, PhD thesis, Curtin University of Technology, **2004**.

[9] F. Ulrich, *Notice regarding the crystal structure of the corundum-hematite group*, 8th ed., Norsk Geologrisk Tidsskrift, **1925**, pp. 115–122.

[10] N. Rosenberger, B. Steuler, C. Compson, Applications for Alumina in the Automotive Market, https://www.ceramic-applications.com/applications-for-alumina-in-the-automotive-market/, "(accessed: 16.01.2022)".

[11] S. E. Tung, E. Mcininch, «High-purity alumina I. The nature of its surface acid sites and its activity in some hydrocarbon conversion reactions», *Journal of Catalysis* **1964**, *3, Issue 3,* 229–238.

[12] A. Manasilp, E. Gulari, «Selective CO oxidation over Pt/alumina catalysts for fuel cell applications,» *Applied Catalysis B: Environmental* **2002**, *37, Issue 1*, 17–25.

[13] M. Bajgiran, M. Rad, A. McDonald, «Microstructure, Phase and Dielectric Strength of Thermally Sprayed Alumina Layers in Coating–Based Heating Systems», *International Journal of Applied Ceramic Technology* **2021**, *18*, DOI `10.1111/ijac.13731`.

[14] M. K. Drost, C. Call, J. Cuta, R. Wegeng, «MICROCHANNEL COMBUSTOR EVAPORATOR THERMAL PROCESSES», *Microscale Thermophysical Engineering* **1997**, 321–332.

[15] E. J. W. Verwey, «The Crystal Structure of γ-Fe2O3 and γ-Al2O3», *Zeitschrift für Kristallographie - Crystalline Materials* **1935**, *91*, 65 –69.

[16] S. Kolitcheff, Approche multitechnique des phénomènes de diffusion en hydrotraitement de distillats, PhD thesis, Université de Lyon, **2017**.

[17] J. Pikunic, C. M. Lastoskie, K. E. Gubbins, *Molecular Modeling of Adsorption from the Gas Phase*, John Wiley & Sons, Ltd, **2002**, Chapter 2.5.1, pp. 182–236.

[18] G. A. L. Ledezma, Suitable Representations of Gamma Alumina Porous Structures by Computational Modeling, PhD thesis, Université Claude Bernard Lyon 1, École Doctorale 206, **2021**.

[19] J. Backus in *History of Programming Languages*, Association for Computing Machinery, New York, NY, USA, **1978**, 25–74.

[20] D. Seshadri, *Communication with Computers- An introduction*, **2017**.

[21] M. Dominique, «An introduction to biological NMR spectroscopy», *Molecular & cellular proteomics : MCPs* **2013**, *12*, DOI `10.1074/mcp.O113.030239`.

[22] R. J. S. Brown, P. Fantazzini, J. Kärger, R. Kimmich in *Diffusion NMR of Confined Systems: Fluid Transport in Porous Solids and Heterogeneous Materials*, The Royal Society of Chemistry, **2017**, pp. 1–15.

[23] R. J. Davis, «New perspectives on basic zeolites as catalysts and catalyst supports», *Journal of Catalysis* **2003**, *216*, 40th Anniversary Commemorative Issue, 396–405.

[24] R. Skloot, Henrietta's Dance, ://pages.jh.edu/jhumag/0400web/01.html, "(accessed: 06.02.2022)".

[25] M. H. Levitt, *Spin Dynamics Basics of Nuclear Magnetic Resonance*, John Wiley & Sons, Ltd, **2008**.

[26] W. Pauli, «The Connection Between Spin and Statistics», *Phys. Rev.* **1940**, *58*, 716–722.

[27] Wikipedia, Gyromagnetic ratio— Wikipedia, The Free Encyclopedia, [Online; accessed 08-February-2022], **2022**.

[28] P. A. Rinck, *Magnetic resonance in medicine: A Critical Introduction*, BoD, **2016**, Chapter Relaxation Times and Basic Pulse Sequences in MR Imaging.

[29] J. P. Hornak, *The Basics of NMR*, **1997-2019**.

[30] H. C. Torrey, «Bloch Equations with Diffusion Terms», *Phys. Rev.* **1956**, *104*, 563–565.

[31] W. S. Price, «Pulsed-field gradient nuclear magnetic resonance as a tool for studying translational diffusion: Part 1. Basic theory», *Concepts in Magnetic Resonance* **1997**, *9*, 299–336.

[32] J. Kärger, M. Avramovska, D. Freude, J. Haase, S. Hwang, R. Valiullin, «Pulsed field gradient NMR diffusion measurement in nanoporous materials», *Adsorption* **2021**, *27*, 453–484.

[33] W. S. Price, «Pulsed-field gradient nuclear magnetic resonance as a tool for studying translational diffusion: Part 2. Experimental Aspects», *Concepts in Magnetic Resonance* **1998**, *10*, 197–237.

[34] E. O. Stejskal, J. E. Tanner, «Spin Diffusion Measurements: Spin Echoes in the Presence of a Time-Dependent Field Gradient.», *The Journal of Chemical Physics* **1965**, *42*, 288–292.

[35] P. Galvosas, F. Stallmach, G. Seiffert, J. Kärger, U. Kaess, G. Majer, «Generation and Application of Ultra-High-Intensity Magnetic Field Gradient Pulses for NMR Spectroscopy», *Journal of Magnetic Resonance* **2001**, *151*, 260–268.

[36] A. Glowska, Multi-technique analysis of porous networks in gamma-alumina supports, PhD thesis, IFPEN and University College London, Department of Chemical Engineering, London, **2021**.

[37] B. Balinov, B. Jonsson, P. Linse, O. Soderman, «The NMR Self-Diffusion Method Applied to Restricted Diffusion. Simulation of Echo Attenuation from Molecules in Spheres and between Planes», *Journal of Magnetic Resonance* **1993**, *104*, 17–25.

[38] A. Wheeler, *Reaction Rates and Selectivity in Catalyst Pores*, Academic Press, **1951**, pp. 249–327.

[39] I. Fatt, «The Network Model of Porous Media», *Transactions of the AIME* **1956**, *207*, 144–181.

[40] M. J. Blunt, «Flow in porous media — pore-network models and multiphase flow», *Current Opinion in Colloid & Interface Science* **2001**, *6*, 197–207.

[41] X. Huang, K. Bandilla, M. Celia, «Multi-Physics Pore-Network Modeling of Two-Phase Shale Matrix Flows», *Transport in Porous Media* **2016**, *111*, 123–141.

[42] J. Villadsen, W. Stewart, «Solution of boundary-value problems by orthogonal collocation», *Chemical Engineering Science* **1967**, *22*, 1483–1501.

[43] P. E. V. Keken, D. A. Yuen, L. R. Petzold, «DASPK: A new high order and adaptive time-integration technique with applications to mantle convection with strongly temperature-and pressure-dependent rheology», *Geophysical & Astrophysical Fluid Dynamics* **1995**, *80*, 57–74.

[44] D. G. Griera, Dynamical Measurements, **1996**, `https://physics.nyu.edu/grierlab/methods/node11.html`.

[45] Risorse di calcolo fornite hpc@polito, progetto di Academic Computing del Dipartimento di Automatica e Informatica presso il Politecnico di Torino (http://www.hpc.polito.it).

[46] C. H. Neuman, «Spin echo of spins diffusing in a bounded medium», *The Journal of Chemical Physics* **1974**, *60*, 4508–4511.

[47] W. Kittler, S. Obruchkov, M. Hunter, P. Galvosas in *Diffusion NMR of Confined Systems: Fluid Transport in Porous Solids and Heterogeneous Materials*, The Royal Society of Chemistry, **2017**, pp. 194–225.

[48] H. Wang, F. Willot, M. Moreaud, M. Rivallan, L. Sorbier, D. Jeulin, «Numerical Simulation of Hindered Diffusion in γ -Alumina Catalyst Supports», *Oil & Gas Science and Technology* **2017**, *72*, 8.

[49] G. A. Ledezma Lopez, J. J. Verstraete, L. Sorbier, A. Glowska, D. Leinekugel-Le-Cocq, E. Jolimaitre, C. Jallut, «Generation of -Alumina Digital Twins Using a Nitrogen Porosimetry Simulation», *Industrial & Engineering Chemistry Research* **2021**, *60*, 16728–16738.

[50] S. Kolitcheff, E. Jolimaitre, A. Hugon, J. Verstraete, P.-L. Carrette, M. Tayakout-Fayolle, «Tortuosity of mesoporous alumina catalyst supports: Influence of the pore network organization», *Microporous and Mesoporous Materials* **2017**, *248*, 91–98.

Acknowledgement

I would like to thank prof. Stefania Specchia, thanks to her will to uplift each student, she gave me the opportunity to work in collaboration with an international facility, IFP-EN of Lyon. I have known her since the bachelor years because of her role in the mobility team, she was there when I could not go to another mobility because of the pandemic but she always allowed to bring the best of each opportunity that my colleagues and I have had.

Secondly, I want to thank Gabriel Ledezma. In less than a year I have probably spent more time with you than with my family. I will always fondly remember the online meetings, your patience and professionalism. Each of the step that I have achieved was supervised and pushed towards the, initially impossible, goal of a working model. I can not really express my gratitude for your help. Furthermore, the possibility that I have had to visit with you the IFP plant helped me understand my future path.

I thank Carmen Moncada, at the start of this path we both were experiencing difficulties, but they were just the foundations of a great collaboration.

Voglio ringraziare i miei genitori, non sono sempre stato il figlio più simpatico che ci sia e praticamente non sapete mai cosa sto facendo. Questa è la mia tesi, ci ho lavorato per quasi un anno e questi sono i risultati. Mi avete aiutato con il vostro supporto incondizionato pur inconsapevoli di quello che stavo facendo.
Per quanto riguarda mia sorella Chiara, ti voglio ringraziare più di tutti. Tu sapevi e sei stata la complice ideale per non dir loro niente. Da quando ti sei trasferita ci vediamo di meno ma faccio in modo di sfruttarti il più possibile nei miei lunghi viaggi al nord. Grazie mille per il tuo sostegno in questi duri anni di università.

Un ringraziamento speciale è necessario per Riccardo, da quando ci siamo conosciuti al liceo hai fatto un percorso eccezionale, spingendo me e tutti quelli al nostro fianco a puntare sempre più in alto.

Un ringraziamento va a tutti quelli che conosco e che mi sono amici, chi conosco dalle medie come Carlo che ho visto crescere da bambino a uomo, a chi ho conosciuto al liceo. Quando le amicizie sono sincere non è un caso che durino per molti anni anche se, a parte gli ultimi anni, non riusciamo a vederci spesso.

L'ultimo ringraziamento è per chi ho conosciuto all'università e che ha condiviso con me gli anni della triennale e della magistrale. Ringrazio la possibilità che ho avuto con alcuni di vivere insieme e con tutti la voglia di andare in vacanza. Non è un caso se questi anni siano passati indenni, senza di voi non ce l'avrei fatta. Ringrazio sia chi c'è dal giorno 0 sia chi è arrivato dopo, un pezzo di quello che siete voi adesso è presente anche in me.